Office of Graduate Programs
School of Engineering and Applied Science
Thornton Hall A108
20200609

Thesis/Dissertation Cover and Approval Pages

* Complete the following Form Variables and then click UPDATE

Form Variables

Document Title	Ice Adhesion on Various Surfaces and Flow Conditions
Student Name	Edem Yannick Tetteh
Document Type	Dissertation
Degree	Doctor of Philosophy
Semester/Year Degree Awarded	August 2020
Advisor 1	Dr. Eric Loth
Advisor 2	
Committee Member 1	Dr. David Green
Committee Member 2	Dr. Daniel Quinn
Committee Member 3	Dr. Mool Gupta
Committee Member 4	Dr. Chao (Chris) Qin
Committee Member 5	
Committee Member 6	

UPDATE

Ice Adhesion on Various Surfaces and Flow Conditions

A

Dissertation

Presented to

the faculty of the School of Engineering and Applied Science

University of Virginia

in partial fulfillment

of the requirements for the degree

of Doctor of Philosophy

by

Edem Yannick Tetteh

August 2020

APPROVAL SHEET

This

dissertation

is submitted in partial fulfillment of the requirements
for the degree of

Doctor of Philosophy

Author: Edem Yannick Tetteh

This dissertation has been read and approved by the examining committee:

Advisor: Dr. Eric Loth

Advisor:

Committee Member: Dr. David Green, (Chair)

Committee Member: Dr. Daniel Quinn

Committee Member: Dr. Mool Gupta

Committee Member: Dr. Chao (Chris) Qin

Committee Member:

Committee Member:

Accepted for the School of Engineering and Applied Science:

Craig H. Benson, School of Engineering and Applied Science

Abstract

Atmospheric icing presents a threat to many human-made devices with examples including icing of electrical power networks, wind turbines, communication towers, and aircraft. Predominantly in the case of aircraft engine, ice accretion and ingestion of shed ice (after accretion) can be detrimental to the engine performance. As such, many studies have been conducted, seeking new and innovative solutions to the icing problems. Among these studies, ice adhesion is particularly investigated, as surfaces with low ice adhesion property are very much sought. Additionally, ice shedding very much depends on adhesion. However, the majority of the work done has mainly focused on static ice, contrarily to high-speed impact ice as it would occur in the situation of engine components in flight conditions. A detailed review of engine icing including icing due to both supercooled droplets and ice crystals is first conducted, as this does not yet exist in the available literature. This review motivates specific experimental investigations for the rest of the PhD dissertation. In particular, ice adhesion would be measured in both tensile and shear mode for both static and impact ice in the same facility, making this work unique among many previously published reports.

The present work will investigate ice adhesion for a variety of flow conditions and surfaces. The tested surfaces will range from metal alloys to icephobic coatings. The facility to be designed, developed and employed would be a novel compact icing research tunnel (CIRT), allowing installation of detailed surface and diagnostic devices to measure ice adhesion stress and thermal conditions. Finally, a comparison between this new set of data to existing ice adhesion data available in the literature would be provided, as well as predominant trends in ice adhesion strength model on various surfaces.

For my dad

Acknowledgements

The technical, physical, and emotional journey of completing this dissertation would not have been possible without the guidance and inspiration of various essential people.

First and foremost, I would like to sincerely thank my advisor, Dr. Eric Loth, who not only provided the platform for me to embark on this process, but also provided expert mentorship, intelligence, and support throughout this period of study. Dr. Loth, your attention to details is impeccable and from you I have learned about not only fluid mechanics but also resilience, professionalism, and adaptability.

Special thanks goes to Jim and Jessica at Rolls-Royce for their mentorship and direction throughout this experience. Jim and Jessica, your valuable inputs and continual advice have shaped the way I maneuver through projects. Rolls-Royce, thank you for sponsoring this venture.

I am also indebted to the leadership and support received from my thesis committee. Their instrumental input and time commitment is ultimately what has allowed me to reach this point.

I truly appreciate my fellow colleagues and members of the Fluid Research and Innovation Laboratory (FRIL) for their continued support and encouragement through this endeavor. Their patience, friendship, and understanding made it all bearable.

Further thanks goes to my Charlottesville friends and church family for their unwavering warmth and fellowship throughout the years. I also want to thank Audrey, my girlfriend, for the moral support and making this dissertation journey enjoyable.

Finally, many thanks goes to my relatives and dear family here in the United States and abroad. Specifically, I honor my loving parents, Joseph and Marcelline, and brother Aristo. My determined brother, thank you for always believing in my dreams. My diligent father, I am eternally thankful for you setting the bar high and motivating me to achieve and surpass it. My dedicated and dependable mother, thank you for your steadfast prayers, support, and love through it all.

Lastly, I would be a miss if I did not give all honor and glory to who has done it all, God. I want to thank the Lord for his strength and peace throughout this process.

Table of Contents

List of Figures

List of Tables

Nomenclature

Acronyms

AFC	=	Axial Flow Compressor
AOA	=	Angle Of Attack
CFD	=	Computational Fluid Dynamics
CIRT	=	Compact Icing Research Tunnel
CIT	=	Cranfield Icing Tunnel
EGV	=	Exit Guide Vane
FAA	=	Federal Aviation Administration
HIWC	=	High Ice Water Content
ICI	=	Ice Crystal Icing
IGV	=	Inlet Guide Vane
IPS	=	Icing Protection System
IRT	=	Icing Research Tunnel
IWC	=	Ice Water Content
LE	=	Leading Edge
LP	=	Low Pressure
LWC	=	Liquid Water Content
LWC	=	Liquid Water Content
MMD	=	Mass Median Diameter
MR	=	Melt Ratio
MVD	=	Median Volume Diameter
MVD	=	Mean Volumetric Diameter
NASA	=	National Aeronautics and Space Administration
NASA	=	National Aeronautics and Space Administration
NRC	=	National Research Council

PDF	=	Probability Distribution Function
PSL	=	Propulsion Systems Laboratory
RPM	=	Revolutions Per Minute
SDI	=	Supercooled Droplet Icing
TC	=	Thermocouple
TWC	=	Total Water Content (LWC + IWC)

Variables

c_p	=	Constant Pressure Specific Heat
d	=	Droplet Diameter
D	=	Diameter
D	=	Droplet Path Derivative
e	=	Collection Efficiency
h	=	Enthalpy
H	=	Accreted Ice Height
k	=	Thermal Conductivity
L	=	Length
M	=	Mach number
m	=	Mass
$\dot{m}$	=	Mass Flux
N1	=	Fan Speed for a two-spool engine
N2	=	High Pressure Speed for a two-spool engine
p	=	Pressure
P	=	Pressure
$\dot{Q}$	=	Heat Transfer Rate
R	=	Radius

t	=	Accretion Thickness
T	=	Temperature
V	=	Velocity
α	=	Fraction
β	=	Time
Δ	=	Loss
ρ	=	Density
τ	=	Response Time-scale

Subscripts

b	=	Blade
cl	=	Centerline
f	=	Fluid (Freezer/Ambient Air)
h	=	Hydraulic
m	=	Measured
o	=	Stagnation
p	=	Particle (droplet)
st	=	Sticking
T	=	Thermal
TS	=	Test Section
wb	=	Wet Bulb

Chapter:

1 Introduction

1.1 Background & Motivation

Atmospheric icing could be problematic for several applications. These applications, which include wind turbines, aircraft (engine and wings), and power lines, often experience a performance decrease or safety hazard once ice forms on their surfaces. Generally, ice accretion occurs on these applications after impact of supercooled droplets in freezing environmental conditions (as shown in Fig. 1-1). An example of ice buildup on a wind turbine blade is shown in Fig. 1-2. Such ice accretion on these blades often results in a decrease of power production by up to 50% [1].

Furthermore, ice accretion in the case of aircraft can be a threat to flight safety and airworthiness [2,3]. In particular, ice accretion on wings (shown in Fig. 1-2) can result in increased drag and loss of lift, while ice accretion on various engine components and ingestion has been reported to cause engine problems such as compressor stall/surge, rollback or engine flameout. As such, it is crucial to come up with solutions to mitigate ice accumulation on these applications.

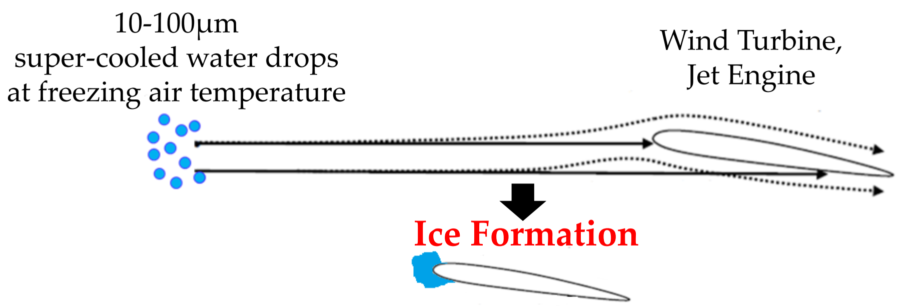

Fig. 1-1 Schematic depicting atmospheric icing on applications (e.g., wind turbine blades, jet engine components).


(a) (b)

Fig. 1-2 Atmospheric icing on (a) a wind turbine blade, and (b) an aircraft's wing.

1.2 Anti/De-icing Methods

Current anti/de-icing strategies include the use of electro-thermal systems to remove or prevent ice from forming on the previously mentioned applications. Another technique is the use of pneumatically controlled rubber boots often installed on aircraft's wings to shed ice formed at the leading edge. However, these techniques are either costly or have a limited performance. The electro-thermal systems are generally energy-driven, which often reduce the overall operating efficiency of the concerned application. On the other hand, the pneumatic de-icing boot is only effective for a certain amount of ice accumulation [4]. Therefore, a few researchers suggested the use of icephobic surfaces as an alternative and optional solution. These surfaces facilitate the removal of ice or retard its formation [5,6]. Additionally, they do not require the use of any sort of energy. As a result, they stand as promising candidates in the search of innovative anti/de-icing techniques.

1.3 Research Objectives and Dissertation Outline

Generally, the key factor behind a good icephobic surface is the adhesion bond between the formed ice and the surface. Therefore, this adhesion factor must be low. However, this factor is usually determined for most icephobic surfaces using static ice (inert water frozen atop a surface); contrarily to impact ice (ice formed from supercooled droplets impacting a surface at high velocity) as it would occur for example in the case of aircraft and aircraft engine components. In addition, both impact and static ice adhesion measurements have never been done in the same facility/environment. Consequently, the research goal of this project is the measurement of ice adhesion for various surfaces at different flow conditions. This involves first identifying the importance of atmospheric icing, measuring ice adhesion in tensile and shear mode on metallic and icephobic surfaces for static and high-speed impact ice, and is systematically done through four objectives presented in five main chapters:

i) Chapter 2: is a survey of engine components' icing to identify when icing occurs, where it occurs, how it occurs, and the impact of its occurrence. As mentioned earlier, engine ice adhesion and shedding assume importance since the ingestion of the shed ice leads to detrimental effects on the engine.

ii) Chapter 3: describes the development and construction of a well-controlled compact icing research tunnel (CIRT) allowing installation of small samples on which adhesion measurement could be taken, and the generation of good quality static and impact ice.

iii) Chapter 4 & 5: characterize an icephobic surface compared to other surfaces in terms of ice adhesion in tensile (Chapter 4) and shear mode (Chapter 5) for both static and impact ice.

iv) Chapter 6: collects existing and published ice adhesion data and describe overarching trends in ice adhesion strength model on various surfaces.

These five main chapters are written as independent articles and convey pertinent information to the reader. To conclude, a summary of all the findings from all these objectives is presented in Chapter 7 along with an overall description of the major contributions of this work to the field of engine icing, ice adhesion strength and icephobic surfaces.

Chapter:

2 Supercooled Droplet Icing and Ice Crystal Icing of Aircraft Engines: When it Occurs, Where it Occurs, How it Occurs, and the Impact of its Occurrence

2.1 Introduction

Ice can form on engine aerodynamic surfaces during flight operation when exposed to low temperatures and in the presence of atmospheric water [7]. Such ice accretion and the ensuing surface release can cause damage to engine parts and flow blockage, which can result in engine rollback or flameout. As such, ice accretion on engine surfaces has been recognized as a fundamental problem and a potential flight safety hazard [2,3,8–10]. Fig. 2-1 below is an example of ice formed from supercooled droplets freezing on impact on the inlet of an engine (W24C-2) during a flight [11]. "Supercooled" indicates that the water is still in liquid form but is surrounded by air below freezing temperature. This type of icing has been studied for many years and engine icing protection system (IPS) have been incorporated to reduce/mitigate these supercooled droplet icing (SDI) threats. However, the current Federal Aviation Administration (FAA) potential icing flight envelopes [12–14] have more recently included ice crystal icing conditions in recognition of this additional threat. Thus, the FAA now defines envelopes for engine icing certification (where an engine is susceptible to ice accretion) by one of two mechanisms: 1) supercooled droplet icing (SDI) and 2) ice crystal icing (ICI).

Fig. 2-1 Ice formation on W24C-2 engine inlet during flight test campaign at the NASA Glenn Research Center [11].

In the last decade, ice crystal icing became a primary research focus after the occurrence of a large number of engine power-loss events (over 100 cases), for which the majority of these have been attributed to ICI [15–21]. In one particular event, the pilots were unable to restart the engines, but were fortunately able to complete a successful landing [18]. Recorded altitudes of such engine power-loss events indicated that they occurred at atmospheric conditions where the airborne water molecules would generally be frozen, thus indicating ice crystal icing [22,23]. As such, the FAA has revised existing icing certification requirements and established new ICI requirements for aircraft pertinent to jet engines, and substantial work (both in the industry and academia) is being undertaken to understand the mechanisms and effects of engine icing from ice crystals, as well as those from supercooled droplets.

To allow a more comprehensive understanding of engine icing, it is essential to identify the following factors: 1) when icing occurs (the atmospheric conditions), 2) where it occurs (the engine component sites), 3) how it occurs (in terms of thermo-fluid icing mechanisms) and 4) the impact of its occurrence (engine operation and/or component response to icing). These four aspects are introduced below and then discussed in more detail later in this review.

In terms of when icing occurs, both SDI and ICI are strongly tied to the environmental conditions. Both SDI and ICI are more likely to happen when the atmospheric water concentration (typically defined in g/m^3) is significant but are differentiated by atmospheric temperature. As notionally indicated in Fig. 2-2a, SDI primarily occurs at temperatures between 0°C and -15°C while ICI primarily occurs at temperatures below -40°C. Both types can occur for intermediate temperatures [15,24–28]. These temperature regimes generally correspond to altitudes regimes since higher altitudes are generally associated with colder temperatures. This relationship is shown in detail in Fig. 2-2b by outlining the FAA guidelines of Parts 25 and 33, Chapter I, Title 14 of the Code of Federal Regulations (defined as envelopes) [12]. These envelopes are based on statistical assessment of atmospheric icing, which is a function of potential flight altitude and temperature exposure conditions. In particular, these guidelines are for small supercooled droplets (Appendix C, Part 25), freezing drizzle and rain (Appendix O, Part 25), and ice crystal icing (Appendix D, Part 33), where it can be seen that a set of recent engine ICI events occurred within the Appendix D envelope, indicating again the importance of ICI.

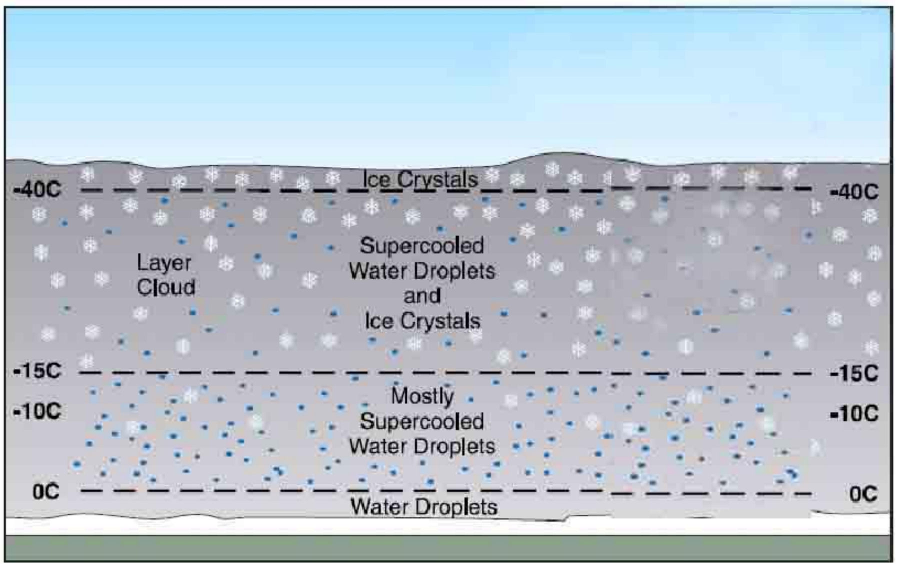

(a)

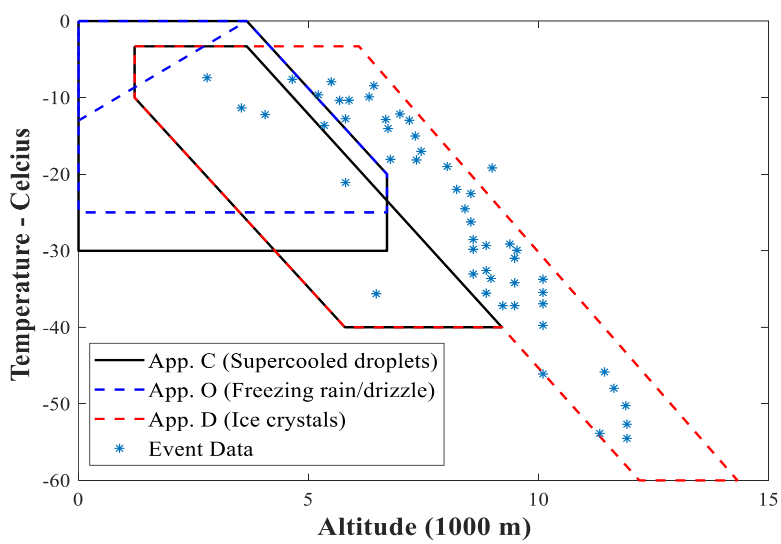

(b)

Fig. 2-2 (a)Variation of atmospheric water phase with temperature [29], and (b) FAA icing 14 CFR envelopes with appendices associated with supercooled droplets, mixed-phase and ice crystals combined and a set of recent engine icing events [12–14,22,23].

In terms of where icing occurs in the engine, different components of the engine will have different types of icing accretion. This difference is due to the variation of local temperature and velocity along the flow path [30], resulting in various engine problems. In general, the SDI tends to occur in the front of the engine and ICI tends to occur inside the engine.

In terms of how engine icing forms, the mechanisms are significantly influenced by heat transfer between the water and engine hardware surfaces. SDI occurs by the impact of supercooled water droplets that freeze immediately upon contact with engine hardware surfaces or soon thereafter. This type of accretion is dependent on many thermo-fluid factors [30] including: liquid water content, droplet size distribution, cloud temperature, flight conditions, flow field, exposure time and geometrical features of the engine surfaces. The mechanisms of ICI are more complex and occur in a mixed-phase environment with accretion and shedding depending on factors such as heat transfer, melt ratio, particle size, and humidity. The lack of understanding of ICI physics has triggered NASA research plans for this type of engine icing, as discussed by Addy *et al.* [18].

In terms of the impact of its occurrence, icing on engines is problematically associated with the shedding of the accreted ice and/or the blockage of flow. In particular, engine ice accretion, both from SDI and ICI, results in the following problems: mechanical damage (e.g. bent compressor blades), unwanted vibrations of rotating parts (due to unbalance from accretion or after partial ice shedding), and temporary thrust/power loss due to flow blockage (e.g., rollback, stall/surge, and even flameout) [30–32].

Despite the importance of engine icing, there is no published comprehensive survey on this topic to the authors' knowledge that addresses most of or all of these four aspects. Furthermore, there is no publicly-available review that discusses the mechanisms and engine component impact of ICI. The majority of published surveys [1,33–41] on the icing topic focuses more on the aerodynamics (e.g. wings), ice adhesion physics and measurement, icephobic surfaces, anti-icing systems, and icing in marine operations rather than propulsion. As such, this manuscript provides a summary of current knowledge associated with these four aspects of engine icing and explains the key differences between SDI and ICI.

Section 2.2 discusses when and where icing occurs. It begins with a focus on the environmental conditions that cause engine icing, including the atmospheric water phase and the aero-thermal-fluid physics that cause specific types of ice accretion (rime, glaze, etc.) and then discusses the engine components most susceptible to each type of icing. Section 2.3 focuses on the thermo-fluid mechanisms of icing formation, considering SDI and ICI, in turn.

Section 2.4 identifies the associated engine problems including out of balance vibration, operability, temporary thrust/power loss, and component damage. Section 2.5 provides a summary of engine icing, including a table that relates icing probability to engine components, to type of icing and to type of engine problems, along with recommendations for future study.

2.2 Icing Conditions and Affected Engine Components

2.2.1 Engine Icing Conditions

In general, engine icing occurs during flights in supercooled droplets or glaciated/mixed-phase conditions in the atmosphere. As mentioned earlier, engine icing highly depends on environmental conditions (altitude, temperature, as well as water phase and concentration). These are shown in Fig. 2-2a in terms of the notional phase of the atmospheric water (liquid, mixed-phase or frozen) and in Fig. 2-2b in terms of the flight envelopes that are susceptible to icing. In addition to this dependence on altitude and temperature, the amount of ice accretion is generally proportional to the atmospheric Liquid Water Content (LWC, mass of liquid drops per volume of air) for SDI and/or Ice Water Content (IWC, mass of ice crystal per volume of air) for ICI.

Liquid water content in the atmosphere varies with temperature. Studies [15] have reported supercooled droplets were present in a wide variety of clouds between the temperature of 0°C and -40°C (Fig. 2-2a). Despite being surrounded by freezing temperatures, such droplets remain in liquid form, as they do not yet have a seed crystal or nucleus for the ice to form. Impact of this supercooled droplet with a solid (an ice crystal or a surface), will generally quickly trigger the freezing of such drops. As such, they tend to freeze immediately upon impact with an aircraft or engine surface. To characterize surface icing in supercooled droplet clouds, SDI envelopes consider both continuous (long-time exposure to icing conditions) and intermittent (short-time exposure) when specifying maximum LWC, which may be experienced in flight for Appendix C (black line of Fig. 2-2b). This envelope considers supercooled droplets with Mean Volumetric Diameter (MVD) from 15 to 50 microns, which generally occurs between 0 and 9100 m (30,000 ft) of altitude and temperatures from 0°C to -40°C [12]. Icing in these envelopes are typically associated with intermittent LWC values varying from 0.05g/m^3 to 3g/m^3, and continuous LWC that has a maximum value of 0.8 g/m^3.

For Appendix O (dashed blue line of Fig. 2-2b), droplets of MVD from 50 to 300 microns are typical of freezing drizzle, while drops with a MVD greater than 500 microns are considered freezing rain [42]. The atmospheric icing in these conditions can have LWC that exceeds 0.4g/m^3 and can extend for horizontal distances greater than 15 nautical miles [13]. An aircraft engine flying in these condition may experience ice accretion due to freezing on its components' cold surfaces, though the amount of formation depends on the air temperature, cloud LWC, droplet size, flight airspeed, and horizontal extent of the icing conditions [15].

As previously noted, most of the recent engine icing has occurred outside of the Appendixes C and O envelopes and were instead attributed to ice crystals ingestion into the engine core [15,22]. These events occurred in atmospheric conditions containing a high concentration of ice crystals [16]. These glaciated conditions led the FAA to define an envelope [14,43] as Appendix D in Part 33 (also in November 2004) for ICI as shown in Fig. 2-2b (marked in red). Such engine ICI occurs at altitudes between 1200 and 14400 m (4000 and 47000 ft), temperatures ranging from -3°C to -60°C, and at high Ice Water Content (IWC). Maximum IWC values can reach up to about 9 g/m^3 at around 9100 m (30,000 ft) [44]. These conditions are generally associated with deep convective clouds in anvil regions or warm tropical regions, which transport low-level high-humidity air high into the upper atmosphere [27]. During that atmospheric transport process, water is continually condensed and frozen as the temperature drops with increasing altitude. As a result, these updraft cores produce altitude water content that is glaciated (ice-only), or mixed-phase (ice with small fractions of supercooled liquid droplets).

In addition to quantifying the mass concentration of ice crystals (via IWC), it is important to understand the shape and size of these particles. Generally, atmospheric ice crystals are of irregular shape and may be in the form of a) individual ice crystals (e.g. plates, columns, etc.), b) aggregates of crystals such as snowflakes, or c) crystals that have collided with supercooled water droplets to form more dense and spherical particles. Fig. 2-3 shows names and images of various individual ice crystals as a function of the air temperature and the ice supersaturation, which is defined as water vapor supersaturation with respect to ice. It can be seen that the crystal shapes become more complex and larger as supersaturation increases. Aggregates of crystals can be even larger and more complex; while combination of crystals with water, can be larger still but tended to be rounder, (e.g. hail is an extreme example).

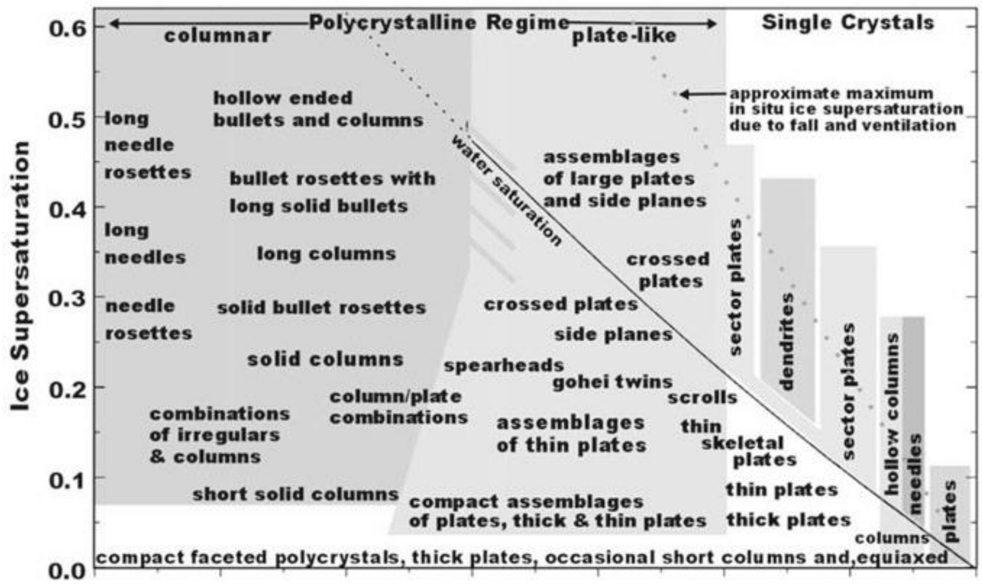

(a)

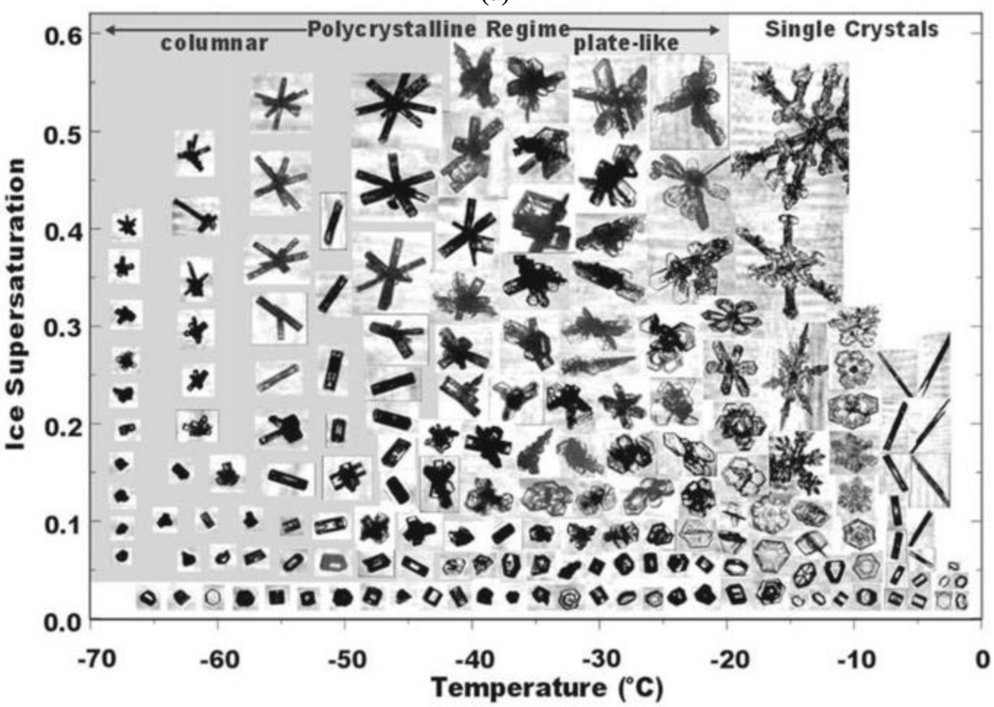

(b)

Fig. 2-3 Names (a) and images (b) of ice crystals as a function of ice supersaturation and air temperature in HIWC clouds [45]

Fig. 2-4 shows samples of ice particles found in atmospheric conditions pertinent to engine ICI. As shown, these particles are generally smaller than 1 mm. The larger particles (>300 microns) are often rime ice particles and aggregates, and are generally limited to 2 mm in size. Even larger particles such as graupel and hail can occur, but these are generally uncommon with respect to engine icing as their size (and thermal inertia) is too large for them to partially melt and refreeze in an engine. However, they may be of threat after fragmentation that could occur after impact on various engine components.

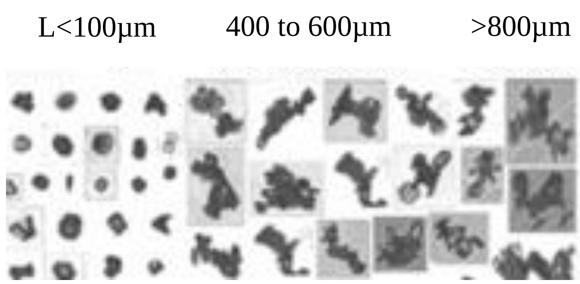

(a)

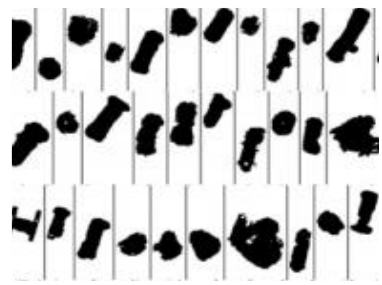

(b)

Fig. 2-4 Images of ice crystals at engine ICI conditions for: (a) an altitude of about 11 km and temperatures of -50 to -45 °C [24,46], (b) an altitude of about 10 km and temperatures of -45 to -25 °C with IWC above 1.5 g/m^3 where the vertical lines indicates a length of 1.3 mm, as shown by arrow [47].

To characterize a length scale for a non-spherical particle, one may employ the Mass Median Diameter (MMD), which is defined as the diameter of a solid sphere of ice having a mass equal to the average mass of the crystals in a given cloud. Recent studies [15,24,44,45,47–50] have revealed that the ice crystals responsible for engine ICI generally range from 200 to 2000 microns in size, where size is not necessarily correlated with IWC. For example, data from recent High Altitude Ice Crystals (HAIC)/High Ice Water Content (HIWC) flight campaign revealed that areas where ICI occurs are primarily composed of small ice crystals [27,47] of about 200-600 μm. This suggests that high IWC regions occur in and above growing convective regions where small ice crystals are nucleated in large quantities [27]. However, as shown by the time traces of ice particle size in the atmosphere in Fig. 2-5, high icing content events (TWC as high as 2 g/m^3) can have a wide variety particle size distributions, with some particle's sizes below 200 μm and some above 1000 μm. However, other atmospheric studies [50] suggest that ice crystals MMDs tend to decrease with increasing TWC, as well as decreasing temperature.

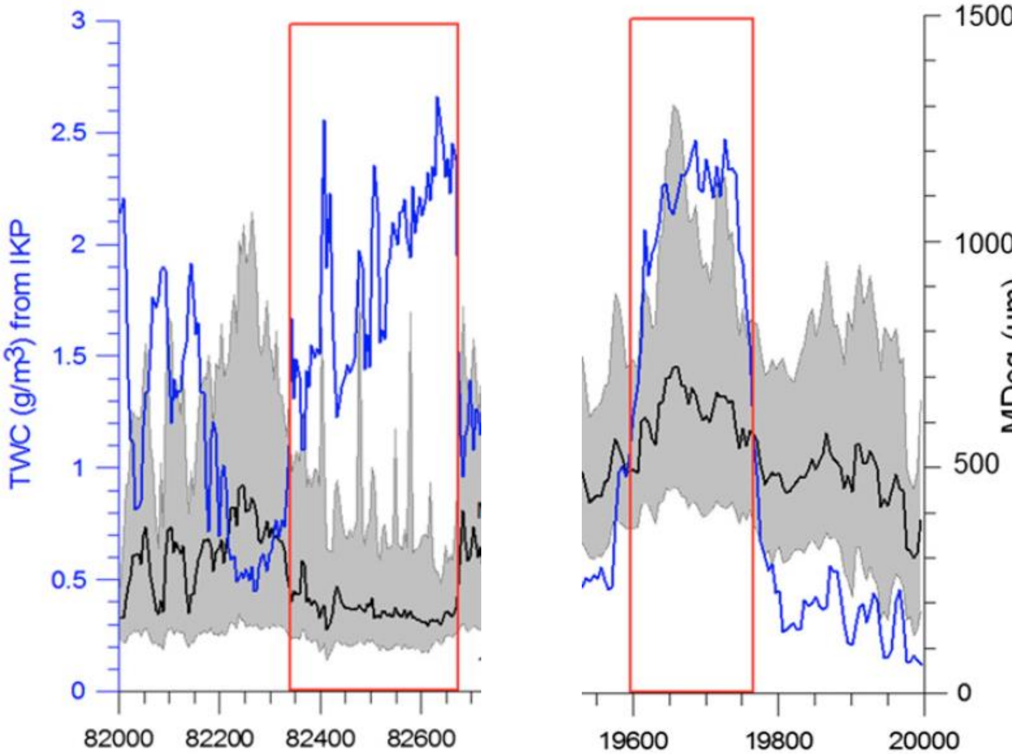

Fig. 2-5 Measurements series of TWC and particle mass equivalent diameter and size over time (seconds) at -37 °C air temperature and altitude of about 10,000 meters [47], where first high TWC event (first red box) shows small particle sizes, while second event (second red box) show much larger particle sizes.

2.2.2 Icing Affected Engine Components

Ice accretion on aircraft engine components has raised safety and performance concerns. The degree of ice accumulation depends on the state/phase of the incoming water (whether supercooled droplets or glaciated/mixed-phase particles) and the local operating conditions of the engine associated with an individual component. For a conventional turbofan, the engine's components affected by icing [1, 3, 11, 38, 48] are identified in Fig. 2-6 and include, but are not limited to: inlet casing, spinner, fan blades, exit guide vanes, splitter, splitter inner and outer walls, core inlet guide vanes, and the first-stage compressor blades/vanes. It should be noted that the components identified in Fig. 2-6 may have different names depending on the engine manufacturer and hardware integration. For example, the first stage compressor blades/vanes are also called Low Pressure (LP) blades/vanes. In addition, engine inlet and core flow-path instrumentation and other components may be influenced by icing conditions.

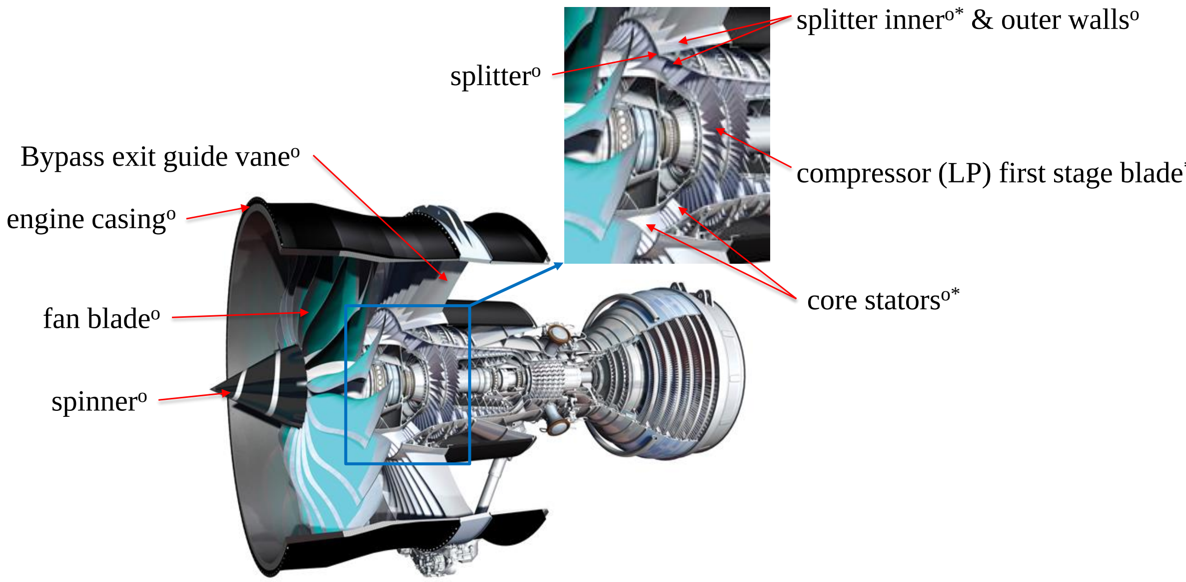

Fig. 2-6 Turbofan schematic [52] showing engine components generally susceptible to supercooled droplets icing (indicated by °) and to ice crystal icing (indicated by *).

When flying through SDI weather, the components most affected are those with surface temperatures below freezing [15]. In particular, the engine inlet/forward components (spinner, fan blades, casing) have a higher chance of experiencing SDI (than the engine core components) as they are first to encounter the supercooled droplets, which generally freeze upon contact. The list of affected components can be shortened with the use/activation of an IPS to heat specific surfaces (via electrical heat or hot bleed air) and prevent ice accretion. However, the water content that is melted by IPS during the process can freeze just downstream of the heated area through an icing process called runback. The different mechanisms that cause freezing upon impact vs. runback ice are discussed in Section 2.3.1.

While supercooled engine icing tends to accrete similar to aircraft aerodynamic icing (with largest accumulations on leading edges), ICI occurs at different environmental condition and tends to be engine architecture dependent. However, recent ICI research [16,53] has shown that ice accretion at glaciated and mixed-phase conditions generally tends to occur at the initial stages of the engine core flow or the swan neck transition between the booster and high-pressure compressor. That region usually includes the following components shown in Fig. 2-6: the engine core stators (which may include inlet and exit guide vanes depending on engine configuration), splitter inner wall (also called booster shroud), and first-stage compressor vanes/blades. For example, Fig. 2-7 shows ICI accretion on an engine booster shroud and tandem engine core stators assembly during a test at the NASA Propulsion Systems laboratory (PSL) test facility, which was recently built to allow crystal icing conditions [27,54]. Accretions at these sites can block the airflow causing engine rollback/surge while shedding from these sites can cause mechanical damage or flameout, as will be discussed in Section 2.4.

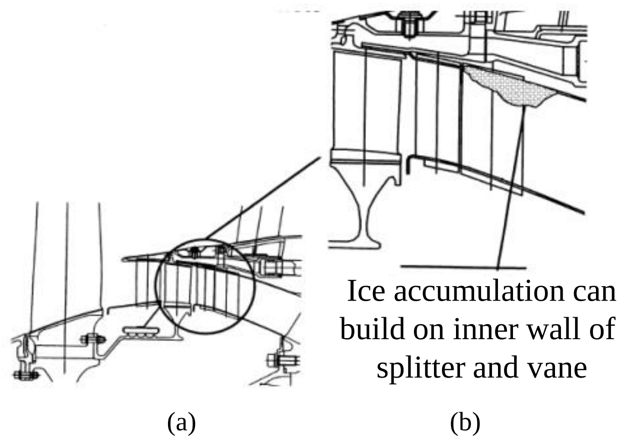

Fig. 2-7 Engine flow paths showing in a transverse view : (a) both a fan stage and core stages before ice accumulation, (b) ice accretion in the core portion of tandem stators and wall in ICI conditions [54,55].

Differentiating between engine components that are affected by SDI vs. ICI also depends on the particle size, engine flow aerodynamics, component's surface temperature, and the size and temperature of the incoming droplets or crystals. A key issue is that some engine components can be rotating at high speeds (an aspect not seen for aircraft aerodynamic surfaces). This causes differences in how particles move through the engine and how ice is accreted, but also increases the likelihood of centrifugal shedding. In terms of movement, the smallest particles (e.g. less than 10 microns in diameter) have little inertia and thus closely follow the airstream due to particle drag. In contrast, the largest particles (of 1000 microns or more) have high inertia and thus are only weakly influenced by local aerodynamics (e.g. tend to have straight streamwise trajectories until they impact a surface).

The intermediate size particles (e.g. 10-100 microns) are affected by the surrounding local aerodynamics but have enough inertia to significantly cross gas flow streamlines. For such ice particles and/or liquid droplets in the engine, the fan induces a high-speed rotational flow that drives these particles radially outward. As such, intermediate size supercooled droplets are centrifuged towards the outer bypass passage. In contrast, particles with very small inertia (small droplets) or very large inertia (large crystals) are more likely to enter the core of the engine [53]. Of these, the smaller supercooled droplets also have a smaller thermal inertia and thus quickly heat up as they move through the engine core such that they are no longer supercooled. Therefore, they do not pose an icing threat. The larger particles, especially ice particles, have higher thermal inertia due to the solid phase of water, so they tend to stay below freezing temperatures further into the core of the engine. As a result, engine core components, which are exposed to larger crystalline ice particles, are more likely to experience ICI within the compression system or downstream in the compressor transition ducts. In some instances, intermediate-size supercooled droplets may be found in the engine core, because of larger droplets breakup upon impact on the blades surface thus redirecting them into the core airflow path. These intermediate size droplets may then cause SDI on the front components of the compressor (IGV, and splitter inner wall). In terms of temperature, icing would occur if engine hardware surfaces and droplet temperatures are below freezing, regardless of the location in the engine. Small droplets would likely freeze on contact with the surface they come in contact with, while larger droplets may experience some level of runback icing. On the other hand, ice particles need some melting (by the warmer temperature of the surrounding air) to produce some liquid water that would act as a catalyst for ice accretion. As such, ICI often occurs on engine hardware components with surface temperature above freezing. Further details about icing mechanisms are discussed in the following.

2.3 Engine Icing Formation Mechanisms

2.3.1 Supercooled Droplet Ice Formation

During flight through SDI conditions, engine components at the front of the engine mostly have surface temperature, which are below freezing, thus providing a suitable ice accretion site. Incoming small supercooled droplets tend to freeze upon impact with the engine components with primary accretion on the blade leading edges and advancing pressure surfaces of rotating blades, spinners and splitters. On the other hand, larger droplets in the presence of an IPS tend to create a film of water, which then flows downstream. This water may freeze on unprotected (colder) downstream surfaces creating ridge-like ice streaks associated with runback icing [56]. These two types of SDI phenomena (freezing upon impact for small droplets vs. runback icing for large droplets) are discussed in the next two sub-sections.

2.3.1.1 Freezing Upon Contact

A schematic of the supercooled droplet freezing upon impact process is shown in Fig. 2-8, where the air, the liquid and the surface are all at temperatures below freezing (as indicated by the blue color). These droplets are already below freezing conditions but require a nucleation source such as a surface impact to undergo the phase transformation from liquid to solid. Since these smaller droplets freeze on contact with engine hardware, they tend to accumulate on surfaces that present the largest upstream frontal area to the supercooled-droplet-seeded flow field (e.g. leading edges and pressure-side surfaces).

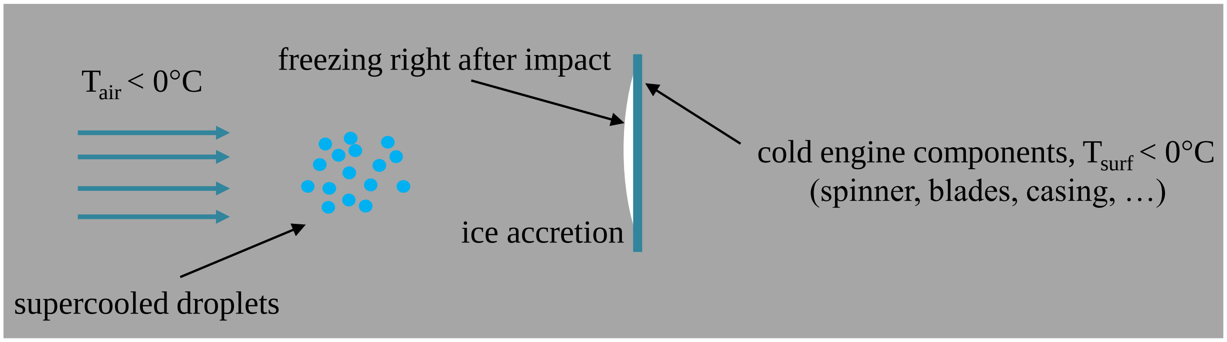

Fig. 2-8 Schematic of supercooled droplet ice formation (blue indicates temperatures below freezing and white indicates ice accretion).

The resulting ice from the process of Fig. 2-8 is generally either "rime" ice (which tends to be rough and milky in appearance, and with an overall more rounded shape) or "glaze" ice (which tends to be glassy, clear and smooth in appearance, but can have complex features, such as horns). These two types of ice are defined in the following and depend on the LWC, droplet size and the temperatures of the droplets, air and surfaces.

Rime ice occurs when the droplets freeze rapidly before they have time to spread over the surface, and before the impingement of another droplet at the same location [29]. As a result, rime ice tends to form with surface and/or ambient air temperature in the range of -15°C or less and with relatively small droplets [56,57] (e.g. 10 microns droplets), since these low temperatures and small drop sizes greatly accelerate the freezing process. Because it is composed of many individual freezing events, rime ice (Fig. 2-9a) is generally milky as it contains a high proportion of trapped air. The shape of rime ice accretion tends to be round in terms of the cross-sectional profile as shown in Fig. 2-9a.

Glaze ice, in contrast, is formed from relatively large supercooled droplets (e.g. 100 microns droplets) striking engine components with surface and/or ambient air temperatures in the range of 2°C to -10°C [56,57] as shown in Fig. 2-9b. These droplets partially freeze before the impingement of other incoming droplets. Freezing of each drop is relatively gradual, due to the latent heat released in the freezing process, allowing part of the water drop to smoothen the surface locally but also allowing the water content to move creating complex ice topography, like the horn shapes shown in Fig. 2-9b [29,58]. This glaze ice is mostly clear (ranging from nearly transparent to a somewhat opaque), and is more dense than rime ice since it has less trapped air.

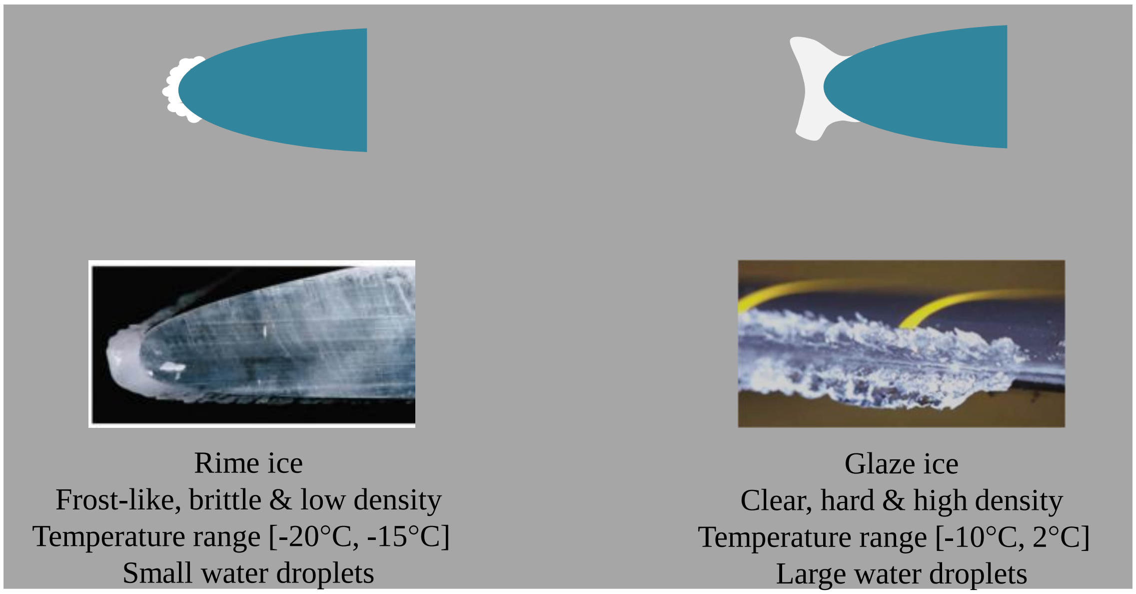

(a) (b)

Fig. 2-9 Schematics and photographs of SDI on an aerodynamic leading edges with flow left to right showing: (a) rime ice on an airfoil [59] and (b) glaze ice via in-flight horn accretion on a wing [60].

A combination of rime ice and glaze ice is called mixed ice, which generally forms in the temperature range of -10°C to -15°C. Fig. 2-10 shows pictures of rime, mixed and glaze ice formed at the leading edge of an engine inlet strut during experimental icing wind tunnel testing conducted by Dong *et al.* [61]. As shown in Fig. 2-10a, rime ice can have a shape with frosted spikes facing upstream (i.e. not always round), while glaze ice in Fig. 2-10c can have more of wavy rivulet-based surface (and is not always horned). Intermediate conditions in Fig. 2-10b give rise to the occurrence of mixed-ice, which tends to have features that are a combination of rime and glaze ice.

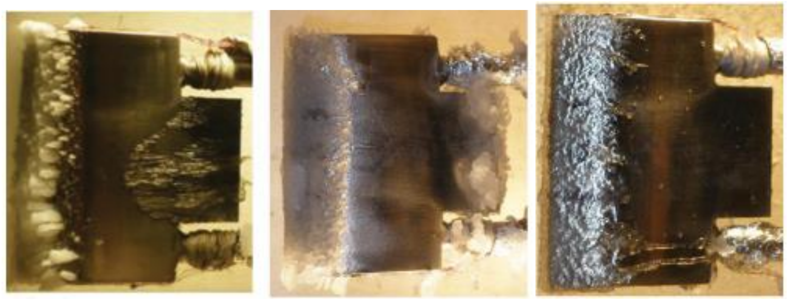

(a) (b) (c)

Fig. 2-10 Photographs of ice shape and type formed on engine strut surface under different icing conditions showing: (a) rime ice, (b) mixed ice and (c) glaze ice, with flow left to right [61].

For either rime, glaze or mixed ice, the largest factor that influences the amount of ice accretion is the atmospheric Liquid Water Content and the exposure duration, where the net amount of accretion, to first-order, linearly increases with time and LWC [62]. However, secondary factors that affect the ice accretion include droplet temperature and size, as shown by the computational ice accretion results for a two-dimensional stator cascade in a compressor stage [62]. As shown in Fig. 2-11a, larger droplet sizes produce larger ice accretions in the aft regions, consistent with other studies [29]. This is because the trajectories of large droplets tend to not be influenced by the local aerodynamics, increasing the impingement efficiency on the pressure-side of the blades. In addition, larger drops tend to have higher impact velocities and high kinetic energy coupled with impingement of supercooled liquid drops on engine cold inlet components surfaces can induce a phase change resulting in freeze upon impact [24]. As shown in Fig. 2-11b, increasing air temperature tends to reduce accretion because the colder blade increases the speed of this phase change and thus the chance of drop freezing for a fixed value of LWC.

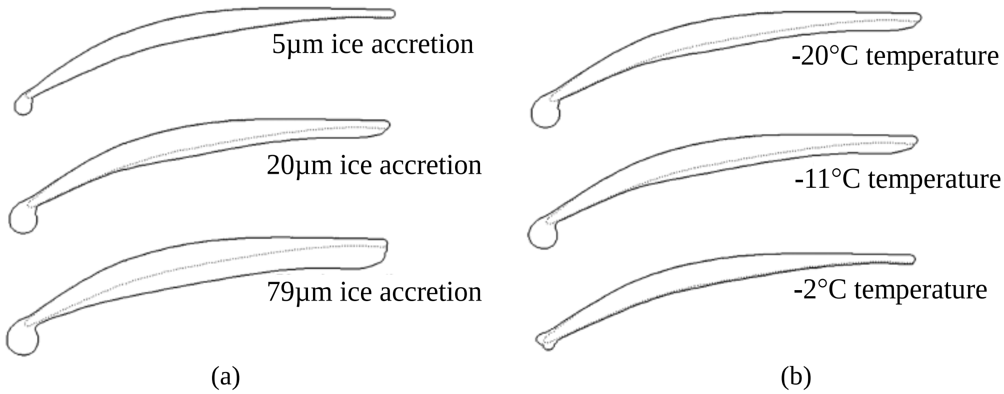

Fig. 2-11 Results of 9 minutes of ice formation at a fixed LWC for a cascade of stator blades at 40 deg AOA: (a) at different drop sizes, (b) at different atmospheric temperatures [62].

Other agents that influence the ice accretion and growth during SDI are the air velocity, the radius of curvature, and the degree of heat addition from an Ice Protection System [29,63]. To see the influence of an IPS, Dong *et al.* [63] conducted an experimental icing wind tunnel investigation on the performance of the hot-air IPS of an engine IGV. By setting the hot-air flow rate such that only partial ice accumulation occurred (insufficient heat for full ice removal), they examined the sensitivity of LWC, as shown in Fig. 2-12. As would be expected, the higher LWC values resulted in the accretion of more ice. Similarly, components with larger radius of curvature, and faster air velocity promote more ice accretion [29]. However, with the sufficient activation of an IPS in the leading-edge region of a component, the impacting droplets will not freeze since the surface temperature is warmed. However, this can lead to run-back ice, as described in the next sub-section.

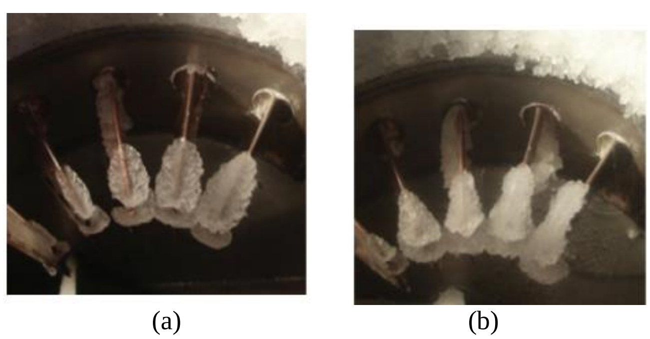

Fig. 2-12 Ice accreted on engine IGVs at a static air temperature of -8°C and a constant hot-air flow rate of 28 l/min for LWC values of (a) 0.5 g/m^3 and (b) 2 g/m^3 [63].

2.3.1.2 *Runback Icing*

In cases where an IPS prevents any leading edge freezing, the impacting droplets lead to a smooth wet zone in the stagnation region and a film of water running downstream as seen in Fig. 2-13a. As the liquid reaches the colder unprotected surface, it tends to freeze, often resulting in a ridge-shape as noted in Fig. 2-13b. The ice formed during runback icing usually results in glaze ice. Overall, the formation of runback ice is dependent on the particular ambient conditions, and the thermal properties (heat transfer characteristics) of the impingement region. For example, runback icing occurs when the surface can remove the latent heat during freezing of the droplets [2,64–68].

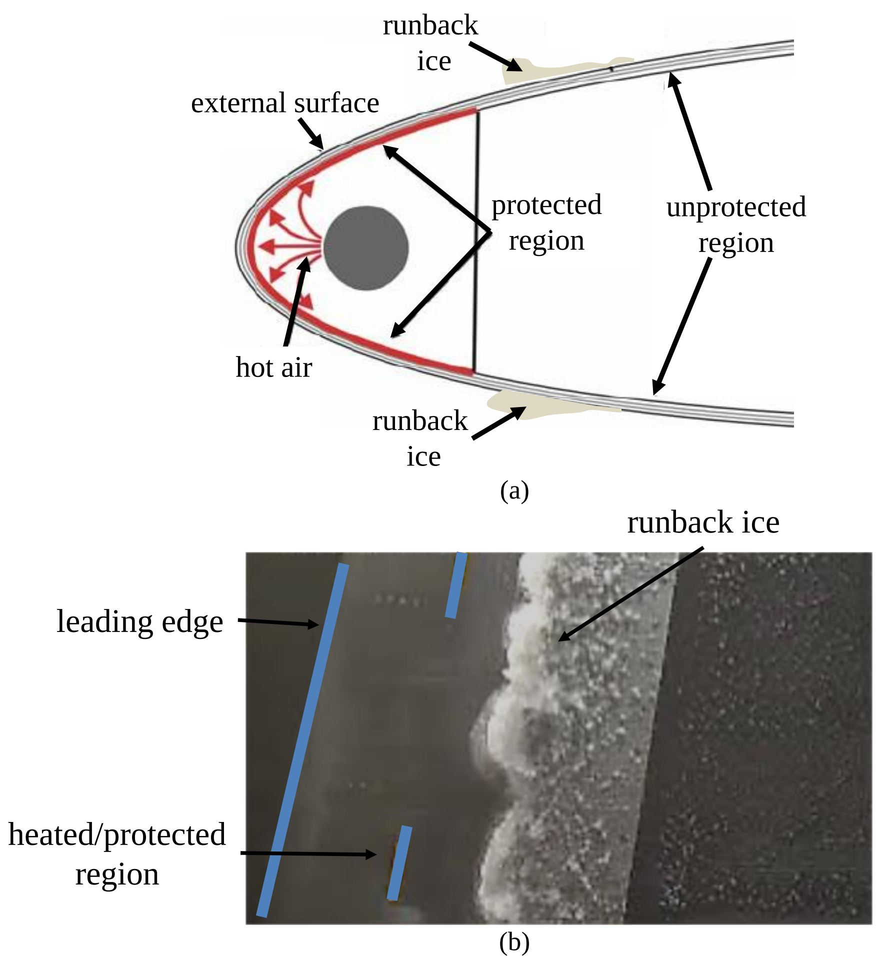

Fig. 2-13 Runback icing formation on an aerodynamic surface with leading edge heated by an IPS with a flow going left to right shown in: (a) a cross-sectional schematic [64] and (b) a photograph from above [69].

Runback ice growth is primarily influenced by temperature and velocity, and secondarily by LWC and water collection efficiency [2]. Runback icing rate is largest when the airflow velocity is high (need to move the water downstream) and the IPS surface temperature is low but above freezing, i.e. it is operating in “wet mode”. However, runback ice can be eliminated if the IPS heat is increased to the point where it is running in “evaporative mode” whereby any impacting drops are given enough heat transfer at the surface to cause full evaporation. However, running an IPS in evaporative mode to prevent all surface icing requires extensive heat addition. For example, an IPS for engine surfaces often employs hot air (Fig. 2-13a) that is taken from the compressor stage, resulting in engine performance penalties [9,10,70,71]. Therefore, it is crucial to use the hot air efficiently to minimize such penalties. While such thermal IPS generally often run continuously during flight in supercooled icing weather conditions, in some cases (relatively large droplets combined with high LWC), the heat provided by the IPS is unable to evaporate all the impinged water. As a result, water collects in a film and run back due to aerodynamic forces (running wet mode), and forms the runback ice [65,72] as shown in Fig. 2-13, which is attributed to insufficient heat [73].

As an example or runback ice on an engine strut, the engine strut study by Dong *et al.*’s [61] used a hot-air anti-icing system that was not close enough to the leading edge to remove ice in that region but was able to remove it from the middle of the strut as seen in Fig. 2-14. As a result, the middle of the strut observed a running wet mode scenario whereby the impinging water droplets created a liquid film that froze downstream as shown by the red circled regions in Fig. 2-14. A similar SDI runback phenomenon was observed by Dong *et al.* [63] and Loth *et al.* [73], who were using an IPS that was also running in wet mode. Again, both the leading edge and runback type of icing described above are a result of liquid droplet impact, whereas ice crystal icing has a different process, as described in the next section.

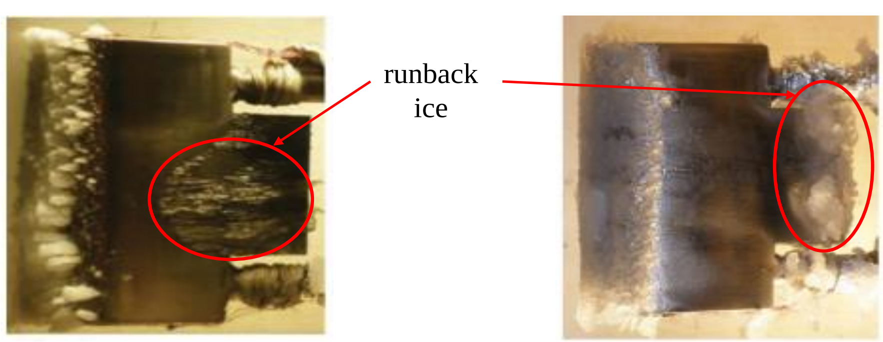

Fig. 2-14 Photographs of formation of runback ice near the trailing edge of an engine strut [61].

2.3.2 Ice Crystal Engine Ice Formation

2.3.2.1 Heat Transfer to Particles, to Surface, and to Airflow

As noted in the introduction, aircraft engines flying in glaciated or mixed-phase icing weather conditions are prone to icing, which has led to several reported power-loss events in flight. ICI in these conditions is a complex phenomenon with physics that differ from SDI. Firstly, ice crystals do not freeze upon impact and, instead, bounce off or fragment when impacting cold engine components surfaces [16,74–76], as shown in Fig. 2-15.

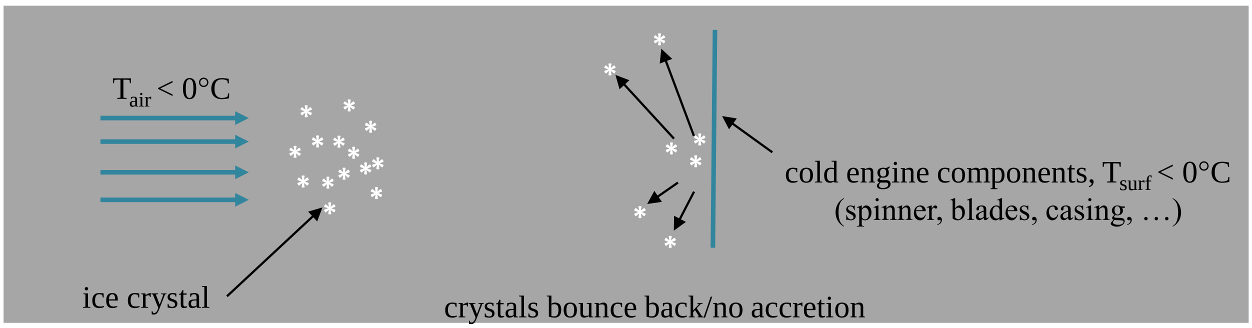

(a)

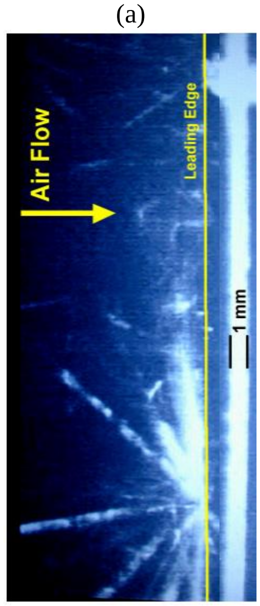

(b)

Fig. 2-15 Ice crystals bounce: (a) schematic from side (b) photo from above [74].

Therefore, investigations have been conducted to determine the cause for ice accretion with ice crystals. Studies of ice crystal trajectories in the flow-path of a jet engine [24–26,77] found that bouncing and fragmentation generally occur on the turbofan cold inlet casing, fan, and spinner (per Fig. 2-15). However, after the fan stage, the ice crystals move downstream (often with smaller sizes) and are more susceptible to melting and accretion. The most commonly accepted description is the hypothesis formulated by Mason *et al*. [15] and illustrated in Fig. 2-16. This hypothesis takes into account that the air warms up as it moves in the engine, thereby heating the crystals to near freezing and raising the temperature of the solid surface to be just above freezing. As a result, the warmed ice crystals ingested into the engine become mixed-phase and/or surrounded by supercooled droplets, thus allowing adhesion to downstream metal surfaces that are just above freezing (indicated by the orange color in top sequence in Fig. 2-16).

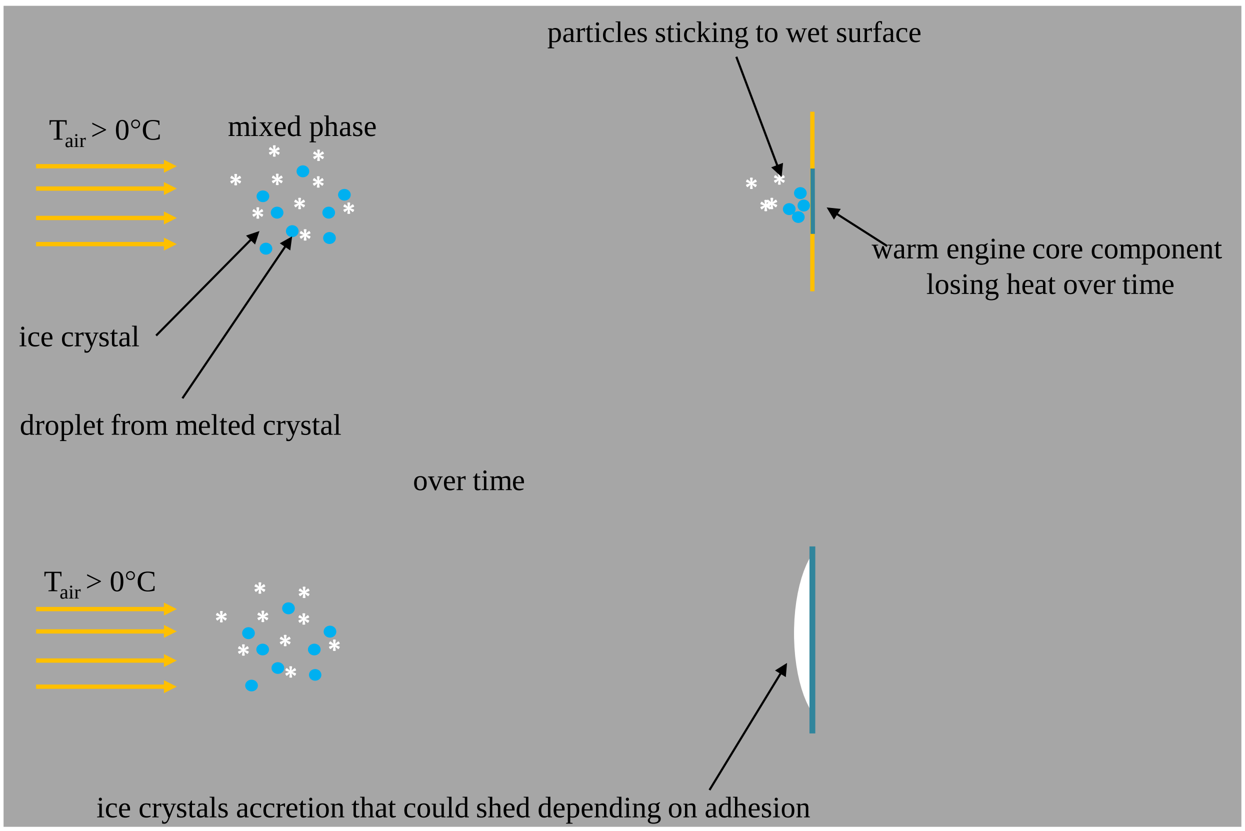

Fig. 2-16 Schematic of ice crystal icing formation within the engine core with airflow above freezing.

The subsequent impingement of more ice crystals can cause the metal surface temperature to drop below freezing, form a location for mixed-phase impingement with ice accretion (bottom sequence in Fig. 2-16). This mixed-phase accretion can then serve as a glue or a catalyst for further ice crystals to accrete. This ICI process can occur on unheated surfaces within the engine core where the local internal air temperature is initially above freezing.

Several investigations were conducted at the National Research Council (NRC) of Canada, and elsewhere to investigate this hypothesis. One of these investigations [16] employed a test rig with warm air flow that contained cold ice particles impinging on an airfoil connecting the top and bottom of a duct, to simulate an engine core stator. They observed that ice forms on the airfoil and other surfaces in the test section when the air temperature is above freezing, while no ice forms during tests when the air temperature is below freezing. This validated the Mason hypothesis, whereby ICI requires warmer air melting the ice crystals into a mixed-phase followed by the impingement of more ice crystals onto a surface for accretion. Further support for the hypothesis was based on studies [15,16] that showed ICI only occurs on surfaces when the temperature is initially above the melting point, as is generally the case for engine core components.

2.3.2.2 Influence of Internal Melt Ratio, Wet Bulb Temperature and Pressure

Mason *et al.* [15,16] found that a critical aspect that determines whether ICI will occur is the mixed-phase composition just before impact. This composition includes a liquid portion based on the local LWC and a crystal ice portion based on the local IWC. The mixed phase can then be characterized by the Melt Ratio (MR), which is the relative proportion of Liquid Water Content to Total Water Content (MR= LWC/TWC), where TWC is the sum of the liquid and ice components (TWC=LWC+IWC). Thus, a mixed phase occurs when 0<MR<1. Several other investigations [27,46,75,76,78] later confirmed that a mixed-phase (0<MR<1) is required for ice crystal accretion.

However, Mason *et al.* [15,16] found that ICI occurs in a more narrow band of MR values and proposed two conditions for the limits beyond which ICI will not occur. The first limit occurs when MR is too high and is characterized by insufficient (not enough) ice crystals to cool the surface to the freezing point or lower, or the crystals melted too much so that there is too much liquid water for impinging mixed-phase material to freeze. The second condition occurs when MR is too low and is characterized by insufficient liquid for ice crystals to stick, and to cause the surface to drop below freezing. In between these two extremes, they concluded that engine ICI would occur. This conclusion was bolstered by thermocouple measurements at the airfoil LE that showed a rapid decay of surface temperature (from ambient temperature, initially above freezing, to freezing) each time ice would form during their tests. This decrease matched the heat loss of the surface due to initial set of incoming ice crystals melting and sticking to the surface, and ultimately becoming an accretion site with the impingement of more ice crystals.

Other experimental studies confirmed that the propensity for ICI is a function of this melt ratio [79,80]. Currie *et al.* [81] conducted an ICI experiment on a crowned cylinder to further investigate the influence of MR, as shown in Fig. 2-17. For their conditions, ICI occurred for 6%<MR<31%. This MR range for ICI is similar to that observed by Struk *et al*. [80] as shown in Fig. 2-18, where ICI was found to be the most severe for MR between values of 10% and 25%. They noted that low liquid water fraction (low MR) prohibits the sticking of solid ice crystals to the surface (insufficient warming of the particles), while high liquid water fraction (high MR) results in too few incoming crystal ice particles to cool and promote heat transfer to freeze the mixture (insufficient cooling of the substrate) [16,79]. Additionally, Struk *et al*. [28] also observed poorly adhered deposits with frequent shedding when MR was sufficiently high.

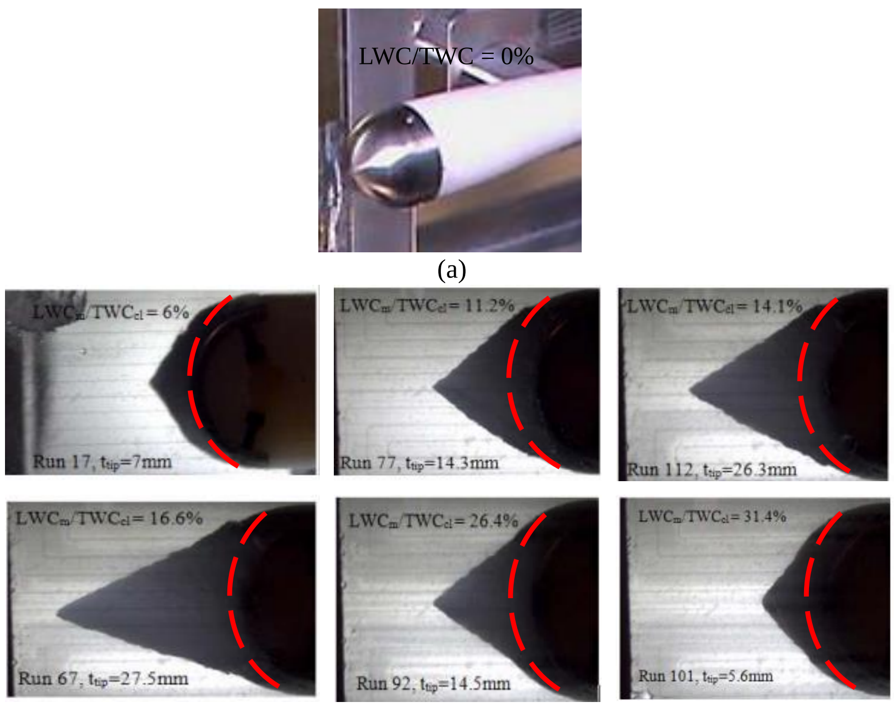

Fig. 2-17 Photos of crowned cylinder: (a) clean surface , and (b) variation of accretion growth (where red line is clean surface) with melt ratio at conditions of M=0.25, p_0=34.5 kPa and TWC=6g/m^3 [81].

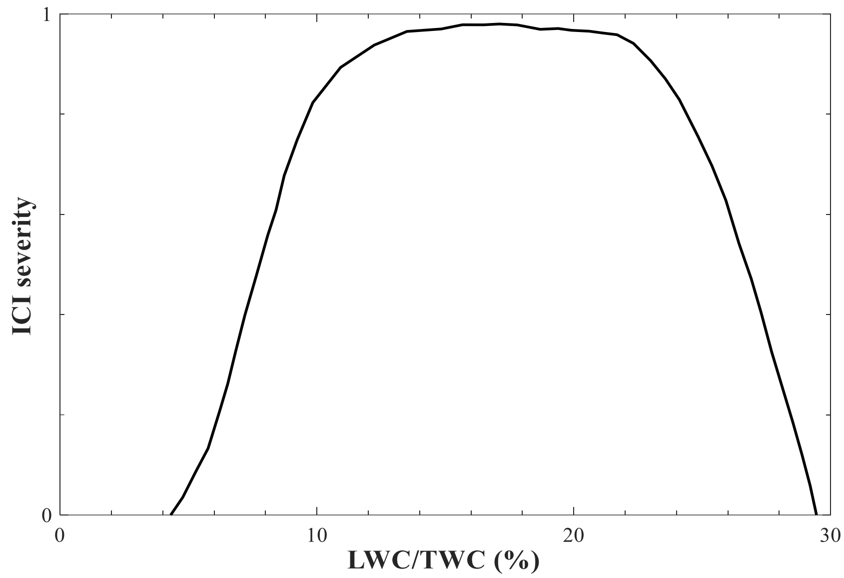

Fig. 2-18 Ice crystal icing severity as a function of melt ratio indicating a window of accretion that is highest between 10%-25% [75,81].

For a fixed airflow speed (based on a Mach number of 0.25), Currie *et al.* [81] found that the peak accretion occurred at an MR of 16.6% (Fig. 2-17). However, the MR value for peak accretion tends to vary with the airflow velocity and that the peak MR could occur in a range of MR of 10%-25% [80]. This dependency of MR value for peak accretion with airflow velocity was also observed by Struk *et al.* [80]. Currie *et al.* [81] also found that the amount ice accretion (for a fixed MR) increases nearly linearly with TWC, e.g. as shown in Fig. 2-19.

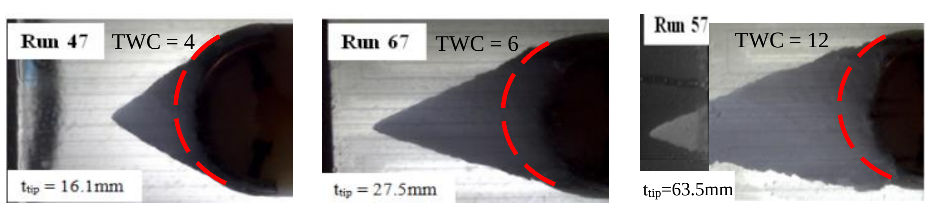

Fig. 2-19 Increasing accretions observed on a crowned cylinder as in Fig. 2-17 for increasing levels of TWC for a fixed melt ratio of 16.6% and M = 0.25 [81].

In addition to the primary influence of melt ratio, ice accretion severity is influenced by several other secondary factors. For example, Struk *et al.* [79] investigated the influence of pressure for ICI on a wedge-type airfoil and found that ice formed in mixed-phase conditions was more severe at lower pressure (45 kPa) than at a higher pressure (93 kPa). To investigate the effect of T_{wb} (temperature of a wet surface in air), Struk *et al*. [28] conducted tests with the same wedge-type airfoil and confirmed that T_{wb}<0°C produced well-adhered accretions, whereas ice formation was prevented when T_{wb}>0°C, since ice particles did not stick to the surface and were instead washed off by the aerodynamic forces. These influences on ICI accretion in simplified flow conditions should be considered in the context of actual engine conditions, which are more complicated. In particular, compressor work and component heat transfer effects can lead to large variations of T_{wb} on the surfaces as well as significant variations of pressure and temperature throughout the flow [51]. In addition, the particle trajectories, which are influenced by the velocity field and particle sizes can significantly impact ICI accretion as discussed in the next section.

2.3.2.3 Influence of Particle Size and Trajectory

Studies conducted to understand the fundamental character of ICI have also revealed that ice crystal particle size influences whether accretion occurs. In particular, very large ice crystals take more time to melt and thus are likely to produce too low of an impingement MR. On the other hand, small ice crystal may melt too much producing too high of an impingement MR. To investigate the particle size influence, Knezevici *et al.* [82] conducted an ICI test using a forward facing, inclined ramp as shown in Fig. 2-20a. Posts were added to act as stagnation leading edges for accretion and were colored for visual scales to help quantify accretion thickness. Their results confirmed that T_{wb} below freezing temperatures (after ingestion of supplemental liquid water) significantly increased accretion and ice bond-strength for a given particle size (Fig. 2-20b and Fig. 2-20c). In addition, it was noted that smaller particles (50-100 µm) yielded much larger accretion compared to larger particles (200-300 µm). They attributed this to: 1) smaller particles have reduced thermal inertia, which allowed enough melting so that the MR was closer to the peak accretion range values; 2) larger particles did not melt as much yielding too low MR for substantial ice accretion and furthermore can have an erosive effect in that they can remove accreted material upon impingement. Particle size also determines aerodynamic response times and so can influence impact velocity, as discussed in the next section.

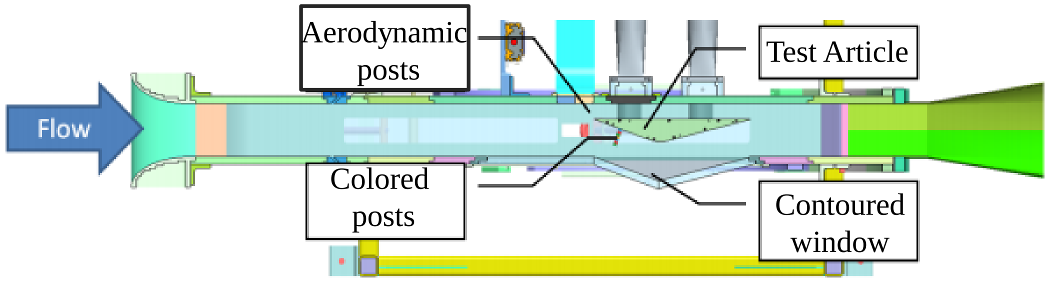

(a)

Small ice crystals

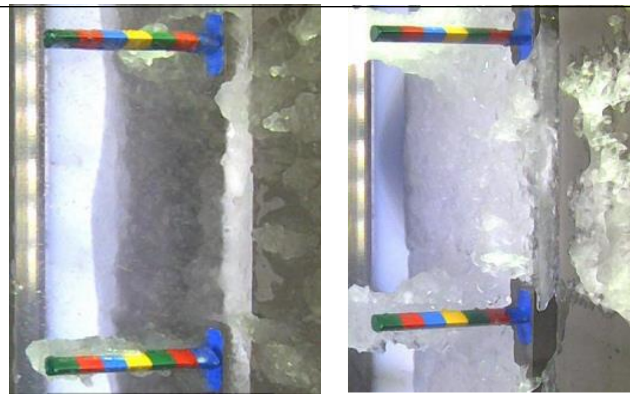

(b)

Large ice crystals

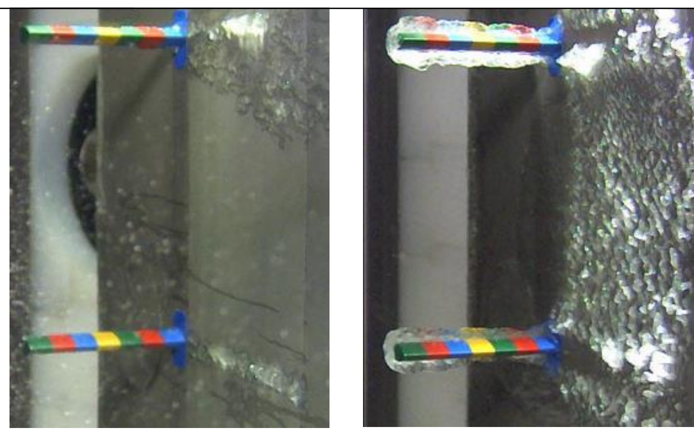

(c)

Fig. 2-20 (a) Top view of the icing wind tunnel with clean test article, (b) ice accretion from small crystals (50-100µm) viewed from the aft contoured window and (c) from large crystals (200-300µm) [82].

Impact speed can determine whether a particle bounces off or adheres to a surface, and this likelihood can be quantified by the “sticking efficiency”, which is the probability that an impinging particle will adhere to a surface (instead of bouncing off). This efficiency varies with particle size and impact speed as shown by simulation results in Fig. 2-21 [22]. It can be seen that larger particles (which are more likely to be solid ice) have a lower sticking efficiency (and thus reduced ice accretion as shown in Fig. 2-20c). In addition, higher impact speeds also have lower sticking efficiency since they reduce the time available for the phase change to occur.

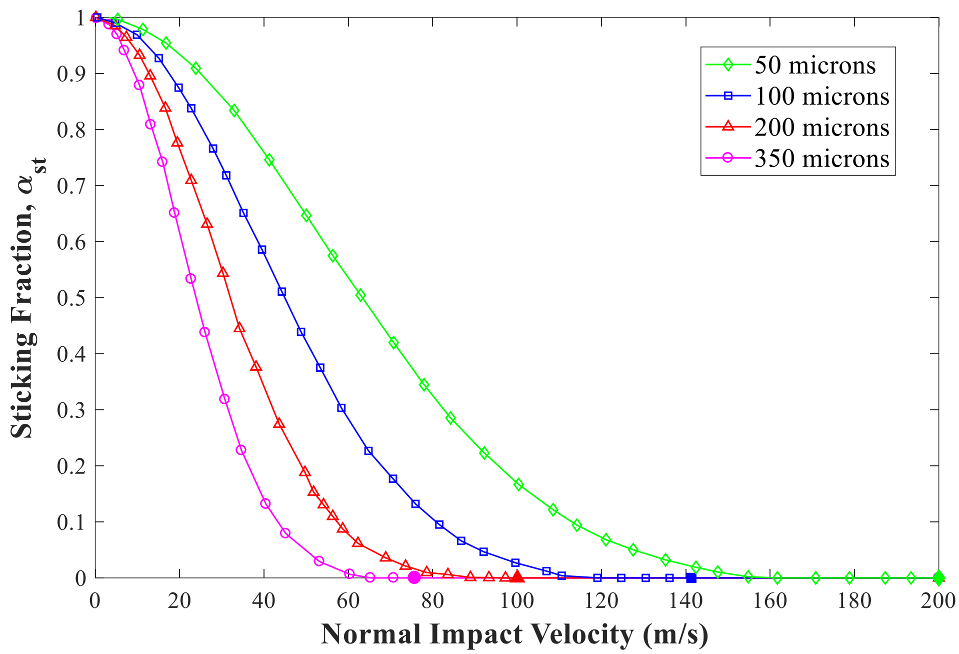

Fig. 2-21 Variation of sticking fraction with ice crystal impact velocity and effective diameter [22].

Another influence is the angle of impact with the surface. Ice crystals impacting at shallow incidence and at high velocity also have higher tangential momentum, making them less likely to adhere [75]. At high speeds, shallow impacts can have an erosive effect on existing ice, whereby they can remove accreted material upon impingement [17]. This ice erosion phenomenon was also observed during ICI test at the NASA PSL facility, where sharp arrow-like ice surfaces were observed for cases of low melt ratio [17]. This erosion effect has been observed in other experiments [74] and predicted in simulations [28], such as shown in Fig. 2-22 by Nilamdeen *et al.* [22]. In fact, if the surface is bare (no existing ice layer), high-speed shallow impacts of ice crystals can damage the surface, by causing local micro-fracture leading to surface erosion over time (like sand blasting the surface).

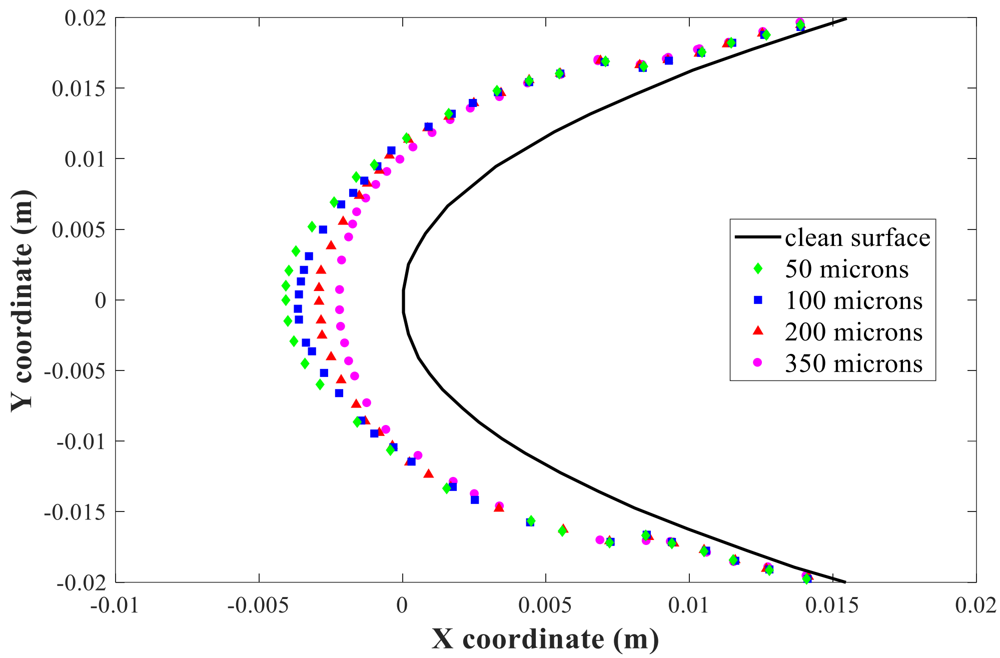

Fig. 2-22 Leading edge ice accretion reduction with increasing ice crystal sizes due to erosion [22].

2.4 Impact of Icing on Engine Performance

As mentioned earlier, icing from supercooled droplets, glaciated or mixed-phase weather conditions can affect engine airworthiness. This includes mechanical damage, unwanted operational vibrations, and aerodynamically-induced performance losses such as rollback, compressor surge/stall, and flameout. Generally, the more the accretion, the more the aerodynamic characteristics of the flowfield are disrupted [63] and the more the shedding. As such, engine problems are generally exacerbated by flight conditions that cause significant accretion. In the following, the above primary problems by SDI and then by ICI are discussed in terms of engine components (malfunction of sensors and probes are not discussed).

2.4.1 Engine Problems Related to Supercooled Droplet Icing

The mechanisms behind SDI suggest that accretion would occur on engine components with surface temperature well below freezing in the presence of LWC. The impacted components are typically near the front of the engine. As identified in Fig. 2-6, SDI accretion tends to occur on the spinner, the fan blades, the casing, the bypass EGVs, and the splitter (leading edge, as well as outer walls). SDI accretion and subsequent shedding at one or more of these listed sites can result in either mechanical damage or aerodynamic performance losses [30,71,83]. Engine performance losses (such as compressor surge/stall, engine rollback and flameout) are discussed in the next section since they are more likely to occur with ICI. However, it should be noted that these engine performance issues can occur during significant ice sheds and ingestion into the core following SDI exposures.

Ice shedding can cause structural damage downstream to the impact of the thrown ice, and is often related to centrifugal release. For example, shedding from the spinner can impact the fan blades or casing, while shedding from the fan blades to the casing, bypass vanes or splitter (e.g., erosion). Shedding from the rotating spinner or fan blade occurs when the centrifugal force is higher than the ice adhesion bond [84,85]. Generally, the ice released during shedding is centrifuged away from the core, whereby the ice fragments can impact and cause damage to the acoustic liners of the casing [30]. However, sometimes the shed ice is ingested into the core. These ice fragments can erode surfaces, but when they are large they can bend or even chip fans and blades in the compressor [30,53]. Fig. 2-23 is an example of a bent blade and a broken blade tip caused by ice ingestion in the LP compressor stage [86]. A broken blade tip is more serious as it can track downstream resulting in damage in successive stages of the compressor.

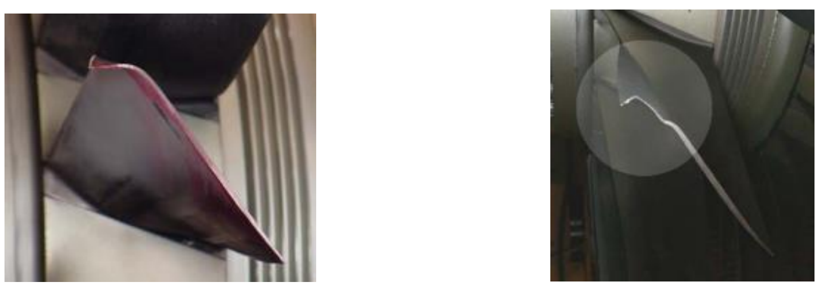

(a) (b)

Fig. 2-23 Mechanical damage to compressor blade varying from (a) bent first stage AFC blade, to (b) broken first stage AFC blade tip due to icing [86].

Another issue with shedding is that it often results in only a partial removal of the ice on a component. This is due to the stochastic nature of ice fracture and the non-uniform adhesion stress, especially on a curved surface [25,26,77]. Therefore, partial shedding can cause a mass unbalance of the rotating fan, which consequently causes an unwanted increase in the vibration level of the engine [15,31].

2.4.2 Engine Problems Related to Ice Crystal Icing

As discussed in Section 2.3.2, ice crystals ingested into an engine in glaciated conditions tend to remain in a solid state (via bouncing or fragmentation) when interacting with the colder up-front components such as the spinner and fan. After the fan, they reach the splitter where some of them go into the core while the rest exit through the bypass duct. The ice crystal particles (about 100-1000 microns in size) exiting by the bypass duct are often harmless as they are do not accrete and are too small to cause much wear or damage. However, the ice particles that enter the core flow can result in accretion at sites of the swan neck transition between the booster and high-pressure compressor such as the splitter inner wall (or booster shroud), the core stators (IGVs and EGVS) and the first stage compressor (LP) blades/vanes (Fig. 2-6). Generally, it is more likely for accretion to occur in the stagnation areas of stationary components rather than rotating. Accretion followed by shedding at these sites can lead to mechanical damage, as discussed above for SDI. For example, ice fragments shedding from the core stators or forward components of the low-pressure (LP) compressor can cause severe and perhaps disastrous damage to subsequent blade rows of the compressor [53]. However, ICI can even be further insidious as it can lead to additional engine problems such as stall, surge, rollback, or flameout as reported [14,79]. The following discuss these unique ICI engine problems.

2.4.2.1 Surge/Stall

Ice crystal accretion in the core flow of the engine compressor region (blades/vanes) causes aerodynamic blockage (and even separation). For a given power level, this aerodynamic blockage lowers the pressure rise and reduces the flow turning angle, both of which are detrimental to the compressor performance [53,62]. The net effect is a reduction of the compressor efficiency and a restriction of the compressor flow capacity [15,87]. Such detriments will affect multi-stage compression system performance since each of the stages are designed to carefully integrate with each other to provide efficient pressure rise [25,26,77]. Generally, all engine compressors are designed and built to possess a certain margin of stability in which operation is safe for its components and optimal performance can be achieved. Ice buildup on the blades and ingestion often subject the compressor blades to work in conditions far from their design point. This subsequently results in the compressor operating outside of its stability margin and ultimately experiencing stall or surge. Surge is particularly problematic as it results in rapid and substantial loss of mass flow through the core [26,77,87]. Overall, the aerodynamic influence of ice accretion and ingestion in the engine core passage generally can cause stall/surge, and reduce power [26,77]. Additionally, flow blockage resulting from ice building the core passage can also result into engine rollback, as discussed in the next section.

2.4.2.2 Rollback

As the compressor experiences continuous flow blockage due to icing, a series of events occur in which the fuel flow is decreased and the turbine is no longer able to provide the power required to drive the compressor. This subsequently result in engine rollback, which is a substantial and un-commanded thrust reduction. As such, rollback is one of the engine issues among the many encounterable during icing. A specific example is the Honeywell turbofan engine model ALF502R-5, which experienced rollback due to ICI, while flying through glaciated/mixed-phase environments. Following that event, a series of studies (flight testing and rig testing) were conducted by Goodwin *et al.* [54] to better understand the causes of the rollback event. During their flight testing with a highly instrumented engine, the rollback phenomenon was captured revealing a decrease in both the fan speed (N1) and the core speed (N2), as shown in Fig. 2-24. At the beginning of the rollback, a sharp decay in the rate of N1 was observed (marked from 1 to 2 in Fig. 2-24), while the rate of N2 only decreased slightly [15,54] (also marked from 1' to 2' in Fig. 2-24). The reduction in N2 and N1 speeds continued until the N1 found a new stable operating point, which is the sub-idle condition into which the engine settles at the end of the rollback sequence.

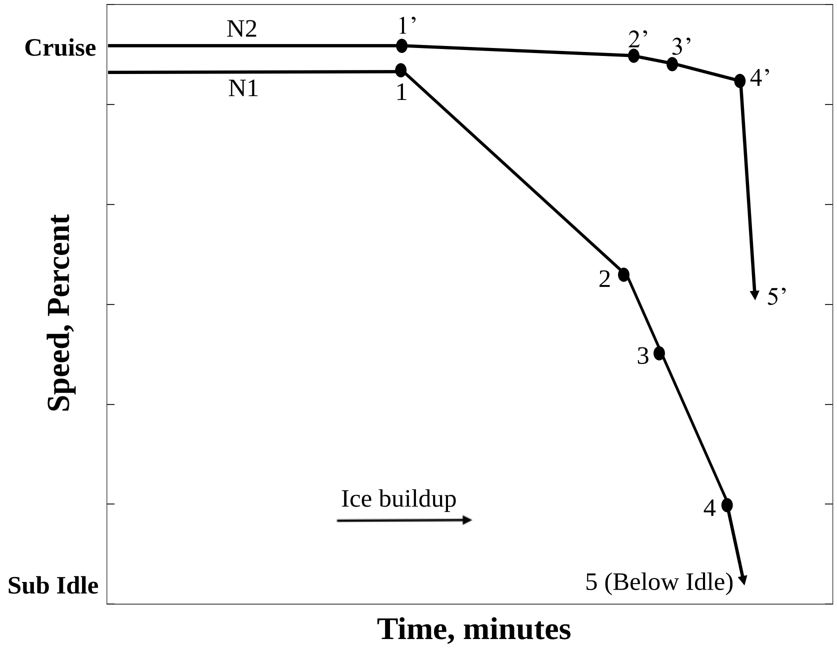

Fig. 2-24 Engine fan and core speed traces during an ICI-induced in-flight rollback sequence with 1 and 5 marking the beginning and end of the event [54].

While the data from the flight test only described the engine response during the rollback event, it did not provide direction information on how icing caused the problem. However, analysis of the fan and core speeds, were consistent with the hypothesis that rollback was caused by the gradual increase of airflow blockage in the engine core due to ice accretion. The results suggested that ice accretion on the static components such as the core stators (EGVs) and splitter inner wall (in Fig. 2-6) may be the source of this flow blockage. To investigate this further, Goodwin *et al.* [54] also conducted a thermodynamic analysis assuming a melt ratio (mixture of supercooled liquid and ice content) for which significant ICI accretion can be expected [15,16]. They confirmed that ice accretion (particularly at sites such as the EGVs and splitter inner wall) is possible at the flight conditions of rollback event (field event). As such, the analysis predicted that accretion at those sites would lead to aerodynamic pressure losses, as shown for two sets of predictions in Fig. 2-25. In this figure, curve B presents the data (solid black circle) from the actual rollback (field event), while Curves A and 2A are predictions based on mixed-phase conditions where Curve 2A had double the TWC (and roughly double the ice accumulation) as compared to Curve A. To cap the investigation, they then conducted engine tests [54,55] in an icing tunnel at mixed-phase conditions similar to flight conditions conducive to rollback event. Formation of ice was observed at the expected sites (EGVs and splitter inner wall), and a pressure loss was also noticed once accretion started, leading consequently to rollback. As explained above, the continuous pressure loss due to ice accretion at the mentioned sites triggered a series of engine reactions, which resulted into rollback.

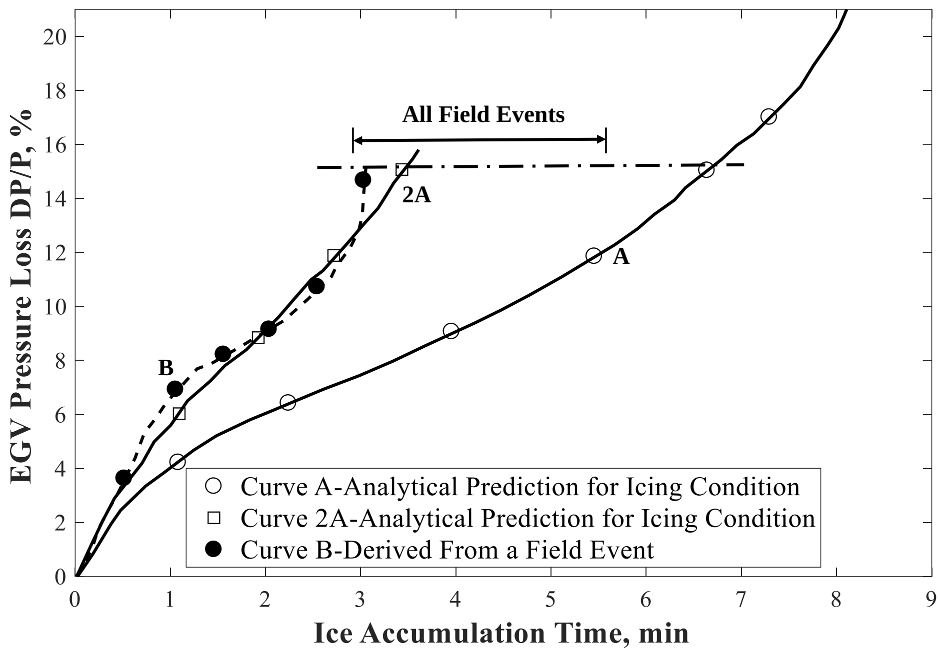

Fig. 2-25 Comparison of exit guide vane pressure loss during rollback, where Curves A & 2A are simulations predictions, and curve B is real event data [54].

Although these results were specific to Honeywell model ALF502R-5, other turbofan engines are likely to behave in a qualitatively similar manner whereby ice accretion in an engine core passage causes flow blockage and pressure losses, potentially leading to rollback.

2.4.2.3 Flameout

Another consequence of ice accretion and shedding on/from the engine core components is engine flameout, where the combustion process completely ceases (complete loss of engine power). In general, there are two primary mechanisms that cause engine flameout [25,26,77]: the loss of combustion stability and low combustion efficiency. Combustion stability is described as the steady-state ability of the flame to remain burning over a wide operating range, and is dependent on fuel, air and a source of heat to make the two previously listed items burn. As such, there exist both a rich and a weak limit to the air/fuel ratio for a given combustion chamber at a given pressure, temperature and flow speed. A typical flame stability loop is shown in Fig. 2-26. Outside of this stable region, the flame usually extinguishes by quenching. When blockage occurs due to ICI, it interrupts the air flowing to the combustion chamber, thereby reducing the air/fuel ratio [53]. The presence of ice in the flow stream also can cause a temperature drop in the combustion chamber, and the controls systems will indicate the need for an increase in fuel to recover temperature, which also reduces the air/fuel ratio. Thus, icing can cause a low air/fuel ratio from blockage and/or a fuel increase and the resulting fuel-rich condition can cause the combustion to drop below the stable region, leading to flameout [25,26,77,88].

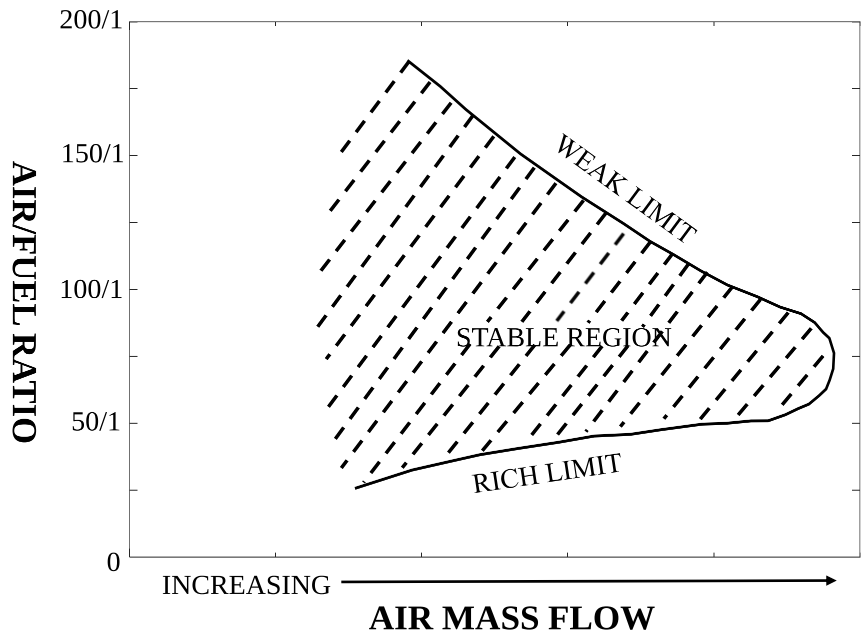

Fig. 2-26 A typical engine combustion stability with stable region bordered by weak and rich limits [25].

2.5 Engine Icing Summary

2.5.1 Engine Icing Summary via icing type, conditions, accretion and problems

Icing on aircraft engine surfaces can threaten flight airworthiness and safety. In order to better understand the state-of-the-art and to identify issues for further study, a review of published studies of engine icing was completed to consider when engine icing occurred (icing weather conditions), where it occurred (affected components), how it occurred (engine-icing mechanisms) and the impact of its occurrence (various problems resulting from icing of specific engine components).

It was shown that there are two distinct types of engine icing: supercooled droplet icing (SDI) and ice crystal icing (ICI). SDI engine icing is a well-studied phenomenon with well-established certification and flight envelopes that include continuous and intermittent maximum icing cloud weather conditions documented in FAA Appendix C. In addition to these envelopes, freezing rain and drizzle conditions are defined in FAA Appendix O. Icing tunnel experiments and flight tests have revealed that engine components susceptible to SDI include the spinner, the fan blades, the inlet casing, the IGVs, the bypass EGVs, the splitter, and the splitter outer walls. During SDI, droplets either freeze upon impact or (if impacting a heated section) create a liquid film that moves downstream by aerodynamic forces and then freezes in the unheated portion, resulting in runback ice. The ice formed by SDI could either be rime or glaze depending on many factors such as droplet size, LWC, ambient/surface temperatures, impact speeds, etc. Notably, SDI only occurs if the iced component of the engine has a surface temperature below the freezing point.

ICI is a more recently recognized and less documented phenomenon, but one that can lead to an engine core accretion and flow blockage, which can cause a host of engine operational performance issues that have led to many icing-related flight incidents. The ICI weather generally occurs in anvil regions near deep convective clouds and the FAA condition is defined in Appendix D. ICI accretion generally occurs on engine core passage components in the swan neck transition between the booster and high-pressure compressor, notably the core stators (IGVs & EGVs), the splitter inner wall (or sometimes called booster shroud), and the first stage (LP) compressor blades/vanes. The mechanisms of ICI include transport of a mixed-phase fluid (via both LWC & IWC) towards a surface and the heat transfer and thermodynamics of the surface. Generally, a mixed-phase accretion occurs with ICI and the resulting semi-liquid film acts as glue for more incoming ice crystals to adhere to at the mentioned sites. The surface is cooled by this accretion, such that the mixed-phase can turn into solid ice depending on many factors such as TWC, ice crystals sizes, T_{wb}, MR, etc. Over time, the resulting ICI accretion can grow and then shed.

In addition to the when, where and how of icing, attention must be paid to the impact of its occurrence. Ice accretion and shedding during SDI or ICI can result in a wide range of engine problems such as mechanical damage, rollback, compressor stall/surge, or flameout. SDI accretion, which occurs on the stationary and rotating parts at the front of the engine, often leads to shedding which may cause mechanical damage and/or an increase of engine vibration (due to mass imbalance). On the other hand, ICI occurs on the core components and is more likely than SDI to cause flow blockage that may result in rollback and compressor stall/surge. Subsequently, an engine flameout may stem from the ice accretion blockage and/or the ingestion of shed ice from these core components. However, since much is still unknown about ICI, the Ice Crystal Consortium [18] (ICC), a group formed of engine and airframe manufacturers has been created to improve understanding and coordinate the additional work.

2.5.2 Recommendations for future work

While there have been many studies investigating SDI and ICI on engine components and simple surface, there are many outstanding issues that are not yet understood regarding the accretion process in modern engines. These include aspects of ice formation, of ice adhesion, and ice impact.

In terms of ice formation, there are mature computational tools for SDI accretion, but predictive capability for accretion in glaciated/mixed-phase conditions is much less developed and validated. Such tools are critical to develop in order to better understand and accurately model ICI accretion to help support engine design and performance in icing conditions. These tools can help address issues of scaling [7] since sub-scale testing can lead to a different type and amount of ice accretion for an engine component.

In terms of ice adhesion on surfaces, models for ICI conditions are not well developed as there is little experimental. While SDI has much more adhesion data, the results are often inconsistent [89] and focus primarily on aluminum surfaces and not the advanced surface materials used in newer engines (e.g., titanium, composites, etc.). Furthermore, the influence of surface curvature and thermal gradients that are abundant in modern engine components have been largely unexplored in terms of ice adhesion.

In terms of impact, further study is recommended to better quantify the relationship between ice shape and roughness flow blockage and pressure losses in complex engine flow paths. Moreover, the impact of high-speed shed ice on a surface in terms of the resulting breakup and damage outcomes has not been well studied for engine icing conditions.

Chapter:

3 A compact icing research tunnel for ice adhesion characterization

3.1 Introduction

Atmospheric icing presents a threat to many human-made devices with examples including icing of electrical power networks [90,91], wind turbines [92–94], communication towers [95], and aircraft [96–102]. As such, innovative solutions to the icing problems are needed [103]. To that end, icing research wind tunnels have been built at various locations around the world to improve the understanding of the physics of ice accretion on various objects, particularly aerospace impact ice. These tunnels are designed to approximately replicate atmospheric supercooled water droplets impacting various objects at different conditions.

The NASA Icing Research Tunnel (IRT) and the Cranfield Icing Tunnel (CIT) are respective examples of large and medium-sized icing wind tunnels. Built in 1944 and renovated in 1999, the IRT at the NASA Glenn Research Center is the largest icing wind tunnel in North America in terms of test section size [104,105]. It is a closed-loop design tunnel, which has a 1.8 m high by 2.7 m wide by 6 m long test section, as shown by the plan view schematic in Fig. 3-1a. The contraction area ratio into the test section is 14:1. The IRT is equipped with a 3728 kW (5000 hp) electric motor, which can generate a maximum airspeed of almost 175 m/s (390 mph) in its test section [106]. The IRT contains a heat exchanger, which allows icing tests over an air temperature range from -35°C to 5°C [107]. It has ten spray bars with high water flow rate standard nozzles and low water flow rate MOD-1 nozzles that produce supercooled water droplets with Mean Volumetric Diameters (MVD) ranging between 14 and 275 microns. This spray system can form a 1.2 m (4') high by 1.8 m (6') wide ice cloud, with LWC ranging from 0.15 to 4 g/m^3. The IRT test section can operate from sea level (at 0 m/s) to 914 m (3000') altitude (at 134 m/s). While extremely capable with a large test section, this facility is expensive to maintain and operate, as it requires a team of operators and engineers.

Commissioned in 2004, the Cranfield Icing Tunnel design goal was to enable investigation of atmospheric icing effects across a broad range of applications including; aviation, shipping, ground transport, power lines, wind turbines, buildings, and vegetation. The CIT was designed to allow investigation of the growth, structure, and shedding behavior of ice accreted on test specimen structures. It also includes the ability to evaluate the ice adhesion strength on multiple samples in a single test session. Fig. 3-1b shows a plan view schematic of the CIT. The essential components of the icing tunnel include a 400 kW cooler, which enables icing test temperatures between -30°C and 5°C, and a fan driven by a diesel engine, which is capable of providing a maximum flow of 100 kg/s. The icing tunnel test section size is 760 mm x760 mm with airflow velocity that can reach up to a Mach number of 0.5 (170 m/s). The spray system consists of six spray rake bars with a total of 99 nozzles located in the tunnel contraction area, approximately 3 m upstream of the test section. The location of the spray bars in the tunnel contraction section enables the droplets to be launched into the air, which is already moving at significant speed, decreasing the probability of larger droplets falling out of the flow [108]. The nozzles create a uniform cloud of droplets with diameters ranging from 20 μm to 300 μm and LWC varying from 0.05 to 3 g/m^3. The LWC of the cloud is achieved by activating the desired number and location of nozzles [109]. A similar technique is used in the IRT to achieve a targeted LWC. Overall, this facility allows moderate size test section specimens, enabling faster set-up and turn-around times at a more moderate cost.

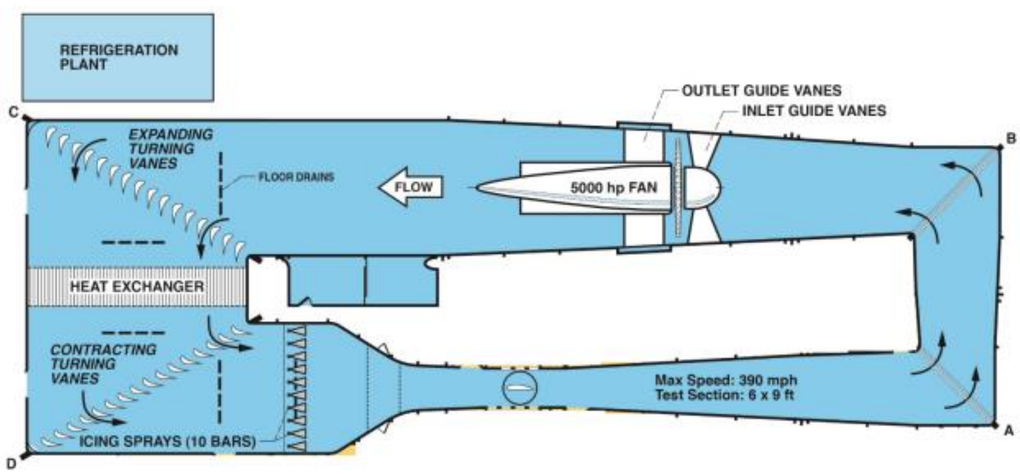

(a)

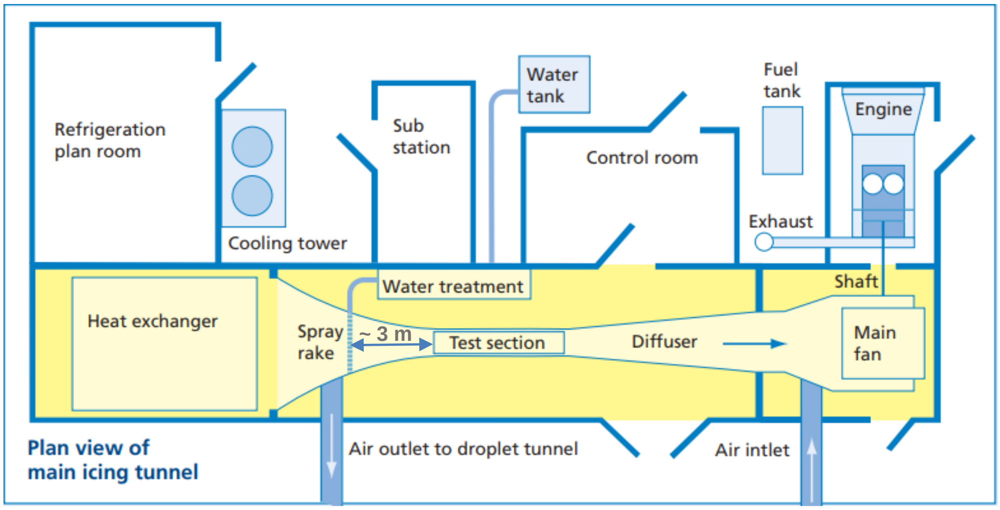

(b)

Fig. 3-1 Schematic of (a) the NASA Icing Research Tunnel [107], and (b) the Cranfield Icing Tunnel [108].

While these facilities have proven highly useful, the cost and complexity of the testing generally scales with the size of the facility. This is problematic if one wishes to construct a typical lab-scale facility to conduct a multitude of tests with high-fidelity ice adhesion measurements. To date, there has not been a complementary small-scale icing facility that can provide tensile ice adhesion measurement with the flow quality typical of research wind tunnels. Moreover, current icing tunnels (to the authors' knowledge) do not measure the temperature variations in their experimental substrate during accretion. Such a small-scale icing tunnel can be cost-effective while allowing rapid and robust icing evaluations of a variety of test specimens including icephobic surfaces and aerospace materials [110], and also characterizing the thermal transients and characteristics of ice adhesion [10-12].

As such, the primary objectives of this study were to: 1) describe the design, development, and testing of a novel, compact, cost-effective icing research tunnel for ice tensile adhesion testing over a wide temperature range (from -35°C to 0°C), and for Liquid Water Content (LWC) levels (as high as 2-4 g/m^3) and 2) investigate the variation in droplet temperature, substrate temperature, and tensile adhesion characteristics of impact ice vs. static ice. These important objectives have not been addressed in previous literature (to the authors' knowledge), which makes this work unique. In the following, we describe the design and development of such a facility, and then describe measurements that are the first to directly compare tensile ice adhesion and thermal transients in both static ice and impact ice within the same facility.

3.2 Design and Construction of the Compact Icing Research Tunnel

3.2.1 Overall Design

To address, cost, availability, and complexity concerns associated with testing in the large and mid-size tunnels such as the NASA and Cranfield icing wind tunnels, a small-scale icing research tunnel was designed and built using a walk-in cold chamber as the refrigeration unit. This new facility was named the Compact Icing Research Tunnel (CIRT) and is intended to enable high fidelity testing in icing at low cost and in a low space. The commercial walk-in cold chamber is used to cool the air to the targeted temperature for icing tests. This cold chamber is a 1.5 m wide x 1.5 m long x 2.1 m high, insulated heavy-duty indoor walk-in freezer from Leer, USA with an aluminum floor and a ceiling mount self-contained heat exchanger system. The heat exchanger recycles the air in the chamber through its inlet, cools it, and then re-injects it back into the chamber via its fans. The walk-in freezer has an exterior thermostat that indicates the ambient air temperature in the chamber and can operate down to a temperature of -35°C without the wind tunnel running.

Installed in the freezer is the wind tunnel with a 7.5 cm (3") by 10 cm (4") test section. Fig. 3-2 shows a schematic of the icing facility (freezer and wind tunnel), which uses a single atomizing nozzle (MOD-1) to create a cloud of droplets, with a mean diameter ranging from 10 to 40 microns depending on upstream air and water pressure supplied to the nozzle. The nozzle feed streams use deionized water and air at controlled heated temperature conditions to avoid freezing of the spray nozzle and to ensure high-quality icing in the test section. The water spray nozzle is placed approximately 0.9 m (3') above the icing wind tunnel test section and the spray can be diverted from entering the wind tunnel by use of an extendable/retractable small funnel (motorized shield here in diagram) such that spraying time and spraying quality can be precisely controlled prior to delivery to test specimens. The CIRT employs a vertical configuration rather than the horizontal configuration used in the NASA IRT and the CIT. The vertical configuration was adopted to allow a reduced floor space footprint, to maximize tunnel length within the constraint of the walk-in cold chamber, and to maximize distance of flight for the droplets (to ensure supercooling). Droplet cooling is discussed more in detail in Section 3.2.4.

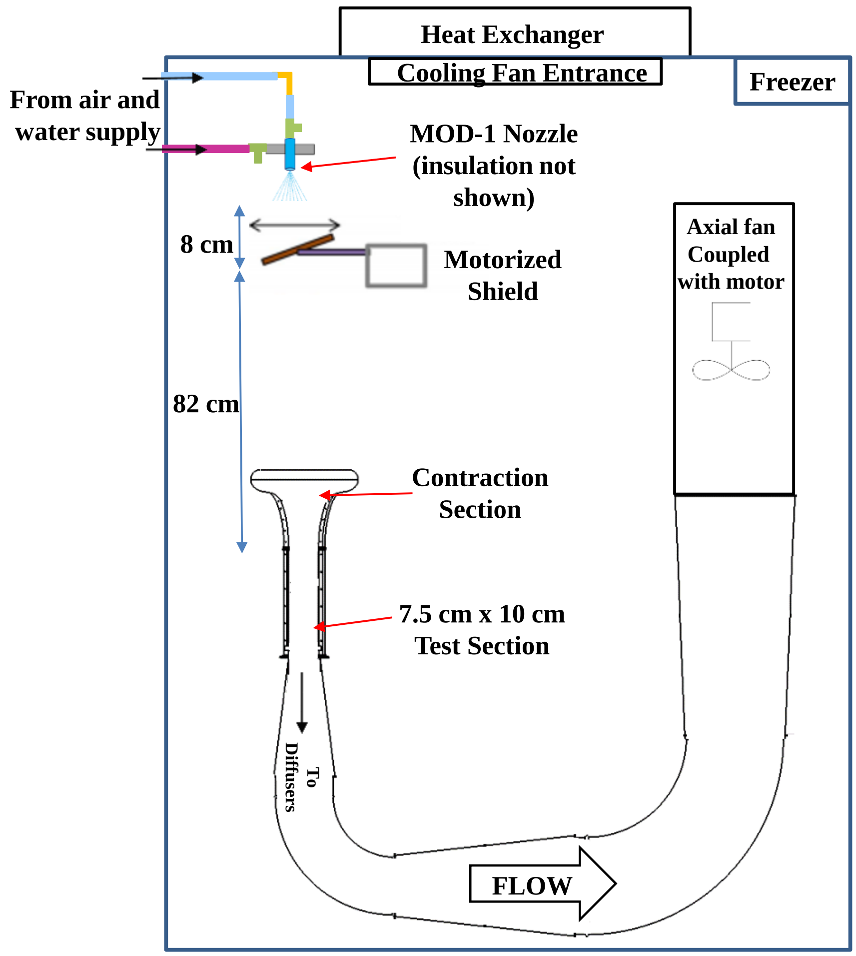

Fig. 3-2 Diagonal view schematic of the Compact Icing Research Tunnel (CIRT).

3.2.2 Aerodynamic Design

The wind tunnel components (contraction section, test section & diffusers) were designed, and 3D printed out of ABS material on a FORTUS 400. This printing method allowed a resolution to within 250 microns. Additional surface finish smoothing was achieved by the application of acetone. A computer rendering of the components' assembly and a photograph of the actual facility are shown in Fig. 3-3. The inflow to the test section included a 5:1 area contraction ratio into the 0.3 m long test section; this was followed by three sets of diffusers creating an effective U-turn of the flow. The exit of the wind tunnel path included an in-line axial fan (maximum RPM of 3709) powered by a 3 phase 1.5 kW (2 hp) electric motor.

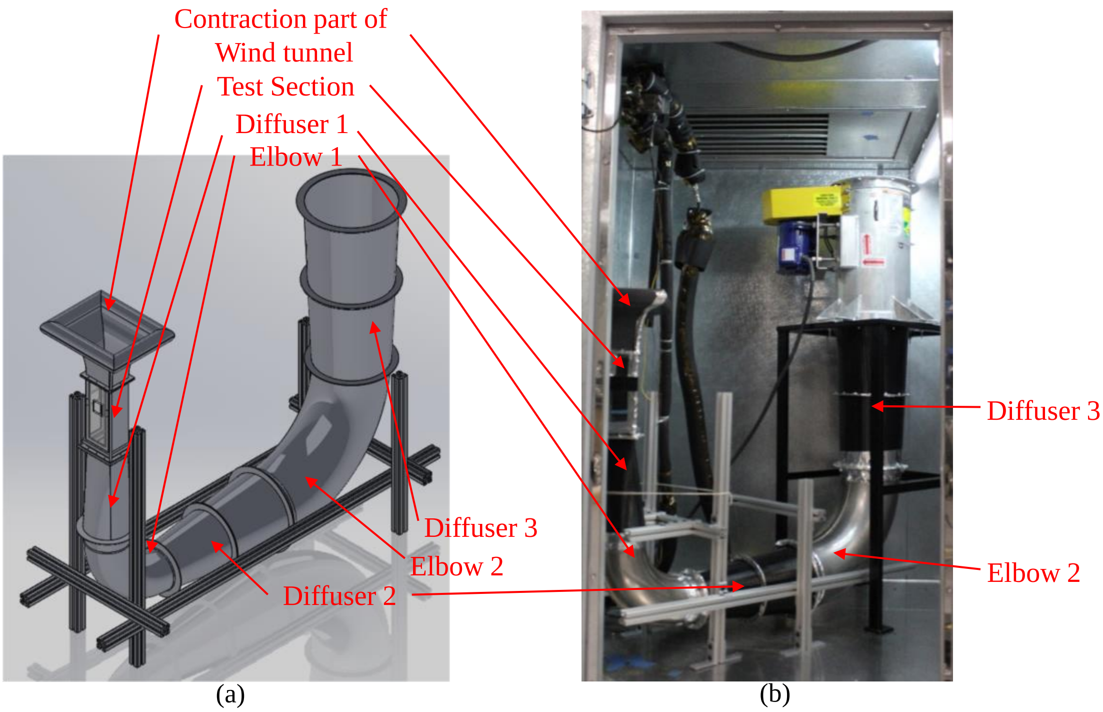

Fig. 3-3 Computer model (a) and real image (b) of assembled Compact Icing Research Tunnel.

The three diffusers and the two connecting elbows were designed to maximize test section size and flow velocity within the space constraints of the walk-in cold chamber. The diffuser (shown in Fig. 3-4) dimensions were defined and optimized to minimize pressure drop within the system, and to achieve maximum test section speeds. The pressure drop for each diffuser was estimated as described in [111]. The system pressure loss for a measured wind tunnel test section velocity of 40 m/s includes a loss for each component, as tabulated in Table 3-1. The wind tunnel was then assembled as shown in Fig. 3-3a. Pitot-tube measurements of air velocity at different RPM of the fan indicated airspeed values to within 2% of one another in a space area of 6.5 cm x 8 cm at the center of the test section. These findings suggested a reasonably uniform flow in the wind tunnel test section. Similarly, air temperatures measured by thermocouples installed at various locations in the walk-in cold chamber and the wind tunnel test section indicated values to within 1°C, suggesting uniform temperature profile in the CIRT test section.

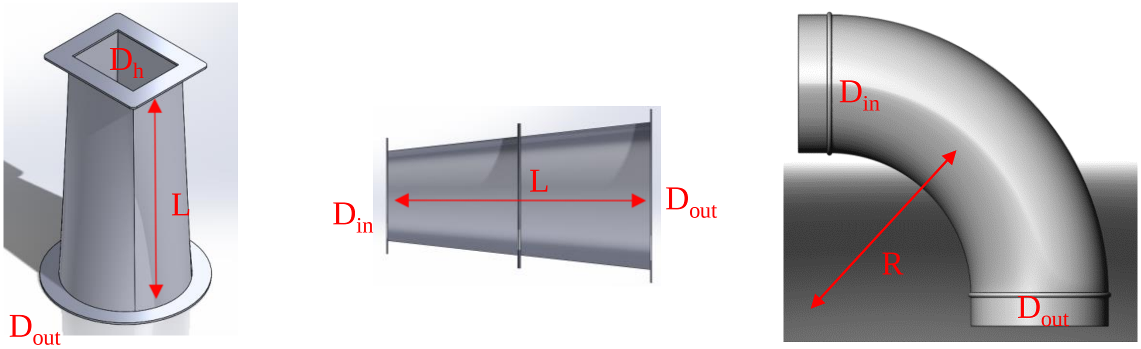

(a) (b) (c)

Fig. 3-4 Renderings of: (a) Diffuser 1, which includes a rectangular to circular cross-section change and a length L, (b) Diffusers 2 & 3, which have a circular cross-section with length L, and (c) example elbow with a centerline turning radius R.

Table 3-1 Component dimensions and estimated pressure losses for a test section velocity of 40 m/s.

System Pressure Loss				
Part	**D_h or D_{in} (m)**	**D_{out} (m)**	**L or R (m)**	**ΔP (Pa)**
Diffuser 1	0.1	0.2	0.3	72.7
Elbow 1	0.2	0.2	0.2	35.3
Diffuser 2	0.2	0.25	0.4	25.9
Elbow 2	0.25	0.25	0.4	4.7
Diffuser 3	0.25	0.3	0.6	1.2
			Total	139.8

3.2.3 Spray System Characteristics

A single MOD-1 nozzle, shown in Fig. 3-5a & b was used to generate a supercooled droplet cloud above the wind tunnel test section, as also shown in Fig. 3-2. The MOD-1 nozzle used heated water and air (filtered beforehand) to prevent freeze-out in the nozzle while dispensing the supercooled droplets' cloud at the targeted air temperatures of the test section (which are significantly below freezing). For a -20°C test section air temperature, the supplied air and water temperatures used prior to entering the walk-in cold chamber during icing tests were set at 110°C and 60°C, respectively. In the freezer, metallic hoses transporting the heated air and water to the nozzle were thermally insulated to minimize heat loss to the cold ambient air. Using a previously obtained droplet cloud calibration chart [106] shown in Fig. 3-5c, the MOD-1 nozzle could produce a droplet cloud with MVD ranging from 10 to 40 microns depending on the supplied air and water pressures. It should be noted that the horizontal axis values of Fig. 3-5c chart are the difference between water and air pressures (psid). For air and water supply pressures of 138 kPa (20 psig) and 414 kPa (60 psig = 40 psid (water-air)) respectively, the calibration chart indicates a water droplet cloud with a MVD of 20 microns, as shown by the red point in Fig. 3-5c. Similarly, a droplet cloud with an MVD of 13 microns could be achieved by supplying the spray nozzle with air and water with gauge pressures of 172.4 kPa (25 psig) and 241.3 kPa (35 psig = 15 psid (water-air)) respectively, as shown in Fig. 3-5c by the green point.

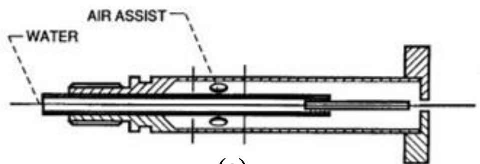

(a)

(b)

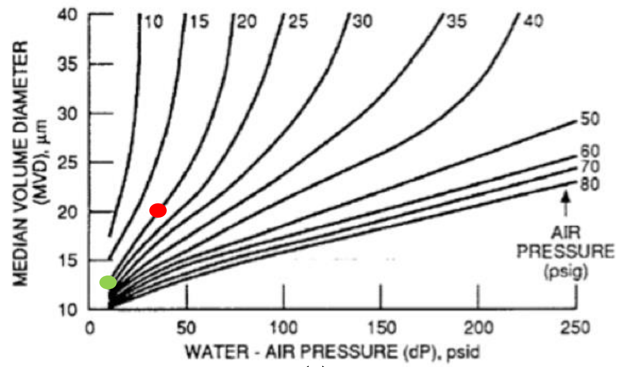

(c)

Fig. 3-5 Droplet spray: (a) schematic of MOD-1 spray nozzle, (b) photo of nozzle, and (c) droplets' cloud calibration chart [106].

The predicted Rosin-Rammler (R-R) mass-based probability distribution function (PDF) droplet size distributions for the two conditions of the MOD-1 (MVD of 13 microns and 20 microns, as noted in Fig. 3-5c) and the CIT's nozzle (MVD of 20 microns) are compared in Fig. 3-6. Also shown is the measured mass-based PDF for the MOD-1 nozzle for an estimated MVD of 20 micron droplet cloud [112,113]. The comparison shows that both icing tunnels (CIRT & CIT) have approximately the same predicted PDF shape for a 20 micron MVD cloud. The smaller droplet (13 microns) cloud, also shown in Fig. 3-6 shows a shift of the MOD-1 PDF to the smaller sizes, as expected. This condition with smaller droplets (MVD of 13 microns) was selected for icing tests in the CIRT as it demonstrated the best combination of high but reasonable liquid water content (LWC) and high-quality ice. The ice quality was achieved by employing small droplets to ensure supercooling before impact within the available (and relatively short) time-of-flight for the spray. This time-of-flight was quantified for the CIRT and compared to that for the CIT as described below.

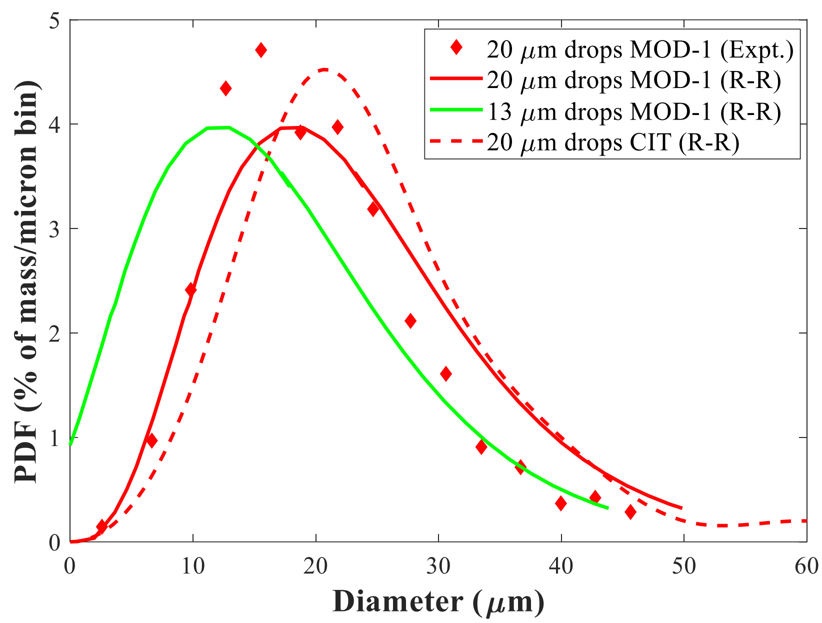

Fig. 3-6 Experimental droplet size distribution shown as symbols and Rosin-Rammler (R-R) shown as lines for various MVD cases, where the 13 micron Mod-1 MVD is used in the present study.

Flow rates were recorded during all tests using Omega meters (FLR1008-D for water and FLR1204-D for air) installed on the MOD-1 nozzle air and water supply lines to monitor any variations during icing tests. Air and water flow rate meter readings were 22 ± 0.5 L/min and 100 ± 2 mL/min, respectively, for nozzle test conditions of 137.9 kPa air gauge pressure and 413.7 kPa water gauge pressure.

3.2.4 Droplet Time of Flight Evolution

As shown in Fig. 3-2, the center of the CIRT test section is approximately 0.9 m below the MOD-1 nozzle. A computational fluid dynamics (CFD) analysis of the evolution of the drop and air velocity for the quiescent spray conditions of the Mod-1 nozzle [112,113] was coupled to a 1-D area relationships to account for the wind tunnel airflow velocity. Since the time of flight for the droplet is the integral of the inverse of the velocity over the distance, the shorter CIRT would experience a smaller time of flight for the drops than that for the CIT. With the initial droplet temperature exiting the nozzle above freezing, this reduced time of flight reduction would not allow enough cooling for the droplets to reach supercooled equilibrium with the surrounding air, before reaching the CIRT test section.

To minimize this issue, the CIRT was designed to maximize the droplet time-of-flight within the freezer chamber space constrictions. To estimate the droplet temperature during its flight, Eq. (1) was used, where the

Lagrangian rate of change of the droplet internal energy is related to the heat transfer to the particle, $\dot{Q}_p$, in addition to the energy absorbed from the surrounding fluid due to any phase change.

$$m_p \frac{\mathcal{D}(c_{p,p} T_p)}{\mathcal{D}t} = \dot{Q}_p + h_{phase}\dot{m}_p \tag{1}$$

This equation can be solved analytically by assuming that the surrounding gas has a constant temperature ($T_{f@p}$=const.), the temperature of each droplet is uniform internally, and that one can also neglect convection and only assume conduction. In this limit, the resulting heat transfer is proportional to the droplet surface area, the thermal conductivity and the temperature gradient. Furthermore, if one assumes no heat transfer, a constant density of the droplets and a constant specific heat, the change in the droplet temperature (T_p) relative to the initial value exiting the nozzle ($T_{p,t=0}$) is a function of the ratio of time relative to the droplet thermal response time-scale (τ_T) as

$$\frac{T_p(t) - T_{f@p}}{T_{p,t=0} - T_{f@p}} = \exp\left(-\frac{12 k_f \beta}{\rho_p d^2 c_{p,p}}\right) = \exp\left(-\frac{\beta}{\tau_T}\right) \tag{2}$$

Using this first-order approximation for droplet temperature, Fig. 3-7 shows the temperature profile for $T_{p,t=0}$ of 60°C and $T_{f@p}$ of -20°C in both CIRT (13, 20 & 30 micron MVD) and CIT (20 micron MVD). The time of flight was based on a 40 m/s test section velocity for the CIRT data and that of 80 m/s for the CIT data. The 20 micron droplets reached the targeted temperature of -20°C at the test section in both the CIRT and CIT to within 1° C, based on this first-order analysis. However, it could be seen that a 30 micron droplet in the CIRT would not reach this supercooled condition, owing to its larger diameter and increased thermal response time (Eq. 2). As noted in Fig. 3-6, the mass of droplets in the range of 30 microns or more is nearly reduced by half when the MVD changes from 20 microns to 13 microns. Therefore, this smaller droplet size is expected to have a more uniform droplet temperature and better ensure a supercooled state before impingement. Such an effect must be considered when employing a small icing research tunnel that does not have a long time of flight for droplet cooling.

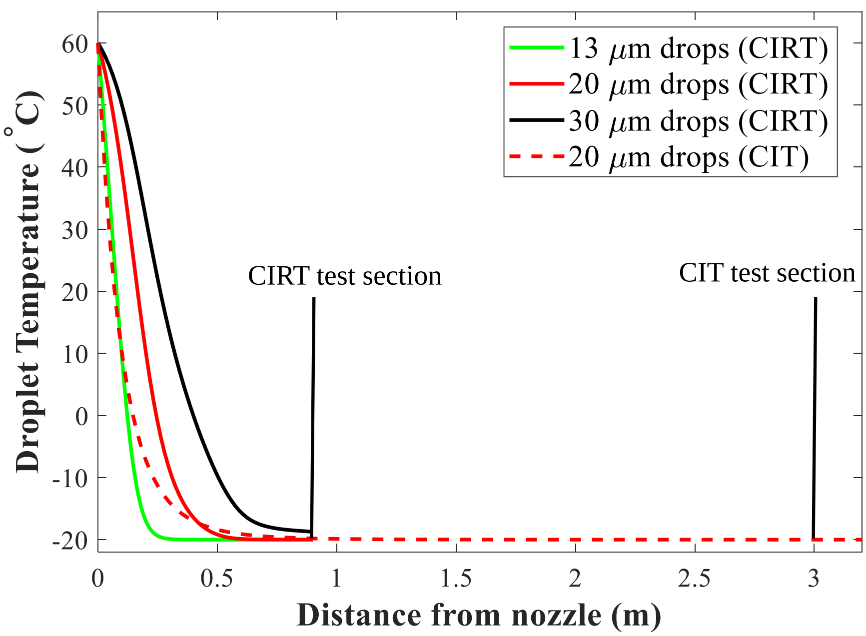

Fig. 3-7 Droplet temperature change over distance from spray nozzle to test section for various droplet sizes in the CIRT (where MVD is 13 microns for ice tensile test) and the CIT.

3.2.5 Test Section LWC

A vital control parameter for icing tests is the Liquid Water Content (LWC), defined as the mass of liquid water per unit volume. An icing blade was used to measure the LWC in the center of the CIRT test section [114]. The icing blade was made of aluminum with a thickness of 3.18 mm (1/8”) and was placed in the CIRT as shown in Fig. 3-8a. The temperatures of the filtered air and deionized water supplied to the MOD-1 nozzle were 110°C and 60°C, respectively, while the cooled air in the test section was at -20°C. The test section air velocity during the LWC measurement icing tests was 40 m/s. The spray was turned on for a total duration of 75 sec to allow an ice accretion height of about 5 mm as shown in Fig. 3-8b (the minimum suggested height is 3 mm [24]). The uniform ice height accreted across the blade, also shown in Fig. 3-8b, provided evidence of a uniform cloud in the wind tunnel test section, as well as homogeneous air temperatures and flow velocities. The test section LWC was calculated using accretion time (β_{ice}), accretion height (H) , test section velocity (V_{TS}) , blade collection efficiency (e_b) , ice density (ρ_{ice}) as follows [24]:

$$\mathrm{LWC} = \frac{\rho_{ice} H}{e_b V_{TS} \beta_{ice}} \tag{3}$$

The height of the ice on the blade was measured using an image processing software package called "ImageJ". This icing blade test was conducted for the 13 and 20 micron MVD cloud conditions and the ice density was measured to be about 927 kg/m^3. A total of 3 tests were performed using the icing blade and the results indicated average LWC values of 2.8 g/m^3 and 3.6 g/m^3 respectively for the cases with 13 and 20 microns diameter droplets.

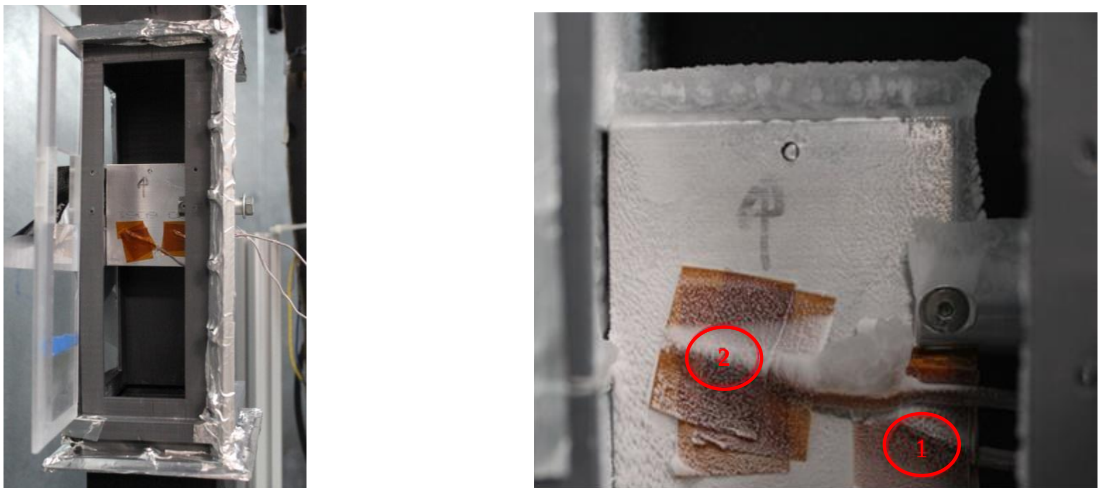

(a) **(b)**

Fig. 3-8 (a) Side view of icing blade installed in the CIRT test section for Liquid Water Content (LWC) measurement, and (b) a view of accreted ice at the leading edge of the icing blade (with good uniformity in accretion height observed) with locations of two thermocouples noted with red ovals.

3.2.6 Ice Tensile Adhesion Method Setup

The new CIRT was used to conduct ice accretion tests on an aluminum test specimen for 2 different exposure conditions and to measure ice tensile adhesion properties for: (1) impact ice (where droplets and air just upstream of test article impact at test section air velocity (nominally 40 m/s)); and (2) static ice (commonly called "freezer ice", where water is slowly poured in a container above the surface and left to freeze). In both cases, the ice tensile test consisted of applying a gas pressure acting over a "defect", a technique that was devised by Andrews *et al.* [115–117]. The defect is a plastic, non-adhering disc placed over a hole located in the center of the test substrate to prevent water from entering the pressurization channel, as shown in Fig. 3-9b. Once ice accreted on the test substrate, a measured air pressure was applied through the access port causing an upward force on the defect, which initiated the ice fracture that removed most (or all) of the ice from the substrate. The pressure at which the ice fails was called critical or fracture pressure.

The pressurization was based on slowly increasing the pressure at a rate of 131 kPa/s until ice fracture occurred. This rate resulted in an overall pressurization periods of about 5 seconds depending on the fracture pressure. This slow rate was chosen since a previous study had noted that an overall pressurization time of 0.7 seconds or longer minimizes the amount of ice residue left on substrate disc's surface after fracture and improved fracture pressure repeatability [116]. This fracture pressure was converted to fracture energy and then ice adhesion tensile strength as described in references [118–121]. A schematic of this setup in the CIRT test section is shown in Fig. 3-9a, where the test fixture consisted of a vertical aluminum boss piece (cylinder) coupled to a 30 mm diameter substrate disc (non-coated aluminum). At the fixture center is a 4 mm diameter air supply hole, which was covered by a thin (50 micron thick) Teflon disc to create a sealed surface during ice accretion. There was no recess in the 30 mm diameter disc for this Teflon disc. The Teflon defect of 7 mm diameter was maintained firmly on the disc by creating a suction force carefully controlled by a needle valve, which was attached to a vacuum pump.

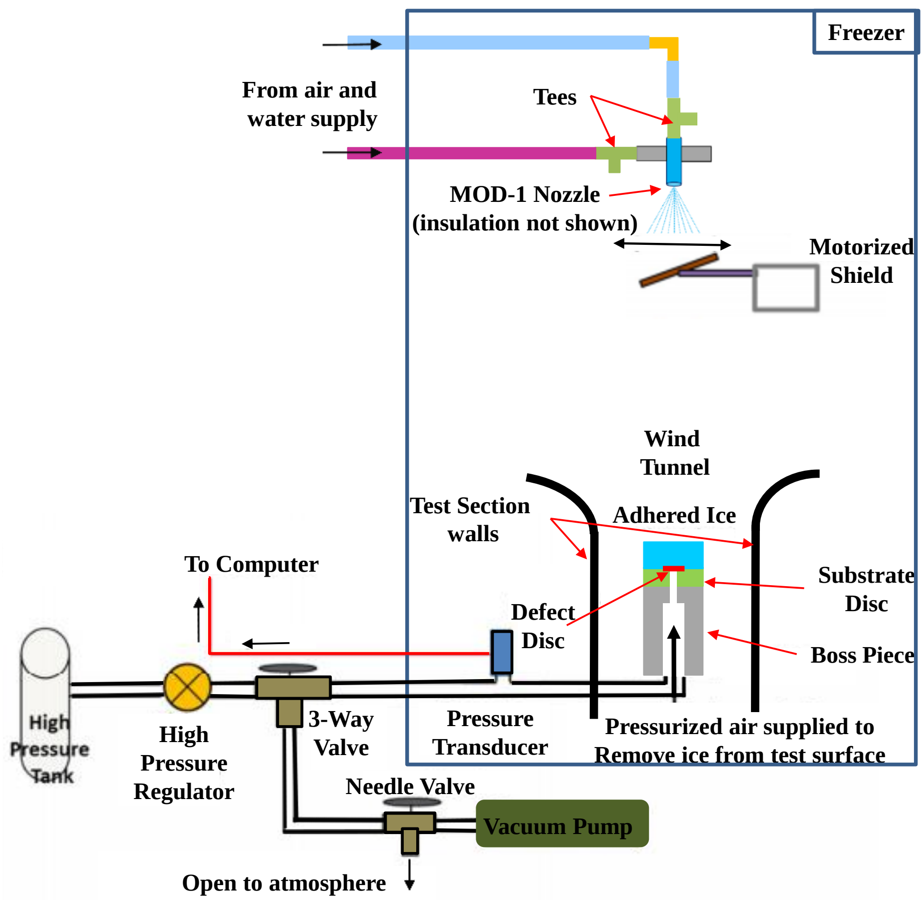

(a)

(b)

Fig. 3-9 (a) Schematic (not to scale) showing ice tensile test setup in a partially shown wind tunnel, and in (b) image of the aluminum sample with Teflon defect.

Deionized water was used for all icing tests since impurities in the water could potentially result in a larger variation in ice adhesion strength [119,120]**.** Furthermore, a single physical aluminum substrate disc, which has an arithmetic surface roughness (Ra) of 4.8 µm, was used for all icing tests to reduce variations that could be attributed to differences in manufactured substrate surface characteristics. This physical substrate disc was cleaned by wiping its surface with Chem-wipes, first dry, and then with a 95% isopropyl alcohol prior to beginning each test to also reduce ice adhesion data variation that may be caused by surface contamination. Static and impact ice accretion were then obtained on the aluminum substrate disc following procedures described in reference [122]. In particular, the impact ice tests were conducted with the 13 micron MVD droplet cloud and LWC of 2.8 g/m^3, and obtained impact and static ice on the substrate are shown in Fig. 3-10. Following the impact/static ice accretion phase, the tensile test was initiated as described earlier. This tensile test was performed for all cases (impact and static ice conditions) when the thermocouples (one each attached to the boss and substrate) displayed a temperature of -20°C. These thermocouples were inserted in one each 1 mm diameter hole drilled into the boss piece and the substrate disc and filled with high conductivity paste, which were covered by an insulation tape for an accurate temperature reading. Impact and static ice tests were each repeated 4 times since ice adhesion individual tests generally show wide scatter.

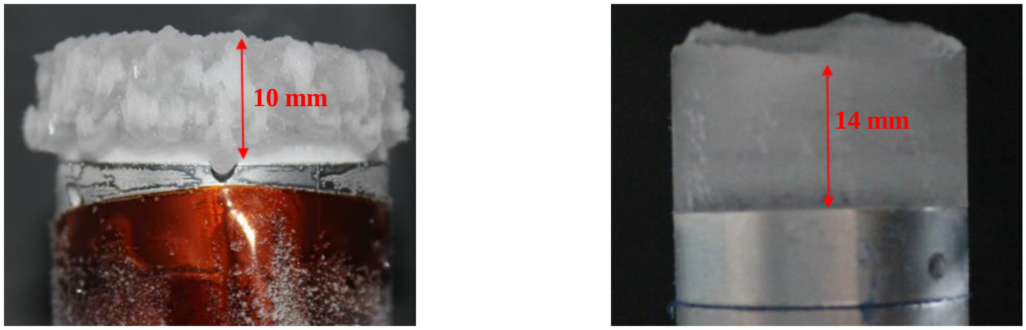

(a) (b)

Fig. 3-10 Images of accreted ice on tensile test fixture (boss + substrate disc) during (a) impact ice, and (b) static ice.

3.3 Results

3.3.1 Thermocouples and Humidity Diagnostics

The CIRT was instrumented in a way to provide a thermally well-characterized environment during all icing tests. As such, a detailed set of thermocouples was used to determine the temperatures throughout the cooling, icing and adhesion testing process. The location of these thermocouples (TCs) are shown in Fig. 3-11. TCs were inserted at various levels of the test section and locations of the walk-in freezer to measure temperature of the ambient air as it was being cooled down. These readings agreed to within 1°C of one another. Thermocouples were also installed on the spray nozzle, on the water supply metallic hose and at other specific locations to monitor temperature variation during the transient process of icing tests. Several of these TCs are shown in Fig. 3-11 with the exception of two that are installed on the surface of test specimens (e.g. the aluminum icing blade as shown in Fig. 3-8b by the red ovals, or aluminum boss piece and substrate disc). The relative humidity (RH) was also recorded during all icing tests using a Vaisala HMT130 humidity and temperature transmitter.

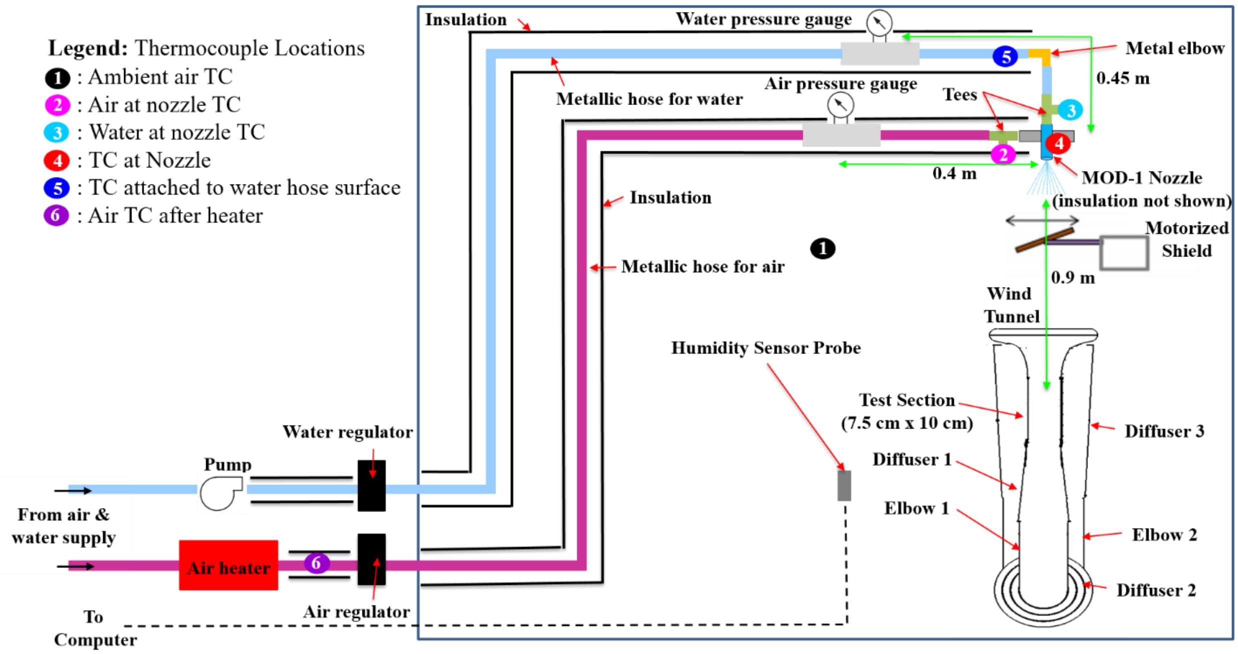

Fig. 3-11 Side view schematic of the CIRT and instrumentation.

Sample results for humidity and temperature are shown in Fig. 3-12. During all icing tests, the relative humidity at first slightly decreased, and started to increase as the air in the cold chamber was continuously cooled down (Fig. 3-12a). The relative humidity increase rate was even higher during the water on and off phase (spray time). However, this relative humidity never reached saturation. This indicates that the freezer heat exchanger effectively removes water vapor and prevents condensation and frost prior to initiation of water spray. However, these measurements also indicate that evaporation may be occurring during impact conditions.

Temperature recording generally started at the same time the freezer was turned on until turned off. An example of the temperature plot during an impact ice test for LWC measurement is shown in Fig. 3-12b, whereas the "Blade Temp." curve represents the reading from the TC located at position 1 on the icing blade (from Fig. 3-8b). It should be noted that temperature readings from TC located at position 2 on the icing blade were within 0.5°C of that at position 1. The high nozzle and water line temperatures were based on the goal of preventing water freezing until the spray was turned on. It could be seen that the water and the atomizer/nozzle temperatures slightly decreased in the very first seconds before reaching an almost steady state right after the spray was turned on, hence the purpose of a pre-test spray sequence (contained by the shield).

During the icing blade tests for the LWC measurement, and before the spray is turned on, the two thermocouples attached to the blade revealed its temperature to be at equilibrium with the targeted ambient temperature of about -20°C. However, upon impingement of the first droplets, the blade surface temperature increased (by about 3°C) due to the latent heat of freezing (energy rejection associated with phase change) of the droplets being transferred to the aluminum blade. This is a phenomenon also observed by Jin *et al.* [100]. Similar to the case of the icing blade, the two thermocouples attached to the boss piece and substrate disc revealed an increase in temperature of the boss piece and substrate disc at the droplet impingement during tensile adhesion impact ice tests due to latent heat rejection from the phase change followed by a decrease afterward as shown in Fig. 3-12c. This temperature increase was however higher than that of the icing blade's case, since the boss piece/substrate disc assembly has more thermal mass compared to the icing blade. Furthermore, the substrate disc or coupon displayed a slightly higher temperature compared to the boss piece due to the fact it is the part of the assembly that experienced the droplets impact and thus directly absorbed more of the droplets latent heat rejection. This absorbed heat was then transferred by conduction to the boss piece. Likewise, a thermocouple inserted in the boss to monitor its temperature change during static icing tensile tests revealed the same temperature increase phenomenon once the room temperature deionized water was poured into the cylindrical mold made around the test fixture.

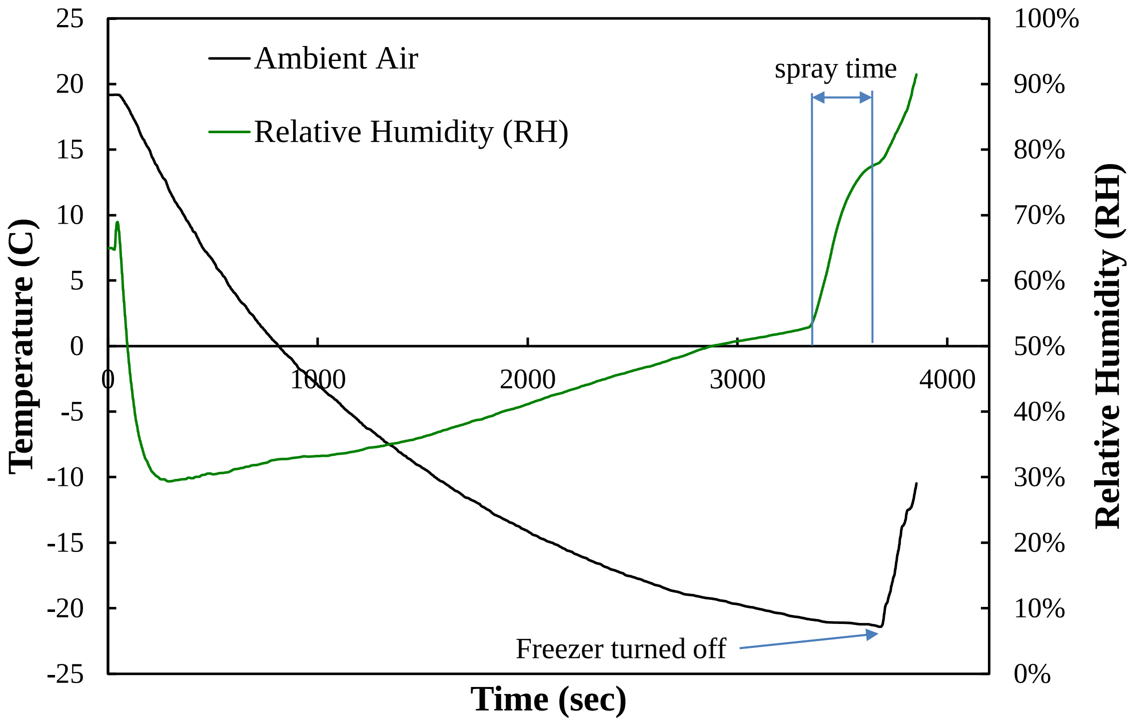
Ambient Air
Relative Humidity (RH)
spray time
Freezer turned off
Temperature (C)
Relative Humidity (RH)
Time (sec)
25
20
15
10
5
0
-5
-10
-15
-20
-25
0
1000
2000
3000
4000
100%
90%
80%
70%
60%
50%
40%
30%
20%
10%
0%

(a)

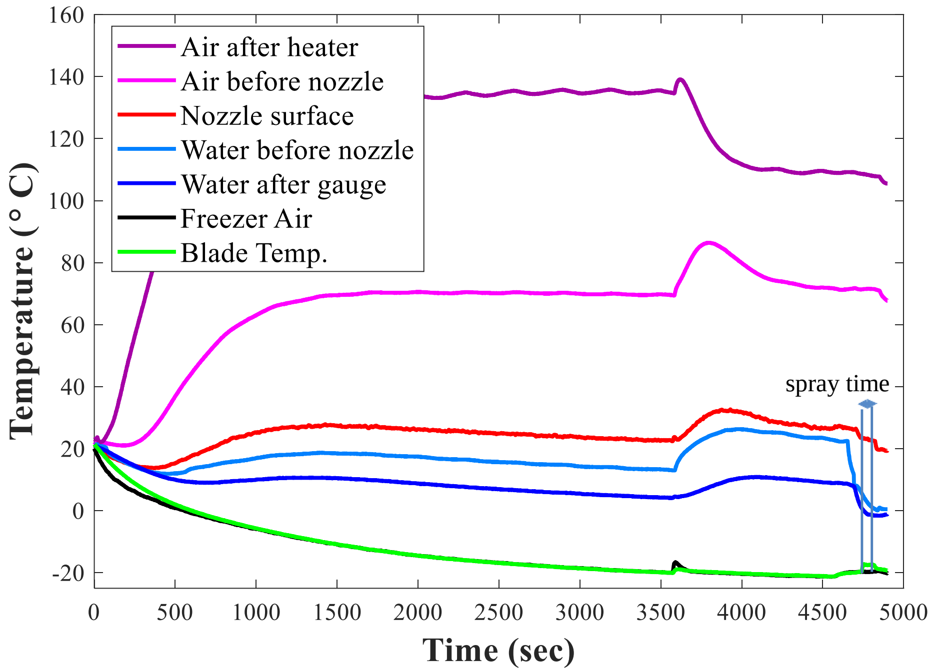
Air after heater
Air before nozzle
Nozzle surface
Water before nozzle
Water after gauge
Freezer Air
Blade Temp.
spray time
Temperature (° C)
Time (sec)
160
140
120
100
80
60
40
20
0
-20
0
500
1000
1500
2000
2500
3000
3500
4000
4500
5000

(b)

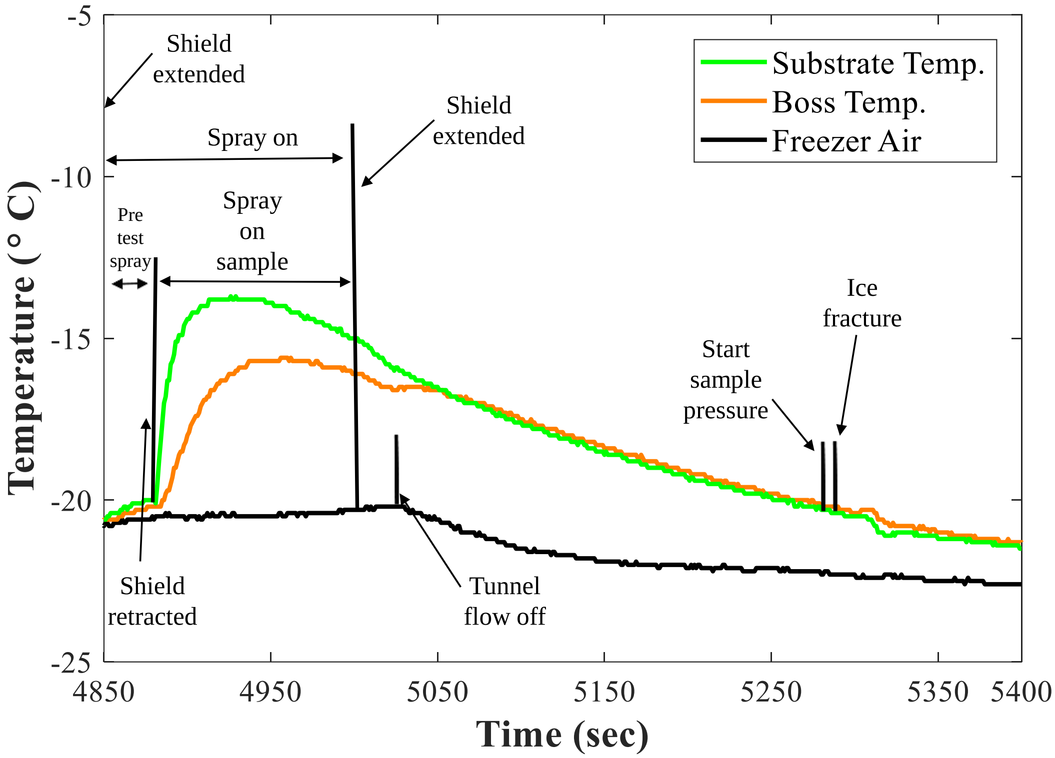

(c)

Fig. 3-12 Sample transient measurements for (a) relative humidity, (b) temperature from thermocouples during freezer cool-down and (c) temperature during spraying conditions up to ice fracture for impact ice (with tunnel flow operating). Curves' color matches thermocouples' one in Fig. 3-11.

The results indicated an average substrate temperature increase of 7°C for the impact ice tests compared to 5°C for static ice tests. Such temperature rises are deemed significant since it is known that ice adhesions can be a strong function of temperature [97,118,123–125]. Fortunately, the similarity in these temperatures for static and impact ice makes it reasonable to compare their ice adhesion properties, as done in this study. However, in the more general case where these may be very different, it may not be appropriate to make such a direct comparison. As such, it may be important to measure air and substrate temperature transients to characterize the freezing process and rejection of latent heat when evaluating difference in ice adhesion. Such temperature characterization has not been used for any impact icing tests to the authors' knowledge.

It is interesting that the present temperature rises for static and impact ice were about the same considering the time to reach the temperature rise peak was much different (about 35 seconds for impact ice and about 85 seconds for static ice). This temperature rise is associated with latent heat of rejection during freezing, where this heat can be transmitted to the substrate from the ice during phase change. For the impact ice case, it is expected that the latent heat can also be rejected into the surrounding air by convection (given the high flow speeds in the test section) as well as by droplet evaporation (though this effect is not expected to be large given the high humidity). In the static ice test case, the ice formation time is slower but one would expect that the still conditions would include very little convective heat transfer from the substrate to the air and little droplet evaporation heat rejection, such that most of the heat rejection would be into the substrate. As such, the similarity in temperature rise between static and impact icing may be attributed to counter-acting effects of more avenues of heat rejection (convection and evaporation) for the impact ice case compared to more time for heat rejection for the static ice case. However, the temperature rise for the impact icing case can also be the result of the temperature of the impacting drops that are above that of the freezer air. While Fig. 3-7 indicates that this is not probable for the drops that are 20 microns or smaller, the size distribution of Fig. 3-6 indicates that about 25% of the droplets have diameters larger than 20 microns where this effect may be present. Given the significance of the temperature, it is recommended that the thermophysics of ice accretion be further investigated to better characterize and understand this phenomenon.

3.3.2 Tensile Adhesion Test Results

Generally, following the ice removal process, one of these 3 types of ice fracture is expected to occur: a full adhesive fracture (full ice-surface interfacial failure with no ice residue left on the surface), a full cohesive fracture (full failure through the ice structure with a complete layer of ice residue left on the surface) or a mixed-mode fracture (combination of adhesive and cohesive fracture). For all the tensile tests conducted (8 from both impact and static ice), a mixed-mode fracture occurred as shown in Fig. 3-13. The static ice tests left more ice residue on the test substrate surface than impact ice tests.

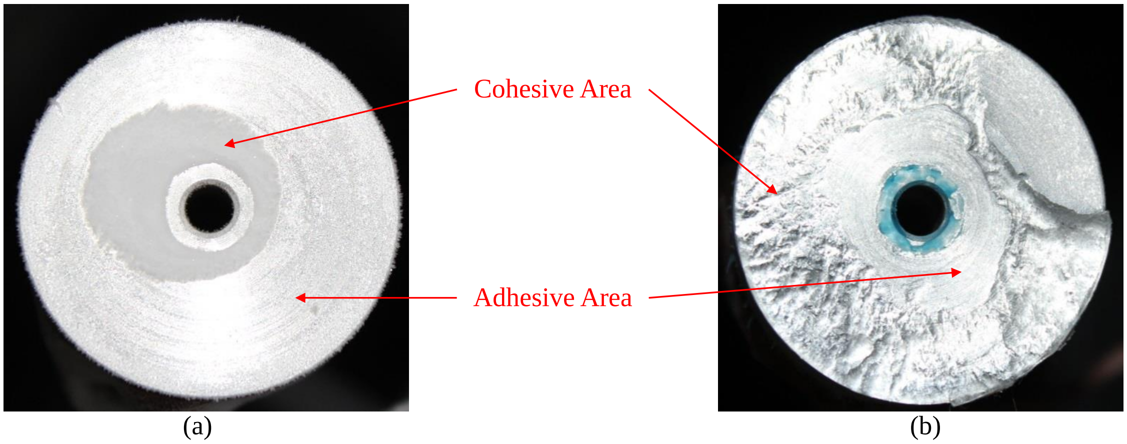

Fig. 3-13 Images showing example results of cohesive and adhesive area on aluminum sample after ice fracture in (a) impact ice test with cohesive residual ice area fraction (α) of 12% and (b) static ice test with α=60%. The cohesive area fractions for other tests are in Table 3-2.

As mentioned earlier, the boss piece was pressurized at a fairly constant rate of 131 kPa/sec until ice fracture occurs. It was noticed that the critical pressure required for ice fracture was lower and more repeatable in the cases of impact ice as compared to static ice. Using the critical air pressure values recorded during the tests, the residual ice area fraction (α) and the test geometry, the fracture energy and ice tensile adhesion stress data were computed based on a methodology described in [118–121]. The results are tabulated in Table 3-2, showing each test data set and the averages. Aluminum impact ice tests displayed a fracture energy with a mean of 0.44 J/m^2 that was 60% lower than that for the static ice tests (1.1 J/m^2). Similarly, the impact tests yielded a mean ice tensile strength value of 0.42 MPa, which was 37% lower than the static ice value (0.67 MPa). These relative differences between impact and static ice are consistent with observations by Chu *et al*. [126], though the absolute values of Chu *et al.* were somewhat higher, which is attributed to different icing conditions (temperature, velocity, etc.) and different testing procedures (ice strain rate).

It is important to comment on the variation of the present fracture measurements. Some scatter can always be expected due to the stochastic nature of the crack propagation and the brittle property of ice. For the present results, the rms relative to the mean for fracture energy was 18% for impact ice and 61% for static ice, while that for ice tensile strength was 11% for impact ice and 17% for static ice. While such scatter is significant, these values are generally lower than that for previously reported ice adhesion data [118–120,126]. For example, the experiments from Pervier [118] and Yeong [119] have revealed rms values about the mean of 30% and 26% respectively for fracture energy and tensile adhesion stress for impact ice tests conducted on aluminum and titanium at different conditions. Thus, the present approach to minimizing effects associated with frosting, surface contamination, manufacturing variations of the substrate helped limit the experimental scatter.

Table 3-2 Results of impact and static ice tests.

	Test #	Velocity (m/s)	Fracture Pressure (kPa)	Cohesive Residue (%)	FE (J/m^2)	Tensile Stress (MPa)
Impact	1	40	1451	20	0.6	0.51
	2	40	1280	10	0.49	0.46
	3	40	726	60	0.13	0.23
	4	40	1319	12	0.54	0.48
Static	1	0	1897	68	0.76	0.57
	2	0	1633	46	0.63	0.52
	3	0	3143	60	2.15	0.96
	4	0	1931	42	0.87	0.61
Impact Avg.		40	1194	26	0.44	0.42
Static Avg.		0	2151	54	1.1	0.67

3.4 Conclusions

Aerodynamic ice accretion is a problem encountered in a number of applications, leading to the creation of purpose-built icing wind tunnels for its study. This manuscript relates how a Compact Icing Research Tunnel (CIRT) was designed to allow low-cost, quick turn-around, high-quality icing tests in modest volume over a range of conditions. The CIRT, which is equipped with a single nozzle water spray system, allows icing tests at the following conditions: a temperature range of -35°C to 0°C, an airspeed up to 40 m/s, a droplet cloud MVD between 10 to 40 microns, and a LWC range of 2-4 g/m^3. In particular, there must be sufficient time of flight from nozzle injection to sample impingement to ensure a proper supercooled state for a given drop size. This icing facility's instrumentation includes thermocouples installed at various locations to monitor the temperature variation of various fluids and components during all icing tests, as well as an ice tensile adhesion measurement test process, which was developed for the CIRT.

The transient measurements indicated a sample's average temperature increase of 7°C for the impact ice tests compared to 5°C for static ice tests. Such temperature rises are deemed significant since it is known that ice adhesions can be a strong function of temperature. The consistency in temperature rise suggests that the dominant mechanism for is the latent heat of freezing. Still, it is surprising that the impact ice and static ice cases were not more different given they are two different ice formation processes. The similarity may be attributed to counter-acting effects of more avenues of heat rejection for the impact ice case (that also includes convection and evaporation), which should be further investigated, compared to more time for heat rejection for the static ice case. The similarity in these temperatures for the present static and impact ice may allow a more direct comparison of their ice adhesion properties. However, it may not be appropriate to make such a direct comparison when these temperatures are much different. As such, it is recommended that future icing tests measure air and substrate temperature to characterize the freezing process and subsequent ice adhesion.

The present results also showed a substantial reduction (about a factor of two) of mean fracture energy and mean ice adhesion strength for impact ice compared to static ice, consistent with previous studies. Additionally, the facility and method were designed to reduce ice tensile strength variation from test-to-test by minimizing effects associated with frosting, surface contamination, manufacturing variations of the substrate. In general, this approach led to an overall reduction in scatter, but the variations are still significant indicating that multiple tests are needed for a given surface (e.g. four as employed herein). Overall, the design and testing of the CIRT shows that a small-scale icing facility can produce high quality icing conditions at 40 m/s while integrating thermal and humidity characterization with tensile ice adhesion and fracture energies measurements.

Chapter:

4 Reducing Static and Impact Ice Adhesion with a Self-Lubricating Icephobic Coating (SLIC)

4.1 Introduction

Atmospheric ice accretion is a great concern for several engineering applications. Ice buildup on aircraft (wings, engine) was recognized to be a serious hazard to flight safety and aircraft operations [96]. Particularly for engines, ice accretion on various components (as shown in Fig. 4-1a) was reported to result in problems such as engine rollback, compressor stall/surge, and flameout. Tragic cases of flight crashes due to icing include the Continental Connection Flight 3407 killing all its passengers [100], the American Eagle Flight 4184 [91], and many others. Other applications that suffer heavily from icing are wind turbines. Ice accumulation on wind turbine blades, as shown in Fig. 4-1b, modifies their aerodynamic characteristics, resulting in a decrease of power production [92,100,127]. Up to a 17% loss in Annual Energy Production (AEP) and a power coefficient reduction into the range of 20%–50% were reported for wind turbines due to icing [127]. Furthermore, ice accretion on these blades and irregular shedding typically result in load imbalances and, subsequently, in an excessive turbine vibration [93].

To then prevent or mitigate icing, anti-icing/deicing systems are used. These systems range from active systems, such as electro-thermal systems, to passive systems, such as water-repellent/low adhesion coatings or surfaces. Among these anti-icing/deicing systems, passive systems are more attractive, as they do not require the use of any sort of energy. One example of passive anti-icing/deicing systems is superhydrophobic coating. These coatings, which have a high degree of water repellency, displayed a low adhesion property, thus proficient at removing/mitigating ice [6,128–139]. In addition to being icephobic, one of the main issues hindering the large-scale use of superhydrophobic surfaces is their poor mechanical stability. These superhydrophobic surfaces were revealed to be fragile to mechanical shear and usually deteriorated after several trials of the same experiment [139–144].

Subsequently, they fail to mitigate ice for long durations in practical conditions. To address this issue of durability of superhydrophobic coatings, techniques such as the introduction of hierarchical roughness structures to reduce the surface roughness features were used to enhance their robustness to mechanical shear [140–144]. In some cases, these techniques helped these surfaces gain self-healing capabilities [141,145]. However, some of these coatings may have additional issues in addition to their mechanical stability. Some studies reported some of these surfaces to perform poorly in environments that were highly humid [139,146,147], at extremely cold temperatures (−15°C and below) [148], and at conditions besides static ice conditions (i.e., motionless water frozen on a cold surface) or low droplet impact velocities, e.g., less than 10 m/s [121,149]. Additional drawbacks undermining the icephobic properties of these surfaces are described in References [5,120,131,148,150,151]. As a result, the association of icephobicity with superhydrophobic surfaces remains debatable.

Another example of passive anti-icing/deicing systems is that of lubricated micro-/nano-textured surfaces infused with hydrophobic or hydrophilic lubricants. These surfaces are widely known as slippery liquid-infused porous surfaces (SLIPS) or liquid-impregnated/infused surfaces (LIS) [5,147,152–159]. These surfaces, which generally possess a low contact angle hysteresis (difference between advancing and receding contact angles) and, in some cases, can self-heal (by capillary wicking due to the lubricating film) [153,154,157,158,160], were highly successful at delaying ice nucleation and achieving low ice adhesion, arguably much better than superhydrophobic surfaces. However, these surfaces' effectiveness may be limited by their mechanical and lubricant stability, as they often lose icephobicity once the lubricating film is depleted (either by evaporation, leak, or consumption) [155,159]. As a result, this may hinder their practical applications [91,156].

A third example of passive anti-icing/deicing systems, which are a sub-branch of SLIPS, is that of liquid-infused elastomers [159,161–166]. Since elastomers generally have a high elastic modulus and elasticity was identified as key to icephobicity [167,168], these surfaces, therefore, combine the use of a lubricant and an elastomer. These liquid-infused elastomers, which consist of an elastic matrix/elastomer in which the lubricant is infused, were revealed to be durable (having self-healing capability) and to possess formidable icephobic properties. One of those surfaces, which showed significant success under supercooled droplets at low impact speeds (less than 10 m/s) is the Self-Lubricating Icephobic Coating (SLIC). SLIC was developed and tested for aerospace applications and showed self-healing properties for these conditions [91]. This coating was found to be stable in long-term centrifugal accelerations in a rotating fan assembly. In particular, the coating applied on a fan blade at a radius of up to 25 cm was rotated at

1000 rpm for up to six hours with no delamination or loss of ice adhesion performance. It should be noted that this corresponds to a centrifugal acceleration of 2,740 m/s^2 (equivalent to 280 g's).

The goal of this study was to investigate the performance of SLIC in terms of tensile ice adhesion for both static ice and high-impact ice (at 40 m/s), and also to directly compare these results to ice adhesion on a surface of aluminum, which represents the most common conventional aerospace metal surface. A specialized Compact Icing Research Tunnel (CIRT) was developed for this study, where the impact ice condition employs a spray cloud of supercooled water droplets, with a mean volumetric diameter (MVD) of 13 microns impacting at a velocity of about 40 m/s in a wind tunnel test section. The CIRT was equipped with a wide array of diagnostics to help fully characterize testing conditions and to obtain ice adhesion tensile strength for both surfaces with a well-established pressure-removal technique. The tensile stress results were then compared to each other and to other tensile stress data available in the literature.

This is a unique study, as ice adhesion has not been previously investigated (to the authors' knowledge) for a self-healing icephobic surface at high-speed (30 m/s and up) impact ice conditions with direct comparison to an aluminum surface. This study is also unique in that it is the first to include a direct comparison of impact ice adhesion data to static ice adhesion data within the same facility. Additionally, this study is the first to compare the robustness of the coating hydrophobicity (contact angle and roll-off angle) for impact icing with that for mechanical abrasion. This abrasion included both a soft abradant (that can cause surface lubricant depletion) and hard abradant (that can cause elastomer depletion).

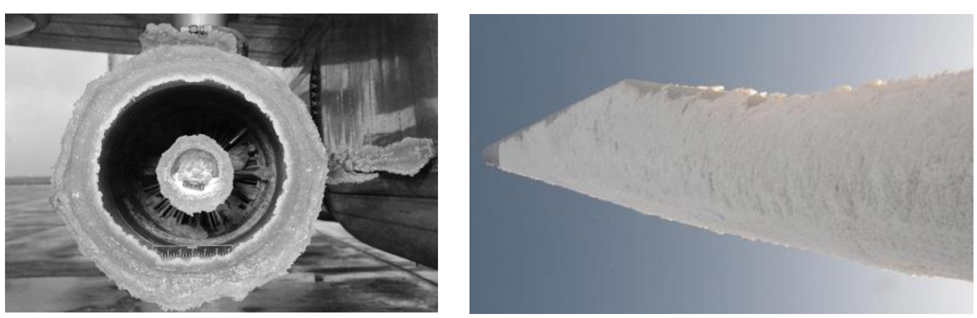

(a) (b)

Fig. 4-1 Icing on (a) the inlet of an aircraft's engine (courtesy of NASA) [11,169] and (b) a wind turbine blade [127].

4.2 Materials and Methods

4.2.1 Tested Surfaces

For this study, the surface discs to be tested included a conventional aluminum surface (non-coated) and an aluminum surface coated with SLIC. The SLIC coating is a hydrophobic oil-infused elastomer that was drop-casted on the aluminum substrate. The coating consists of an elastic matrix in which a lubricant (oil in this study) is infused. Different images of the SLIC are shown in Fig. 4-2. As depicted in Fig. 4-2a, the elastomer/elastic matrix acts as a reservoir for the lubricant, which diffuses towards the coating surface. Reference [161] described such a phenomenon where organic lubricants stored within an elastomeric matrix were observed to migrate towards the surface. This lubricant migration towards the surface creates an oil layer at the surface of the coating (shown in Fig. 4-2a–c), which enables it with a low contact angle hysteresis and smoothness (smooth and lubricated part of SLIC is shown in Fig. 4-2d by the dark/gray regions). These characteristics, in addition to the elasticity of the elastomer, are desirable attributes of an effective icephobic surface. Additionally, the constant oil secretion within the coating and diffusion to the surface enables it with a self-healing ability, which will be assessed and described in a section below. The wettability properties of the coating were quantified, as well as the ones of the aluminum, using a Rame-Hart goniometer (Rame-hart Instrument Co., Succasunna, New Jersey, USA). The contact angles were measured using a 10 µL water drop, while the roll-off angles were measured with a 20 µL water drop. Three measurements were taken on each sample using 3 different drops respectively for the contact and roll-off angles. The average values from the results ensuing from the measurements are tabulated in Table 4-1. Additionally, the uncoated aluminum substrate (used for comparison) had a roughness R_a of 4.8 µm, while the SLIC coating had a roughness R_a of 1.2 µm and was about 125 µm thick.

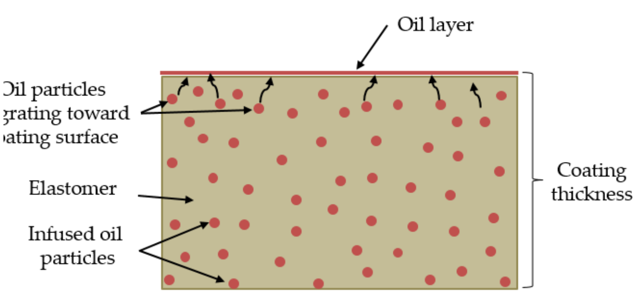

(a)

(b)

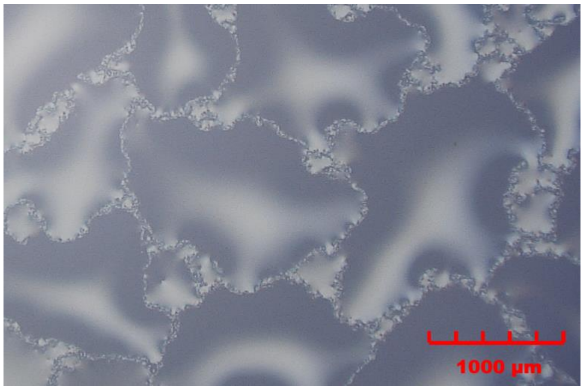

(c)

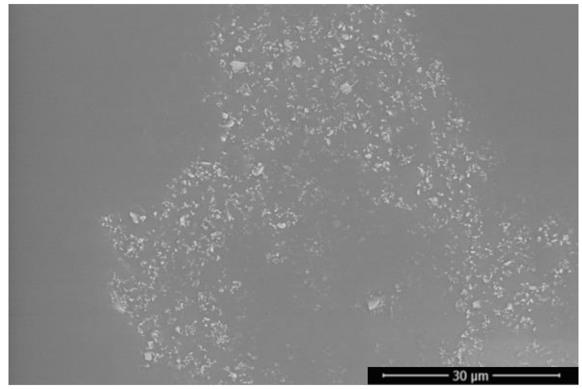

(d)

Fig. 4-2 Different images of the Self-Lubricating Icephobic Coating (SLIC) coating: (a) Schematic of the SLIC showing the diffusion of the infused oil particles [91], (b) a CANON photographic camera picture of SLIC showing the layer of oil atop the elastomer, (c) a HIROX optical microscope image of SLIC, where bubbles represent oil atop the elastomer, and (d) a scanning electron microscope image showing smooth and lubricated regions of SLIC. These smooth regions are without grains.

Table 4-1 Wettability properties (contact and roll-off angles) of both aluminum and SLIC surfaces.

Wettability Properties	Aluminum	SLIC
Contact Angle (deg.)	82.4	99
Roll-off Angle (deg.)	27	13

4.2.2 Ice Tensile Facility

The tensile ice adhesion experiments were performed in a compact icing research tunnel (CIRT) located at the University of Virginia, USA. The CIRT has a test section of 7.5 (3”) by 10 cm (4”) and allows icing tests for both static and impact (up to 40 m/s air velocity) conditions [170]. The CIRT was equipped with diagnostics to characterize test conditions and obtain ice tensile adhesion strength on the test specimens. The overall experimental setup is shown in Fig. 4-3a, where the test specimen consisted of a vertical aluminum boss piece (cylinder) coupled to a 30 mm diameter substrate disc.

As shown in Fig. 4-3b, the static ice was obtained by pouring deionized water into a cylindrical mold formed above the test specimen and allowed to freeze over time at an ambient air temperature of –20 °C. The impact ice, on the other hand, was created by spraying an icing droplet cloud with a size of 13 µm and a liquid water content (LWC) of 2.8 g/m^3 0.9 m upstream of the test specimen, as shown in Fig. 4-3a,c. These droplets then impacted the test specimen in the test section at a velocity of 40 m/s, freezing in the process. For both impact and static ice, deionized water was used, as impurities in the water can potentially result in a larger variation in ice adhesion strength [119,120].

At the center of the test fixture was a 4 mm diameter hole, which was covered by a thin (50 µm thick) Teflon (PTFE) disc, which was 7 mm in diameter. The purpose of this Teflon disc was to create a sealed surface during both impact and static ice accretion. No recess was needed in the substrate disc for the Teflon disc, as the Teflon disc was maintained firmly on the disc by creating a suction force that was carefully calibrated and controlled by a needle valve attached to a vacuum pump, as shown in Fig. 4-3a. Once ice (impact or static) was established on the substrate disc, pressure from a gas (clean and filtered air from a pressurized air bottle) was applied underneath the Teflon defect via the 4 mm channel to remove most or all of the ice from the substrate in tensile mode. This pressure was initialized at atmospheric conditions and then slowly and continuously increased at a constant rate of 131 kPa/s until ice fracture occurred from the test substrate, a pressure that was labeled as the fracture pressure. This method of ice adhesion measurement on a surface was initially designed and implemented by Andrews and Lockington [115–117], and was adapted to enable in situ testing in an icing wind tunnel for both impact and static ice conditions. More details on this procedure are discussed in the following section.

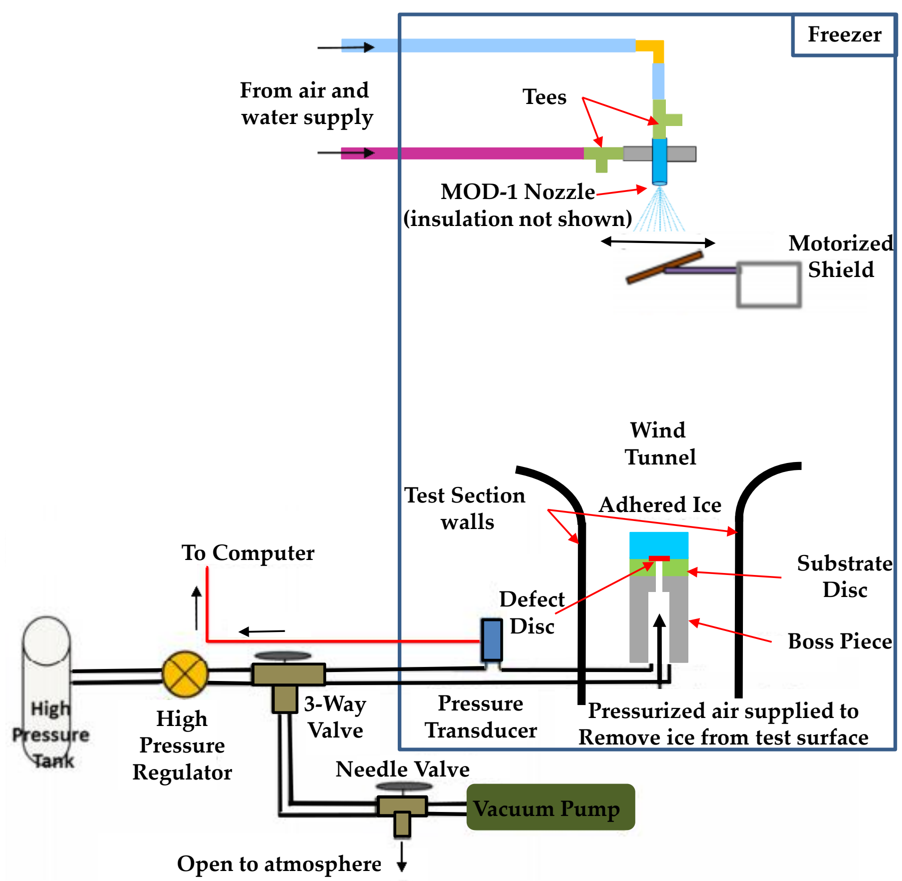

(a)

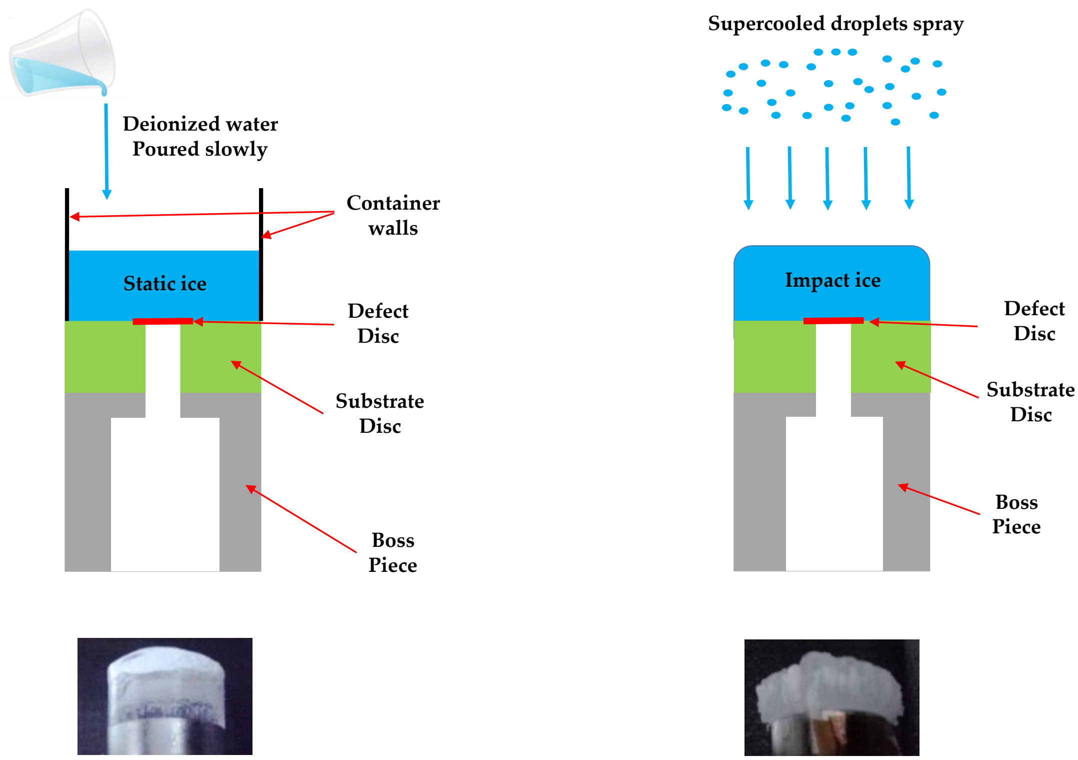

(b) (c)

Fig. 4-3 For ice tensile measurements (not to scale): (a) Overall setup in the compact icing wind tunnel, (b) zoom-in of the static ice accretion procedure, and (c) zoom-in of the impact ice accretion procedure.

4.2.3 Ice Tensile Test Procedures

Prior to each aluminum surface icing test, the substrate disc was cleaned by wiping its surface first with a dry Chem-wipe and then with a Chem-wipe soaked in 95% isopropyl alcohol. A single physical aluminum test substrate was used for all impact and static ice tests. This was to reduce variation in test results that could be attributed to differences in substrate disc characteristics. Similarly, one SLIC test substrate was respectively used for all impact ice tests and one for all static ice tests in order to investigate surface resilience to icing conditions. To prevent any contamination (dirt, dust) on the SLIC surface between icing tests or after, the test substrates were preserved in an enclosed box and were only taken out for icing tests.

Once the aluminum and SLIC test substrate surfaces were ready, they were attached to the boss piece, and the assembly (boss piece and substrate disc) was mounted onto the air pressure pipe in the icing tunnel test section (as shown in Fig. 4-3a). In the case of the static ice tests, a small amount of high-viscosity grease was utilized in addition to the suction force to secure the Teflon disc over the 4 mm access hole of the substrate disc. The high-viscosity grease was added to prevent water from leaking underneath the Teflon disc into the pressurization channel and then freezing over time. This grease was carefully applied to ensure that there was no contamination to the rest of the substrate disc surface. After mounting the test sample in the tunnel test section, the icing wind tunnel ambient air was then set to reach a temperature of −25 °C. The reason for setting the target temperature lower than the intended testing temperature (−20 °C) was to prevent the cooling system of the icing wind tunnel from switching off once the targeted temperature was reached. For both impact and static ice tests, the test substrate was left to cool down to the temperature of −20 °C before ice fracture initiation to reduce variation in test results. The ice fracture procedure for both impact and static ice tensile tests was consistent with that previously established [170]. GoPro recordings of the impact ice accretion, as well as of the tensile test/pop-off test on both the aluminum and SLIC surfaces, are provided in Appendix A.

A time sequence of all of the steps for the impact ice tensile test is depicted in Fig. 4-4a. First, the icing wind tunnel ambient air was cooled down to freezing temperatures. Filtered air, which was then heated by an air heater installed in the line, was supplied to the spray nozzle to prevent the temperature from falling below freezing [170]. At an ambient air temperature of −20 °C, the tunnel fan was switched on and its speed was regulated to create an airflow of 40 m/s in the tunnel test section. Following this step, heated air and water were supplied to the spray nozzle at set pressures to produce a droplet cloud of 13 μm with an LWC of 2.8 g/m^3, and a pre-test spray commenced once the icing wind tunnel ambient air temperature reached −21 °C. The pre-test spray was a 45 s process, where a shield (shown in Fig. 4-3a) was extended to prevent the pre-test spray droplets from impacting the test specimen. Right after the pre-test spray, the shield was retracted, and ice accretion began on the test substrate for 120 s to produce an optimal ice height of 10–14 mm. It is crucial to obtain the optimal ice height before the initiation of the tensile test; Reference [118] proved that ice with a height of greater than 10 mm has little to no influence on ice adhesion measurement. Once the needed ice height was obtained, the shield was then extended back to its initial position, and the spray and the tunnel fan were turned off. The test sample (boss piece and substrate disc) was then left to cool down to −20 °C, as it typically experienced a temperature rise during the spray due to the latent heat rejection associated with the droplets' phase change being absorbed by the test sample. When the sample's temperature reached −20 °C, the tensile test was conducted; this consisted of turning the suction pump off and increasingly supplying air to the substrate disc via the 4 mm port hole at the rate of 131 kPa/sec until most or all of the ice detached from the surface. After the ice fracture occurred, the air pressure was lowered back to zero kPa. This test procedure was repeated 5 times for impact ice tests on both the aluminum and SLIC test substrates.

A time sequence depicting the static ice test steps is shown in Fig. 4-4b. For static ice tests, a cylindrical mold was made to create a cylindrical ice block on the substrate discs to be tested. This mold was achieved by wrapping duct tape around the test sample. The purpose of the mold was to contain and hold water above the substrate disc surface while it slowly freezes. Once the cylindrical mold was formed around the test sample, it was then mounted onto the pressure pipe in the tunnel test section. At the tunnel ambient air temperature of −7 °C, deionized water (at room temperature of 22 °C) was slowly poured into the mold and left to slowly freeze as the tunnel ambient air continued to decrease slowly. Following this step, the cylindrical mold was removed once the tunnel ambient air temperature reached −18 °C, a temperature where the water in the mold was assumed to be sufficiently frozen. The test sample temperature was then reduced to −20 °C, which after the tensile test was conducted following the same steps as for the impact test. Similarly, this test procedure was repeated 5 times for static ice tests on both the aluminum and SLIC test substrates.

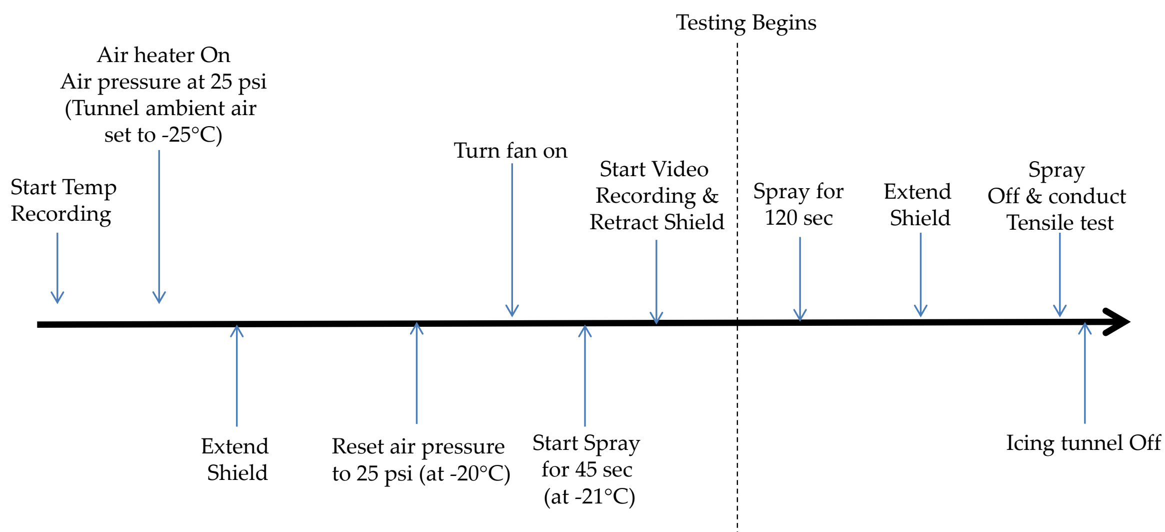

(a)

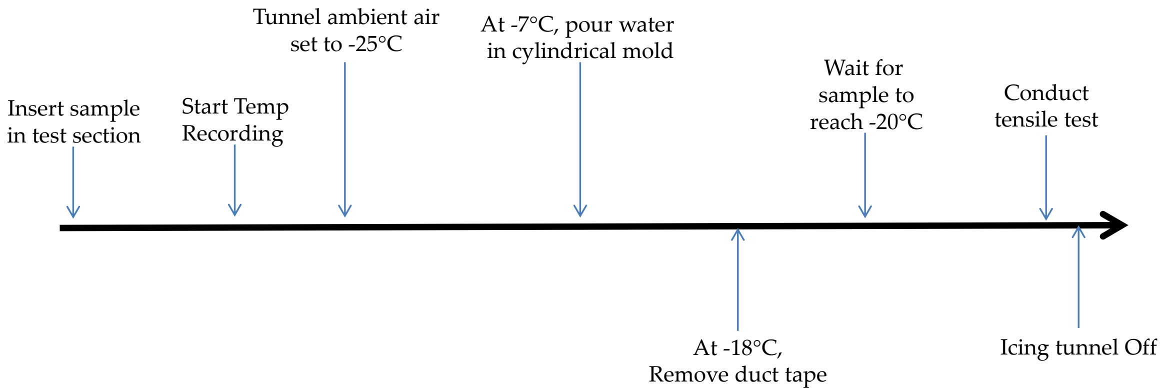

(b)

Fig. 4-4 Sequences illustrating the test procedures for (a) impact ice and (b) static ice.

4.3 Results and Discussion

4.3.1 Tensile Adhesion Test Results

As the gas pressure is applied and fracture occurs, the degree of ice detachment from the substrate can have three possible outcomes:

- A full cohesive fracture (leaving a complete layer of ice residue on the surface),
- a full adhesive fracture (leaving no ice residue on the surface), or
- a mixed-mode fracture (leaving ice residue on only part of the surface).

For all of the tensile tests (both impact and static) conducted on the (non-coated) aluminum test substrate, a mixed-mode fracture was observed. For example, Fig. 4-5 shows sample ice residues on the aluminum test substrate for both impact and static ice tests. However, the opposite happened in the case of the SLIC test substrate surface, where a full adhesive fracture occurred for all of the tests conducted, as shown by the sample test results in Fig. 4-6. This outcome on the SLIC surface is a favorable demonstration of the properties of the SLIC coating, since a desired characteristic of an icephobic coating is its ability to facilitate the removal of ice. The average residual ice area for the present tests is given in Table 4-2, which quantifies the difference between adhesive and mixed-mode fractures.

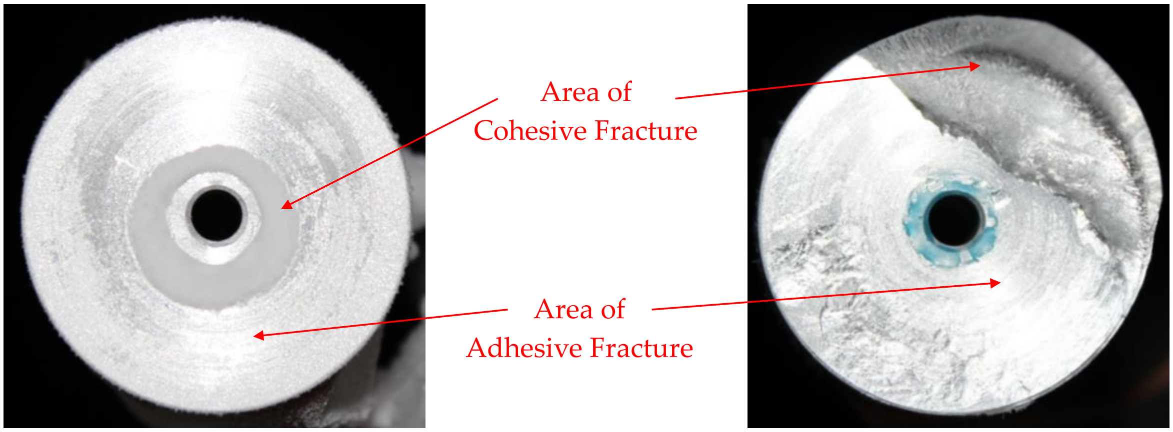

(a) (b)

Fig. 4-5 Residues left on the aluminum sample after ice tensile tests, shown by areas of adhesive and cohesive fractures for both conditions: (a) Impact ice and (b) static ice.

(a) (b)

Fig. 4-6 Full ice removal (100% adhesive failure) from the SLIC coating after ice tensile tests for: (a) Impact ice and (b) static ice.

Table 4-2 Percentage of the cohesive ice residue area fraction recorded on aluminum and SLIC surfaces for both impact and static conditions.

Surfaces	Avg. % Cohesive Residue Area Fraction	
	Impact	**Static**
Al. Surface	20	44
SLIC Surface	0	0

In addition to the amount of ice remaining on the surface, there were also differences in how the ice was released once the fracture occurred. For the aluminum test substrate, the applied pressure launched the detached ice into the air as a projectile (see Video 2 in Appendix A). For the SLIC surface, the detached ice separated from the coating but remained suspended above the coating on an air cushion. In fact, the ice would then spin while suspended above the coating, indicating that the ice was indeed fully detached (see Video 4 in Appendix A). This levitation is due to the fact that the small amount of gas pressure being applied right after the ice detaches from the SLIC surface (still not enough to push the ice block off the surface) raises this one above the surface. Subsequently, as the gas pressure was increased, the detached ice eventually left the SLIC surface (see Video 4 in Appendix A).

The pressure at which the fracture occurred was also quite different for the different surfaces and conditions. For both the non-coated aluminum and the SLIC surfaces, the impact ice fracture pressure was consistently lower (and more repeatable) than that for the static ice tests. In addition, the critical air pressure for the SLIC surface was noted to be much lower (i.e., 50%–80% less) than that for the aluminum surface. This observation confirmed the favorable attribute of the SLIC surface as having lower adhesion strength, which consequently could be used as an excellent de-icing tool in applications operating at extremely cold temperatures and where minimal force is needed for ice removal (e.g., gas turbine fan blades [91]). Using the critical pressure values, the residual ice area fraction (α, i.e., the fraction of the substrate disc area with residual ice after fracture), and the test geometry, ice tensile adhesion stress (σ_{te}) based on previously established methodology [118–121,170] was derived. At first, the fracture energy (FE) was computed using Equations (1)–(5), where 2γ and ω are the cohesive and adhesive ice fracture energies, respectively. In the equations, f_1 and f_2 are constants, ν is the Poisson's ratio for ice (taken as 0.35), c is the radius of the Teflon defect, H is the height of ice accretion, E is the Young's modulus of ice (taken as 8.5 GNm^{-2}), and P_c is the critical air pressure required for ice fracture. Once the FE was obtained, the ice tensile stress (σ_{te}) was determined using Equations (6) and (7), where K_{Ic} is the fracture toughness.

$$\mathrm{FE} = (2\gamma \times \alpha) + (1-\alpha)\omega \tag{1}$$

$$2\gamma = \frac{P_c^2 \cdot c}{E \cdot f_1} \tag{2}$$

$$\omega = \frac{(P_c^2 \cdot c)}{E \cdot f_2} \tag{3}$$

$$f_1 = \frac{1}{1-\nu^2}\left\{\frac{3}{32}\left[(\frac{c}{H})^3 + (\frac{c}{H})\cdot\frac{4}{1-\nu}\right] + \frac{1}{\pi}\right\}^{-1} \tag{4}$$

$$f_2 = \frac{1}{1-\nu^2}\left\{\frac{3}{32}\left[(\frac{c}{H})^3 + (\frac{c}{H})\cdot\frac{4}{1-\nu}\right] + \frac{2}{\pi}\right\}^{-1} \tag{5}$$

$$\sigma_{te} = \frac{K_{Ic}}{\sqrt{\pi \cdot (2c)}} \tag{6}$$

$$K_{Ic} = \sqrt{\frac{FE \times E}{1 - \nu^2}} \tag{7}$$

The individual tensile stress results for both the aluminum and SLIC surfaces are shown in Fig. 4-7, where it can be seen that the adhesion was lower for impact tests compared to static tests, and much lower for SLIC compared to aluminum. This is consistent with the trends in fracture pressure.

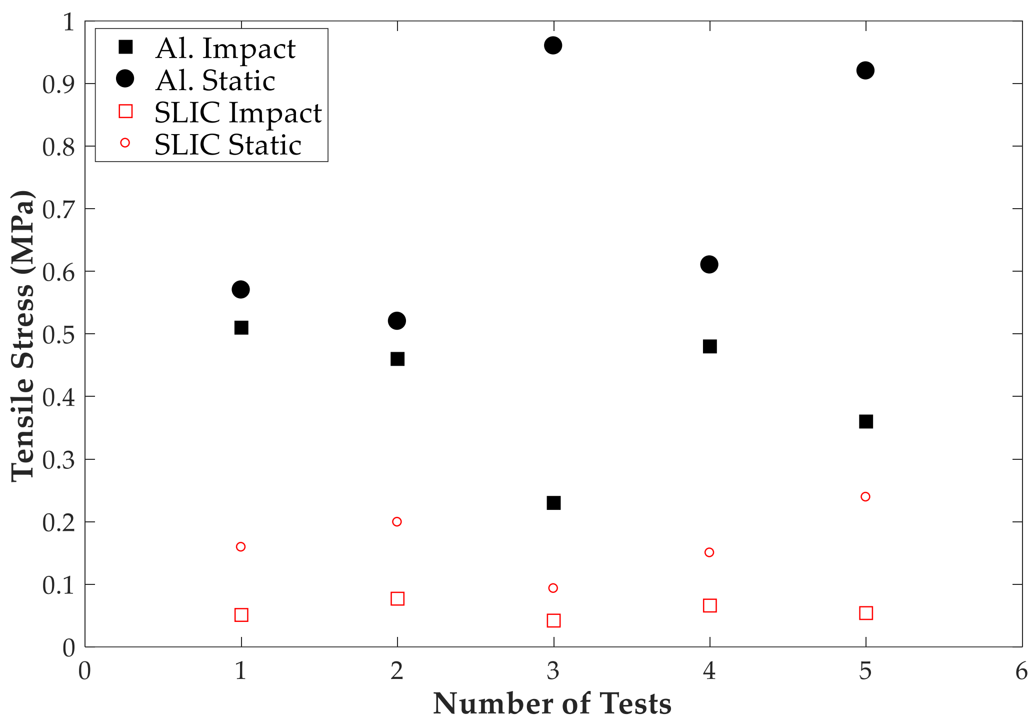

Fig. 4-7 Ice adhesion tensile stress on aluminum and SLIC surfaces for impact and static ice conditions.

Based on the results in Fig. 4-7, the ice tensile stress data were averaged. For the aluminum surface, the average ice tensile stress was found to be 0.41 MPa for the impact tests compared to 0.72 MPa for the static tests. For the SLIC surface, the average ice tensile stress was found to be 0.06 MPa for the impact tests compared to 0.17 MPa for the static tests. As a result, there was a reduction of 85% for SLIC as compared to aluminum for the impact tests and a reduction of 76% for the static tests. Overall, the SLIC surface displayed a reduction of more than half in terms of ice tensile adhesion stress compared to the aluminum surface, thus quantifying the favorable properties of the coating. This ice adhesion reduction in the case of the SLIC surface can be attributed to the low contact angle hysteresis or roll-off angle associated with the coating. In fact, several studies reported that icephobicity is highly dependent on roll-off angles [5,147,155,158,159,162,165,166,168,171]. Subsequently, the SLIC surface, with a much smaller roll-off angle (13° for SLIC compared to 27° for aluminum) displayed a low ice adhesion strength. Additionally, the lubricant layer at the coating surface coupled with the elastomer's high elasticity enable it with an interfacial slippage that enhances the release of the accreted ice release. This interfacial slippage is typical of icephobic-oil-infused elastomer coating [91,168]. Furthermore, it is to be noted that no significant degradation of this property was found, even after five tests on the same surface. This indicates surface resilience to icing conditions.

Another important aspect of the results in Fig. 4-7 is that the adhesion strength was more consistent (displayed less scatter) for the SLIC surface as compared to the aluminum surface. This is attributed to the more stochastic nature of internal ice fracture associated with mixed-mode cohesive failure for detachment from aluminum surfaces [118–120,126]. A comparison of the present ice tensile adhesion data with that reported in the literature for hydrophobic/superhydrophobic coatings and metals in tensile mode is depicted in Fig. 4-8. While the surface chemistry dominated the influence on ice adhesion, the variations are also associated with different icing conditions (temperature, air velocity, etc.), test procedures, and surface roughnesses (height and wavelength). However, the results show that static ice generally has a higher ice tensile adhesion strength compared to impact ice. Furthermore, the SLIC surface remains the best-performing surface (lowest tensile stress) among all of the results.

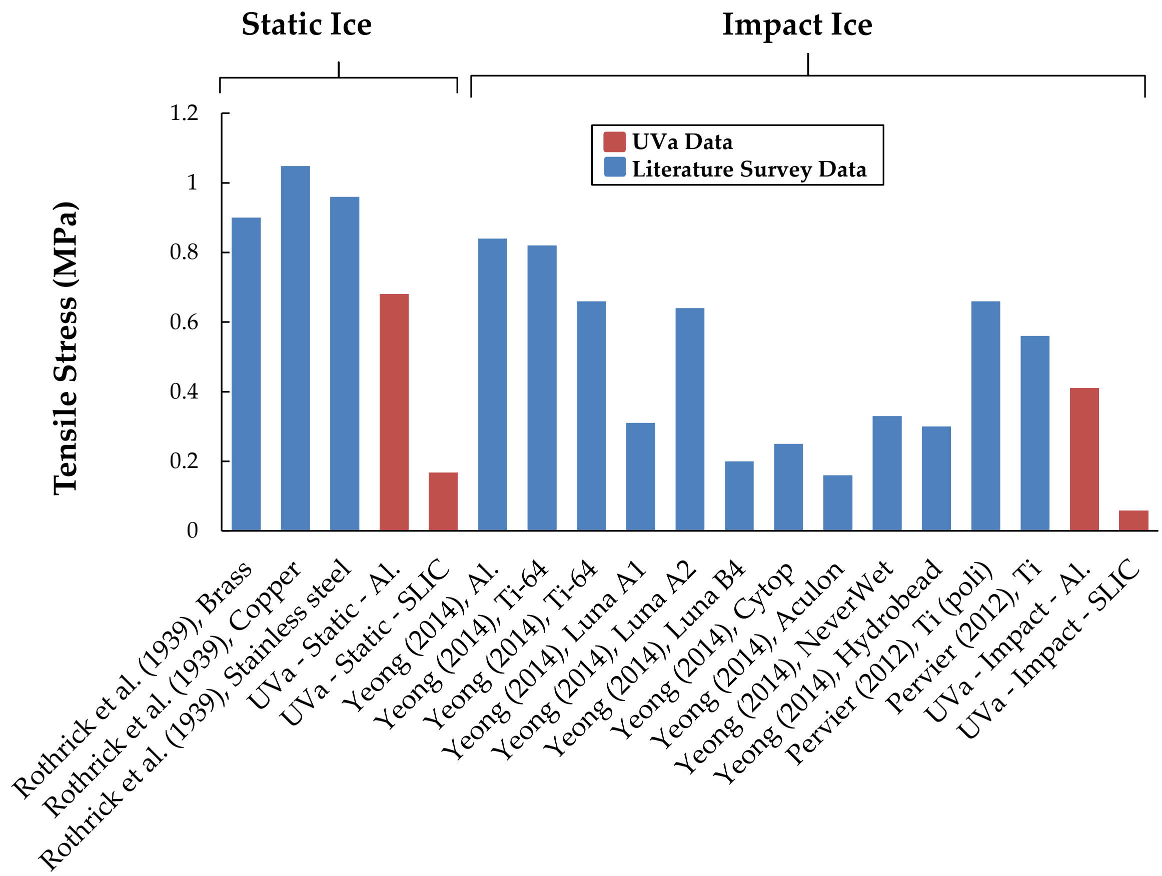

Fig. 4-8 Tensile adhesion stress value comparison of this study (red bars) with previous data (blue bars) reported in the literature [118,119,172]. The results show that SLIC has far lower adhesion stress than any reported measurement on metal surfaces or hydrophobic/superhydrophobic coatings.

4.3.2 Durability of Wetting Properties

To further investigate the resilience of the SLIC coating to icing, wettability measurements were conducted on a regular flat aluminum surface coated with SLIC (used as a baseline) and on the two SLIC substrate discs used for the impact and static icing tests (where each was subjected to five icing tests). The results shown in Fig. 4-9a,b and Table 4-3 revealed a slight enhancement of the coating's hydrophobic properties. In particular, the roll-off angles after the icing tests were actually somewhat lower, indicating that icing may help oil migrate to the surface to improve its icephobic performance. This evaluation confirms the durability of the SLIC's icephobicity with respect to icing in aerospace-based conditions.

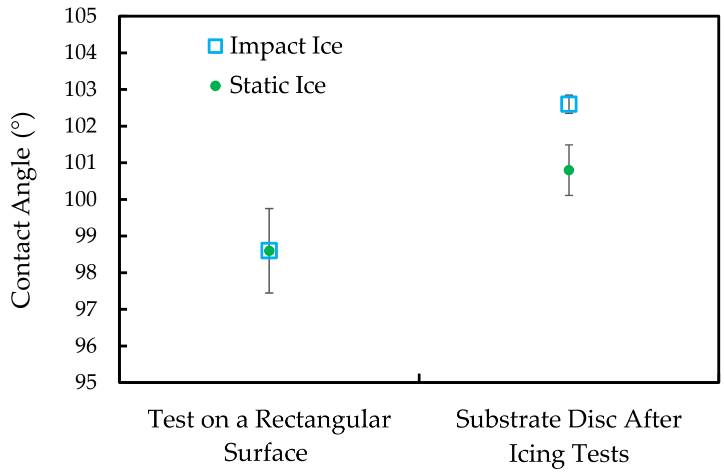

(a)

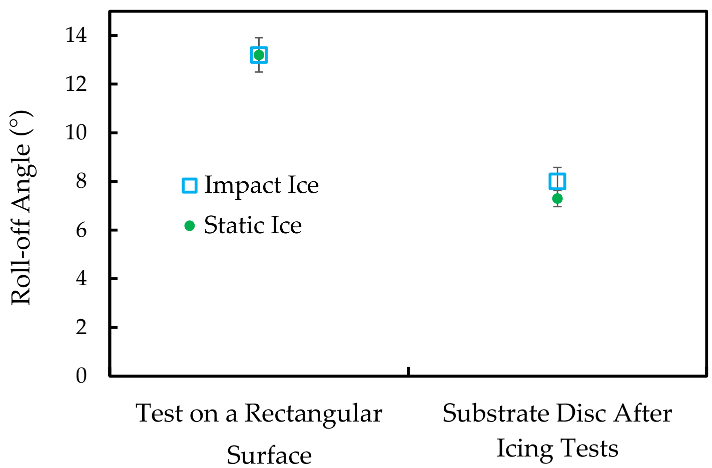

(b)

Fig. 4-9 Measurements of the SLIC's wettability properties on a flat surface and on the tested SLIC test substrate after icing tests for both impact and static ice conditions, showing in (a) the contact angle and in (b) the roll-off angle.

Table 4-3 Measurement data plotted in Fig. 4-9.

	Impact Ice		**Static Ice**	
	Contact Angle (°)	**Roll-off Angle (°)**	**Contact Angle (°)**	**Roll-off Angle (°)**
Test on a Rectangular Coupon	99	13	99	13
Substrate Disc After Icing Tests (SLIC)	102	8	101	7

4.3.3 Investigation of Mechanical Durability

While the SLIC maintained excellent durability for icing conditions, a more extreme test was to subject this coating to mechanical durability testing. This is important because a major concern of most icephobic coatings used to mitigate icing is their durability. In order to assess if this was an issue for the present hydrophobic SLIC surface, linear abrasion testing, a widely accepted method for qualitatively assessing non-wettable surfaces' mechanical durabilities, was conducted using a well-accepted abrasion technique [91,173]. This abrasion test consisted of a mechanical arm with an abrading tip which allows the installation of different types of abradants, as shown in Fig. 4-10. The mechanical arm, along with its tip, could move in a linear motion upon contact with the surface to be abraded and could be loaded with some weights to increase the force of abrasion. For this particular study, two types of abradants (medium-coarse abradant and crocking cloth) were used for the abrading tip, with a weight load of 373 g. Both mechanisms resulted in localized heating due to friction. In addition, the crocking cloth resulted in smoothing and some oil absorption of the SLIC coating, while the medium-coarse abradant resulted in micro-fracturing of the coating, since it contained abrasive particles similar to sandpaper particles.

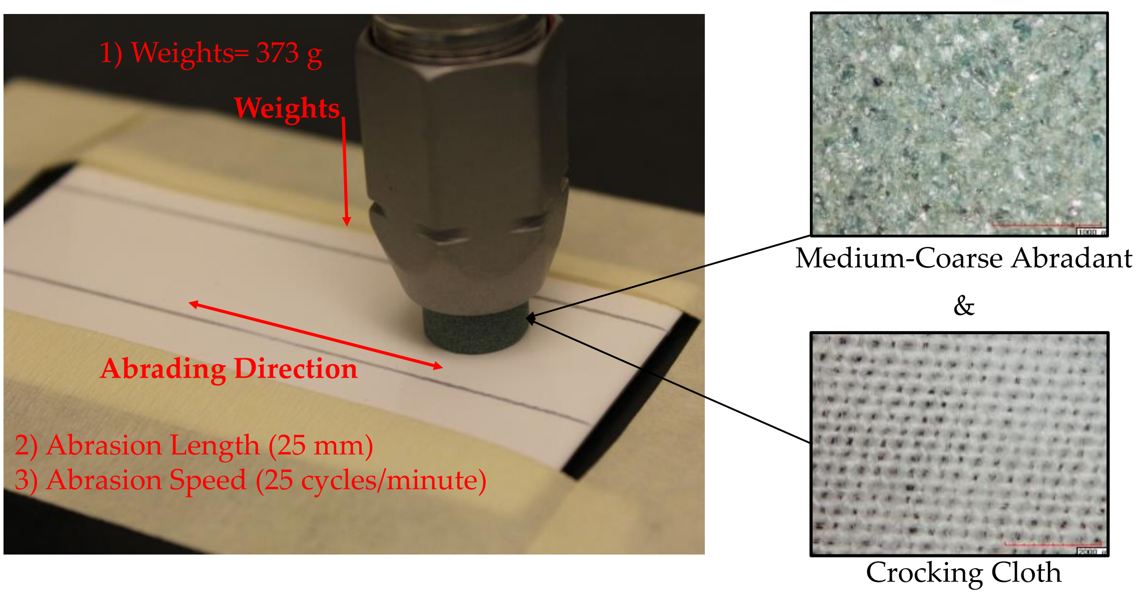

Fig. 4-10 Durability testing on a rectangular surface with linear abrasion on a SLIC surface; the right-hand-side images show two types of abradants: A medium-coarse abradant and a crocking cloth [91].

Once the SLIC coating was secured underneath the abrading tip, the mechanical arm was actuated to operate 20 cycles, where one cycle corresponds to the abrading tip going the 25 mm abrasion length on the coating in one direction and back. A video of this mechanical abrasion test, as well as the post-abrasion images of the SLIC, are provided in Appendix A. After all of the linear abrasion cycles were completed for either the crocking cloth or the medium-coarse abradant, wettability was measured in terms of static contact angle and roll-off angle. As seen in Fig. 4-11 and Table 4-4, the roll-off angle substantially increased (the performance degraded) for both abradant types, whereas the contact angle did not vary as much (the SLIC surfaces remained hydrophobic). However, four days after the abrasion test, the measurement of the wettability properties was repeated on the same samples (one each, abraded by the crocking cloth and the medium-coarse abradant). This time, the measurement revealed that the roll-off angles for both samples recovered to their original (before abrasion) value, while the hydrophobic contact angle was preserved. This demonstrates the self-healing ability of the coating; hence, the term "self-lubricating" used for the name of the coating. This self-healing ability is attributed to the high flexibility of the polymeric chain of the elastomer, enabling the oil particles in the matrix to migrate within this one and towards the surface. This behavior of polymers (or polymer-based coating) of allowing the migration of an introduced self-healing agent (oil in this study) is very typical, and is also described in other researches [167,174,175]. Notably, in Reference [167], the self-healing agent enables the coating to recover its texture, while the oil in the SLIC (self-healing agent in the coating described in this study) helps recover the coating wettability properties and functionality. Overall, this assessment shows the ability of the coating to withstand light and gradual damage that may be caused to the coating in a realistic environment. As a future study, it is recommended that ice adhesion after abrasion be measured to further investigate the durability of the SLIC.

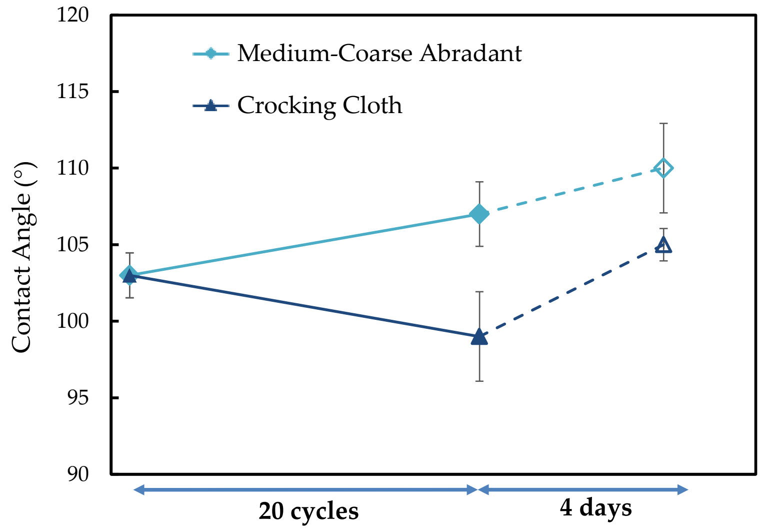

(a)

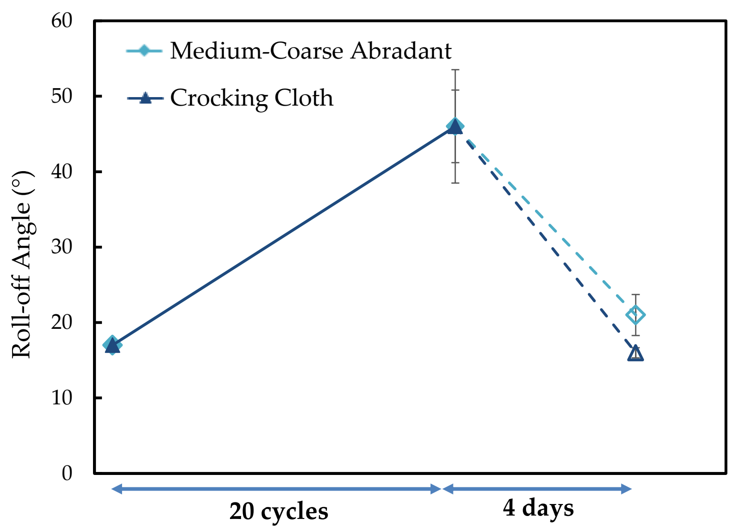

(b)

Fig. 4-11 Present measurements of SLIC wettability before and after abrasion with a medium-coarse abradant and a crocking cloth, showing in (a) the contact angle and in (b) the roll-off angle.

Table 4-4 Measurement data plotted in Fig. 4-11.

Abradants	**Contact Angle (°)**			**Roll-off Angle (°)**		
	Zero cycle	**After 20 cycles**	**After 4 days**	**Zero cycle**	**After 20 cycles**	**After 4 days**
Medium-Coarse Abradant	103	107	110	17	46	21
Crocking Cloth	103	99	105	17	46	16

4.4 Conclusions

In this study, an icing wind tunnel was used to measure ice adhesion tensile strength on a self-lubricating icephobic coating (SLIC) surface and aluminum surface for both impact and static ice conditions. The static ice consisted of deionized water contained in a cylindrical mold left to freeze over time on the tested surfaces at a temperature of −20 °C. On the other hand, the impact ice was ice formed from 13 μm droplets hitting the tested surfaces at a velocity of 40 m/s and at a temperature of −20 °C, freezing during the process. The results showed that generally, impact ice has a tensile adhesion strength lower than that of static ice. Additionally, the SLIC surface reduced the ice tensile adhesion strength by more than 50% for both impact and static ice conditions. Subsequently, this functionality makes the SLIC surface a good candidate as a de-icing tool for applications where minimal force would be required for ice removal. Additionally, the SLIC surface showed good resilience during the icing tests. In particular, even after five icing tests, the tensile stress did not significantly increase (ice adhesion did not degrade) and the roll-off angle did not significantly increase (wettability did not degrade). This resilience of the coating's hydrophobicity (contact angle and roll-off angle) was demonstrated for both impact and static icing tests. To examine the coating's robustness to mechanical abrasion, tests were conducted with a linear abrader. After the application of 20 cycles, the tests revealed some degradation of the contact and roll-off angles taken for the SLIC coating. However, a full recovery of these properties was noted when measurements were taken four days after the abrasion testing. This indicates a self-healing ability associated with the SLIC for these conditions.

Chapter:

5 Ice Shear Adhesion for Different Surfaces and Flow Conditions

5.1 Introduction

Ice accumulation is a significant problem that damages structures like power lines, communication towers, wind turbines, and aircraft [11,41,98–102,127,176–179,90–97]. For aircraft, ice accretion was found to have detrimental consequences, including engine power losses, damage to control-surface hinge movements, increased drag, decreased lift, and even fatal crashes [33,91,100,180,181]. Furthermore, icing can lead to malfunctioning for transmission lines used with communication towers, a decrease of heat transfer efficiency for power lines, and decrease of power production for wind turbines. As such, understanding ice accretion and adhesion is essential to develop tools to facilitate the removal of ice or retard its formation. To that end, several techniques have been developed to measure ice adhesion on metal surfaces and icephobic coatings, which can exhibit a low ice adhesion. Ice adhesion is the bond that forms at the ice/substrate interface and prevents ice removal from the substrate's surface. This ice removal can occur in either a perpendicular direction (tensile mode) or parallel direction (shear mode). Often, atmospheric accreted ice tends to be removed from the surface in the shear mode rather than tensile (e.g., ice removed from aircraft wing due to drag/wind shear, or ice removed from spinning blades due to centrifugal forces). This ice adheres to the surface until the force required to break the adhesion bond is met. The ice adhesion is generally the strongest at temperatures of -15°C and below, for which rime ice (vs. glaze ice) is typical.

To quantify the shear ice adhesion, a wide variety of measurement techniques have been developed for impact ice (i.e., ice formed from droplets moving at ~ 5 m/s or higher on a cold surface) or static ice (i.e., formed from motionless water frozen on a cold surface). The primary techniques employed for measuring this adhesion are illustrated by the schematics in Fig. 5-1 and the shear techniques include: (a) ice push, (b) ice centrifuge, (c) substrate pile push, and (d) substrate pile pull. Key aspect of these techniques are summarized in Table 5-1, Table 5-2 & Table 5-3. Table 5-1 summarizes previous studies using driving push (the most common technique) while Table 5-2 summarizes studies using centrifugal spin (second most common technique) and Table 5-3 lists the other techniques. Each table orders the studies by the type of ice used (static vs. impact), and within each case chronologically (from oldest to most recent). Ice adhesion strength is defined as the stress at which ice fracture occurs between the ice and the substrate. Often, the fracture stress is reported but it should be kept in mind that this only formally corresponds to ice adhesion strength if the ice is completely removed from the substrate (notably the area fraction of ice removal was not always recorded). Furthermore, none of the studies in Table 5-1, Table 5-2 & Table 5-3 measured temperature transients on the substrate during ice formation/accretion, even though these temperature rises can be significant [100]. As a result, columns were not included for thermal transient characterization nor area fraction residue.

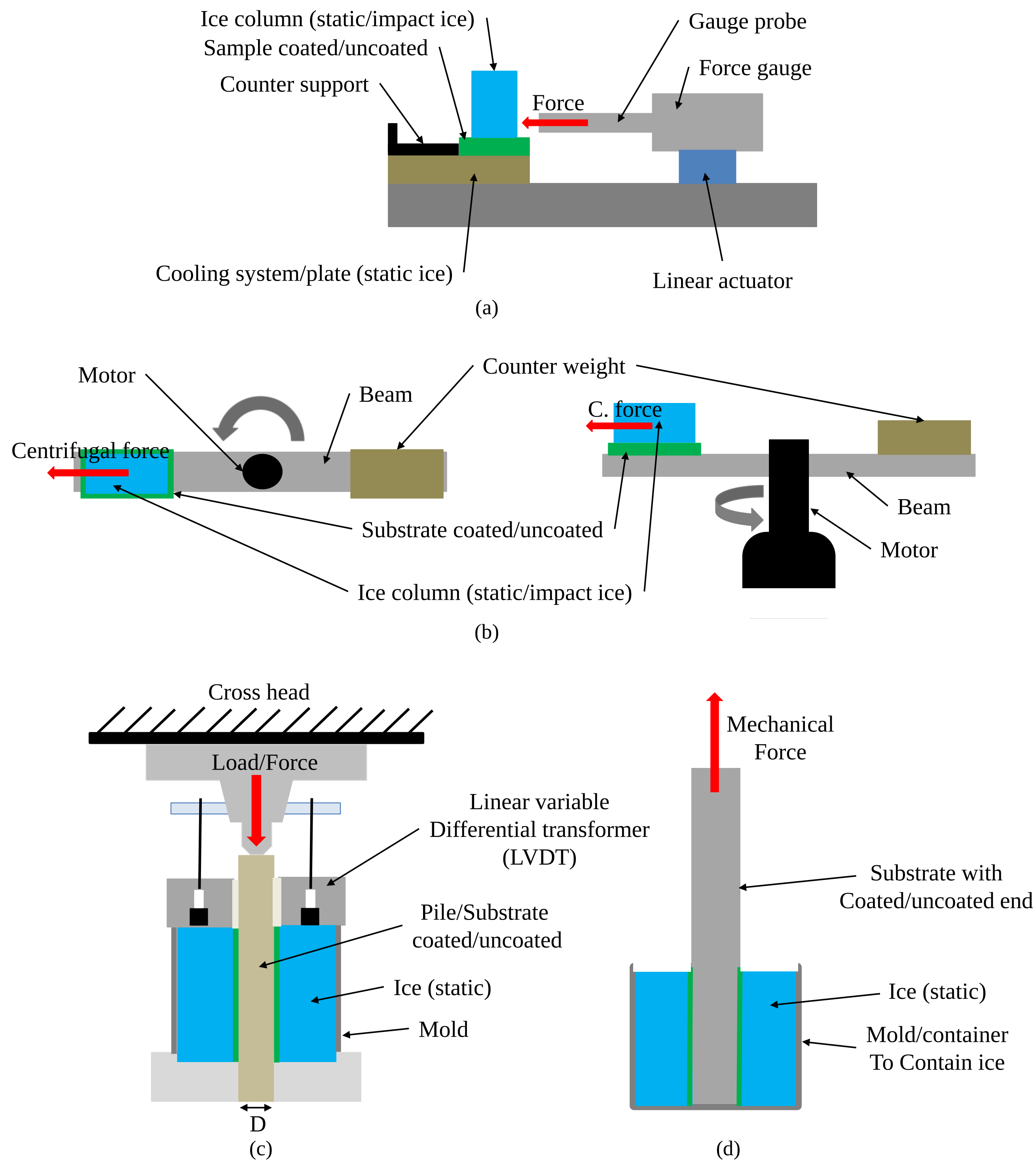

Fig. 5-1 Ice adhesion shear measurements techniques: (a) ice push, (b) ice centrifuge, (c) substrate pin pile push, and (d) substrate pile pull.

Table 5-1 Previous studies of shear ice adhesion using the ice push technique.

Author	Test Type	Ice type	Surface	Shear Strength (kPa)	Roughness (μm)	Icing Area Shape	Area (mm^2)	Height/Volume	T (°C)	Humidity	Surface Preparation
Varanasi *et al.* (2010)	Push	Static	Glass	1075.2	n/a	Rectangular	100	30mm/ 1mL	n/a	n/a	n/a
			Teflon	62.7							
			PDMS	56.1							
Meuler *et al.* (2010)	Push	Static	Steel	698	0.9	Rectangular	100	44mm/1.5ml	-10	n/a	acetone soak, air purge
			PMMA	463							
			PDMS	291							
			PEMA	510							
			Fluorodecyl POSS	250							
			Tecnoflon	389							
Chen *et al.* (2012)	Push	Static	Silicon wafers:		n/a	Rectangular	100	30mm/1ml	-15	n/a	n/a
			Superhydrophilic	913							
			Hydrophilic	202							
			Hydrophobic	77							
			Superhydrophobic	807							
Smith *et al.* (2012)	Push	Static	Bare steel	~420	n/a	Rectangular	100	44mm/1.5ml	-15	n/a	n/a
			Silanes, thiols, and polymer coatings	~130							
					1.33						
Makkonen (2012)	Push	Static	Aluminum	490	n/a	Circular	706.86	10 mm	-10	n/a	n/a
Fu *et al.* (2014)	Push	Static	Glass	820	0.001	Circular	254.5	n/a	-10	n/a	acetone, ethanol, DI water, heat dry
Wang *et al.* (2014)	Push	Static	PMMA Coating	338	n/a	Circular	44.2	20/ 200μl droplet	-10	n/a	n/a

Table 5-1 continued

Author	Test Type	Ice type	Surface	Shear Strength (kPa)	Roughness (µm)	Icing Area Shape	Area (mm^2)	Height/Volume	T (°C)	Humidity	Surface Preparation
Ozbay & Erbil (2016)	Push	Static	Aluminum	731	1.27	Circular	n/a	50µl	-10	58.6% (RH) after 60 min	acetone, ethyl alcohol, DI water, oven dry
			Stainless Steel	1010	2.39						
			Polypropylene	640	1.87						
			PTFE	268	2.03						
			Copper	1217	1.33						
He *et al.* (2017)	Push	Static	Aluminum	487	n/a	Circular	n/a	n/a	-18	n/a	n/a
			Steel	714							
Golovin & Tuteja (2017)	Push	Static	PDMS with oil	64	n/a	Rectangular	100	5-8mm	-10	n/a	n/a
Beeram *et al.* (2017)	Push	Static	Aluminum	450	220 grit	Circular	500	n/a	-8	n/a	n/a
				390	400 grit						
				340	1000 grit						
				300	2000 grit						
				130	mirror polish						
Pervier (2012)	Push	Impact	Mirror polished Ti.		n/a	Rectangular	n/a	3mm		n/a	ethanol, heat dry
		50m/s		12000					-12		
				8500					-10		
				6000					-8		
				3500					-5		
		60m/s		4500					-5		

Table 5-2 Previous studies of shear ice adhesion using the ice centrifuge technique.

Author	Test Type	Ice type	Surface	Shear Strength (kPa)	Roughness (µm)	Icing Area Shape	Area (mm²)	Height/Volume	T (°C)	Humidity	Surface Preparation
Janjua *et al*. (2017)	Centrifugal	Static	Aluminum	152	0.295	Rectangular	600	2 mL	-5	26%	n/a
Laforte & Beisswenger (2005)	Centrifugal	Impact (~ 5 m/s)	Aluminum	350	n/a	Rectangular	1211.6	10 mm	-10	n/a	n/a
Menini & Farzaneh (2009)	Centrifugal	Impact (9.3 m/s)	Aluminum	505	n/a	Rectangular	645.16	10 mm	-10	n/a	Acetone, DI water rinse
Dotan *et al.* (2009)	Centrifugal	Impact (~ 5 m/s) Impact (> 5 m/s)	Aluminum	200-500 240-1350	n/a	n/a	1100	7	-8 -15	n/a	n/a
Kulinich & Farzaneh (2009)	Centrifugal	Impact (10 m/s)	6061 Al. ZrO2 fluoropolymer suspension	362 191	n/a	Rectangular	960	10	-10	n/a	polished and cleaned with organic solvents
Farhadi *et al*. (2011)	Centrifugal	Impact (10 m/s)	6061 Al: CeO2 spin coating Etched coating Ag nanoparticle spin coat Vulcanized rubber spin coat Mirror polished uncoated	 200 110 280 240 362	n/a	Rectangular	960	10mm	-10	n/a	n/a
Arianpour *et al.* (2016)	Centrifugal	Impact (10 m/s)	Aluminum	242	n/a	Rectangular	960	10	-10	n/a	Before polish: ultrasonic acetone clean, DI water After polish: methanol, acetone, DI water, nitrogen blow dry, oven dry

Table 5-3 Previous studies of shear ice adhesion using the other techniques.

Author	Test Type	Ice type	Surface	Shear Strength (kPa)	Roughness (μm)	Icing Area Shape	Area (mm^2)	Height/Volume	T (°C)	Humidity	Surface Preparation
Susoff *et al.* (2013)	Pin Push (Zero-degree cone)	Static	Aluminum	1573 (bare Al) 1594 2562 3901 2681 >2900	-- 0.246 0.58 0.794 0.291 1.3-1.4	n/a	3700	n/a	-14	n/a	degreased and cleaned
Tepylo & Huang (2018)	Lap shear test	Static	Aluminum (sandblasted)	447	n/a	Rectangular	1250	1mm/ 6mL	-20	n/a	n/a
Balordi *et al.* (2019)	Vertical pin pull	Static	Dynasylan SIVO Clear EC coating Dynasylan SIVO Clear EC coating Aluminum	800 780 1000	0.30 (Untreated) 0.94 (Sandblasted) 0.03 (Polished)	n/a	n/a	40ml	-19	n/a	basic soap clean, ultrasonic acetone bath, nitrogen flux dry
Chu & Scavuzzo (1991)	Axial loading	Impact (58m/s)	Aluminum Stainless Steel	~250 ~250	0.1-0.3	n/a	n/a	6.4-9.5 mm	-15	n/a	acetone dip, air dry

The commonly used technique for ice adhesion shear is the ice push test, which can either be set up in a vertical or horizontal plane [118,171,182–190]. The method generally consists of generating ice on a sample's surface and having a linear actuator move a force gauge or load cell into the ice (parallel to the substrate surface) until the ice is broken (as shown in Fig. 5-1a). The force required for ice fracture is then recorded and used to compute the ice shear adhesion strength based on the surface adhesion areas. Probe height relative to the surface, probe speed (ice strain rate), and ice accretion methods (static or impact) can vary between studies. One study reported that ice shear strength decreases with increasing probe height since this creates a moment that adds a tensile component as probe height increases [187]. Therefore, minimizing the probe height can minimize this moment, and reporting the ratio of probe height (relative to the ice thickness) helps characterize the ice push test.

Another common technique is the centrifuge adhesion test (CAT), which shears the ice off a beam through centrifugal spin force (as shown in Fig. 5-1b) [139,191–199]. This technique generally employs a beam attached to a servomotor at its midpoint along its length. While stationary or at a fixed rpm, ice can be generated at one end of the beam and a counterweight attached to the other end to balance the beam and minimize vibrations. Once balanced, the servomotor will continuously accelerate the spin rate until ice fracture occurs. Laforte & Beisswenger [191] first described the CAT, but the angular acceleration and setup details have varied in subsequent studies.

Other less common ice shear adhesion techniques have also been used [41,131,143,200–202]. One is the substrate/pile push test (also known as the zero-degree cone test), which consists of an inner pile and outer cylindrical shell mold as shown in Fig. 5-1c. The pile and mold are placed concentrically with a gap in between. Water is then poured into the gap between the mold and pile and the water is frozen to create ice. To measure the sample's surface ice adhesion, a force is applied to the pile axially along the cylindrical shell/inner pile until it is pushed out and measured with a load cell. This test tends to lead to higher reported shear strength values, and this may be related to difficulty in closely aligning the force and all surfaces and that the entire mass can be in a state of compression after freezing.

Another technique is the vertical substrate/pile pull test, which also uses a pile, but employs a tensile mode instead of a compressive mode to apply a shear force. The technique is shown in Fig. 5-1d and is performed by freezing a test sample pile in ice and then pulling it out. However, the test sample is not necessarily a concentrically fitted cylinder. The lap shear test is also another technique that consists of small plates with a gap between them, in which water is injected and then frozen to create a lap joint. Once frozen, the plates are pulled apart parallel to the icing surface until ice fracture occurs. There are other techniques besides the ones mentioned herein, but the above are the most common.

Along with the different types of procedures used to create the shear force, previous tests also varied in terms of how the ice itself is formed. The most common method is to employ static ice, also called "freezer ice", which is created by freezing a specific volume of water, usually in some sort of mold. The majority of horizontal/vertical push shear adhesion tests in Table 5-1 and Table 5-3 used static ice. Specific parameters of the freezing (time and temperature), substrate (size, material, preparation and roughness), as well as the air (humidity and temperature) can vary. As shown in Table 5-1, Table 5-2 & Table 5-3, these parameters generally vary or are sometimes not reported. This may explain the differences in the ice adhesion values that were obtained and the lack of enough data to determine individual parametric influences across studies. The second method is impact ice, which is formed by spraying a micro-droplets of water at velocities of 5 m/s or greater onto a substrate. Most of the centrifugal tests listed in Table 5-2 used impact ice. This type of test includes additional degrees of freedom (beyond that for impact ice) in terms of the drop characteristics (size, concentration, velocity, and temperature). It should be noted that ice adhesion strength can be correlated to the fraction of the ice still remaining on the substrate after fracture [103,118], but generally this fraction is not reported.

As mentioned above, surface preparation methods have varied between studies. Many studies used acetone or ethanol as an initial surface cleaning followed by a drying method. Some also included various intermediate surface preparation steps. However, several studies did not report their surface cleaning methods. In terms of surface roughness, some studies created samples of varying roughness through different surface abrasion techniques such as chemical etching or sand blasting. Many of the studies have reported roughness values for both metal and nonmetals using a variety of methods such as profilometers or microscopes. However, the quantification of the roughness has not been complete with some employing height variations using a root-mean-square (R_{rms}) and others reporting an arithmetic average (R_a) or others using wetness-based Wenzel geometry values. In some cases, lateral roughness characteristics were included [120]. In general, these surface roughness characterization methods were only consistent within each study (not across the studies).

As may be expected, the widely varying parameters between studies have led to widely varying shear strengths even when comparing with consistent materials for impact ice. However, there is not a consistent recommended set of test conditions and diagnostics accepted by the industry (e.g., aerospace and others) that: a) reasonably represent atmospheric icing conditions pertinent to the different applications threatened by icing, b) can be completed in a moderately-sized self-constructed lab-scale facility, and c) provide quantitative characterization of the key surface, fluid dynamic and thermodynamic conditions. In addition, none of the previous studies measured shear ice adhesion strength for both impact and static ice on consistent surfaces with a consistent temperatures and technique at typical rime-ice temperatures (-15°C and below) to the authors' knowledge. Finally, no studies reported shear ice adhesion for both impact and static ice when comparing metal-based surfaces with hydrophobic surfaces.

This study aims to utilize reproducible icing conditions with a practical measurement technique to provide ice shear adhesion strength for both static and impact ice at the same air temperature (-20°C). To the authors' knowledge, it is the first for such tests. Furthermore, the tests conducted in this study are the first to investigate thermal transients for both static and impact freezing and the first to consider metal vs. icephobic shear performance within the same facility for both static and impact ice. These tests were conducted in a compact icing research tunnel (CIRT) and on three surfaces: a self-lubricating icephobic coating, an aluminum surface, and a titanium surfaces. This icing wind tunnel is also unique in the sense that it was instrumented and equipped to enable in-situ ice shear adhesion measurement after accretion. This is in contrast to other small-scale wind tunnels that only allow accretion measurements [203]. The data for the present tests is then compared to previously published results for both static and impact ice conditions.

5.2 Materials & Methods

5.2.1 Tested Surfaces

For this ice adhesion study, three surfaces were tested: 1) a commercially available titanium surface (ASTM B348), 2) a conventional aluminum surface (Al-6061), and 3) an aluminum surface coated with a self-lubricated icephobic coating (SLIC). The metals were mechanically abraded so they would possess consistent surface arithmetic roughness *(Ra)* as shown in Table 5-4 and as measured by a Zygo optical profilometer. While the average height of the roughness features were nearly the same, these surfaces had different roughness topographies, as shown in Fig. 5-2. For example, it can be seen that the aluminum surface has more peaks per unit length (smaller lateral wavelengths) compared to that of the titanium.

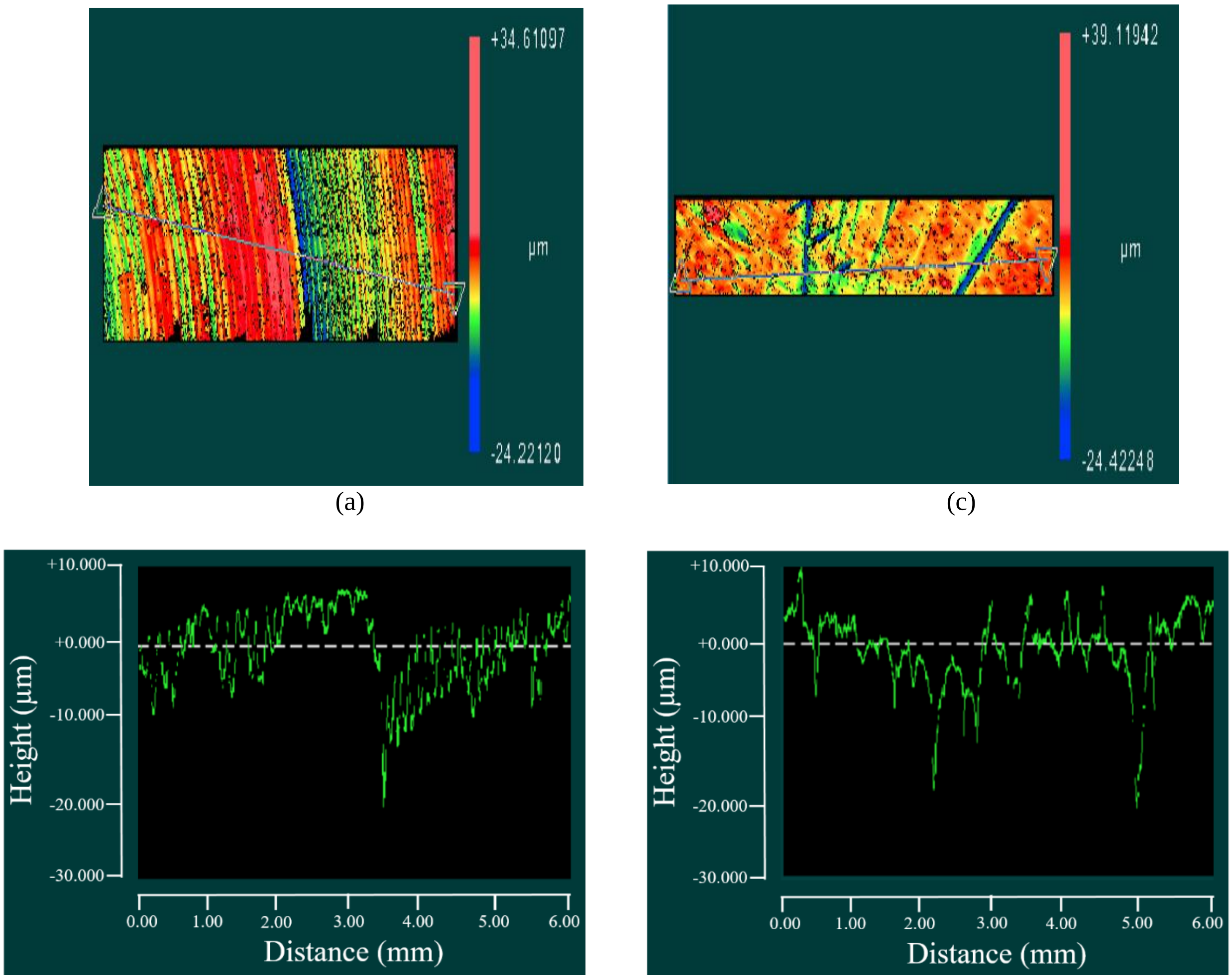

(a) (c)

(b) (d)

Fig. 5-2 Images of aluminum surface map (a) with size of 6.34 mm x 1.93 mm and height profile (b), and that of titanium (c) with size of 7.32 mm x 1.05 mm & (d).

The SLIC coating is a hydrophobic oil-infused elastomer, which was drop-casted on the aluminum substrate. This coating was about 125 µm thick and had an arithmetic roughness of 1.2 µm [110]. Using a Rame-Hart goniometer, the wettability properties (contact and roll-off angles) of the tested surfaces were determined and reported in Table 5-4, with each value being the average of three measurements taken on each sample using 3 different drops respectively. The contact angles were obtained using a 10 µL water droplet, while the roll-off angles were measured with a 20 µL water drop.

Table 5-4 Properties (contact, roll-off angles & arithmetic roughness) of tested surfaces (Al., Ti. & SLIC)

Properties	Aluminum	Titanium	SLIC
Contact Angle (°)	82.4	73.6	99
Roll-off Angle (°)	27	Pinned	13
Roughness, *Ra* (μm)	4.8	4.4	1.2

5.2.2 Ice Shear Testing Facility & Procedures

The ice shear adhesion experiments were conducted for both impact and static ice conditions in a compact icing research tunnel [122]. Impact ice was ice formed as a result of a cloud of 13 microns diameter droplets with a liquid water content (LWC) of 2.8 g/m^3 impacting the test specimen surface in the CIRT test section at a velocity of 35 m/s and temperature of -20°C. On the other hand, static ice was obtained by slowly pouring water in a cylindrical container formed around the test specimen, and allowing it to freeze over time while cooling the ambient air to a temperature of -20°C. It should be noted that deionized water was used for the formation of both impact and static ice to eliminate/reduce variations in ice adhesion strength due to impurities [120,121]. The test specimen/fixture consisted of a boss piece and a 30 mm diameter substrate disc assembly, which was installed in the CIRT test section (as shown in Fig. 5-3). This assembly was either titanium (boss piece and substrate disc made out of titanium) or aluminum (boss piece and substrate disc in aluminum with the possibility of the substrate disc being coated or uncoated). To obtain ice shear adhesion measurements, a horizontal ice push shear test (shown in Fig. 5-1a) was adapted to enable in situ testing in the CIRT. As such, the CIRT was equipped with measurement capabilities to obtain ice shear adhesion strength once ice (either impact or static) was obtained on the mentioned samples' surfaces, as shown in Fig. 5-3. This shear adhesion measurement was achieved by actuating a force gauge attached to a linear actuator, which removes the accreted ice by applying a force through the probe on it (also depicted in Fig. 5-3). Additionally, the force probe was positioned such that its contact with the accreted ice was as low as possible in the setup to minimize any bending moment on the formed ice. The probe was positioned about 1.5 mm above the test specimen's surface as shown in Fig. 5-3 and as shown in ice shear adhesion test videos provided in Appendix B. The resulting ratio of probe height to ice thickness was approximately 0.13. Furthermore, the test fixture was tightly secured in the CIRT test section to minimize undesired motion of the sample during the ice shear fracture process.

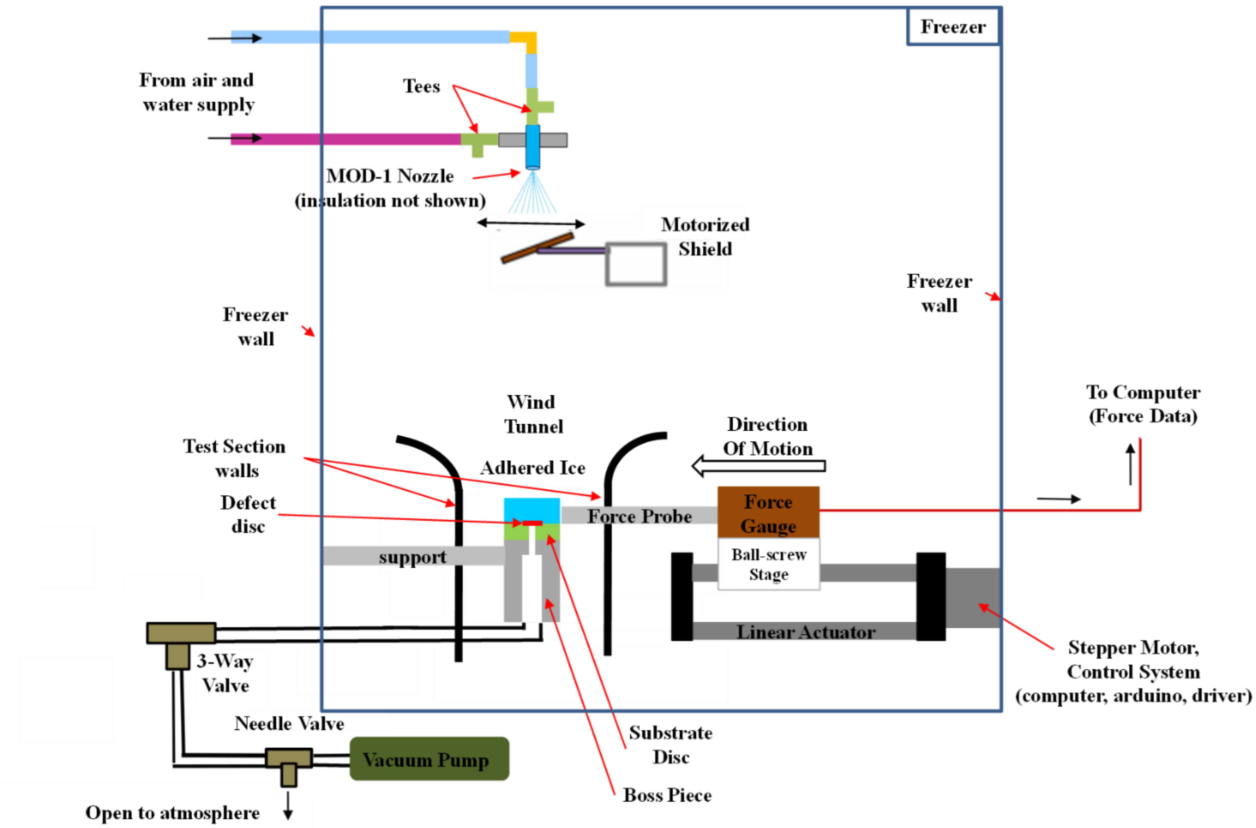

(a)

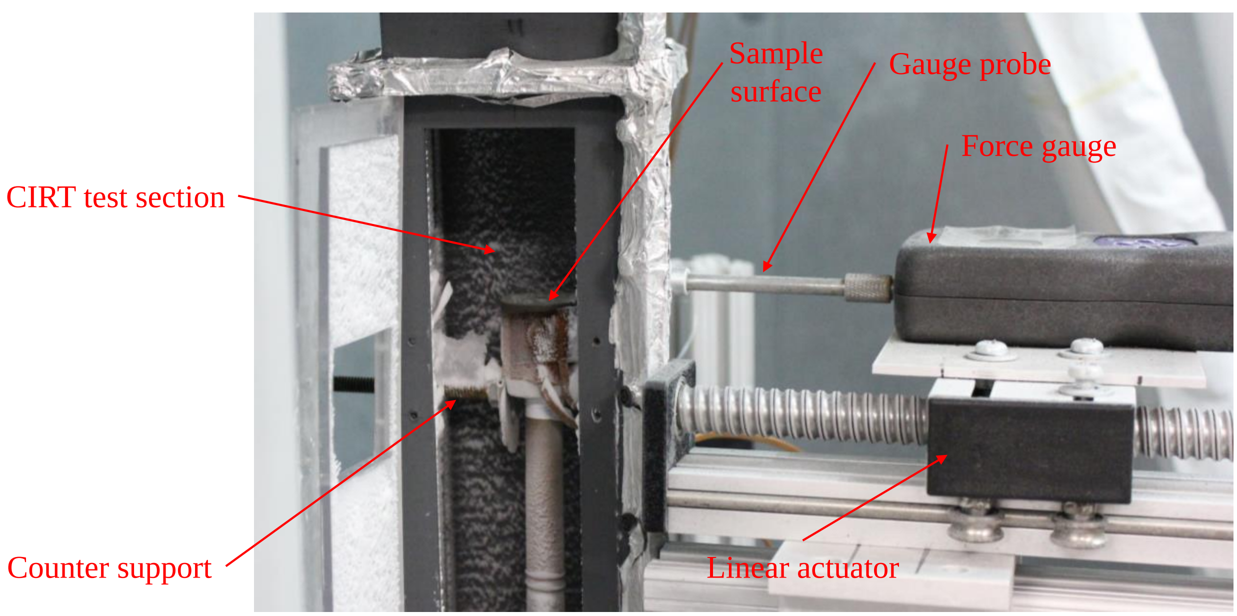

(b)

Fig. 5-3 Ice shear adhesion measurement setup shown in partially shown wind tunnel in: (a) a schematic (not to scale), and (b) a photograph.

Before any icing tests, all metallic substrate discs (aluminum and titanium) were cleaned by wiping their surfaces with a dry Chem-wipe and then with a Chem-wipe immersed in a 95 % isopropyl alcohol to reduce variation in test results, which could be attributed to differences in substrate discs characteristics. This is generally consistent with that of previous studies as presented in Table 5-1, Table 5-2 & Table 5-3. Additionally, one aluminum and one titanium substrate disc was used for all impact and static ice tests to ensure that sample variations could not contribute to ice strength variations and that the measurements were statistically repeatable. Likewise, one SLIC test substrate was used for all impact and static ice tests in order to investigate surface resilience to icing conditions. To prevent any contamination (dirt, dust) to the SLIC surface in between icing tests, the test substrates were preserved in an enclosed box, and were only taken out for icing tests.

Once the titanium, aluminum and SLIC substrate discs surfaces were ready, they were attached to the boss piece (coated or uncoated aluminum substrate disc to aluminum boss, and titanium substrate disc to titanium boss) and the assembly was placed in the CIRT test section. The relative humidity (RH) level prior to starting all icing tests was about 35%. Static and impact ices (shown in Fig. 5-4) were then respectively generated in a series of sequences described in reference [110,122]. Video recordings of impact ice growth on aluminum & the SLIC substrate disc are provided in Appendix B. It can be seen that the impact ice surfaces were more irregular and less translucent. The two types of ice were also expected to be different in terms of ice microstructure and density due to the differences in freezing, all of which can influence ice adhesion strength.


(a)


(b)

Fig. 5-4 Images of ice accreted on substrate disc shown by type: (a) impact ice, and (b) static ice.

As noted in the introduction, ice formation can be associated with thermal transients of the substrate. The present setup was instrumented to provide a well characterized thermal environment with thermocouples (TCs) attached to various surfaces for temperature monitoring during ice formation. In particular, TCs were attached to each substrate disc to show and record its temperature variation during both impact and static icing tests. These TCs were inserted in a ~1mm diameter hole drilled into the test fixture, filled with a high conductivity paste, and covered with an insulation tape for an accurate and precise temperature reading.

For both impact and static ice tests, the ice shear test was initiated after the ice accretion was complete and the test substrate reached the temperature of -20°C. The shear test consisted of moving the force gauge probe at the speed of 1.5 mm/s into contact with the formed ice. The linear actuator was actuated while the force was recorded. The force started to increase once contact was made with the ice, but then decreased immediately once the ice was removed. The force required to remove the ice block from the test sample's surface is termed the critical force, and corresponded to the peak force that was recorded as shown in Fig. 5-5. This value could range as high as 310 N (metal surface in static conditions) to as low as 8 N (SLIC in impact conditions). Using the critical force (F_c), the ice shear adhesion stress (σ) was computed for the tested surfaces and conditions per equation (1) below, where d is the substrate disc diameter.

$$\sigma = \frac{4 \times F_c}{\pi \times d^2} \qquad (1)$$

This stress opposes the removal or sliding motion of ice on a surface [204]. Example recordings of this shear adhesion tests are provided in Appendix B.

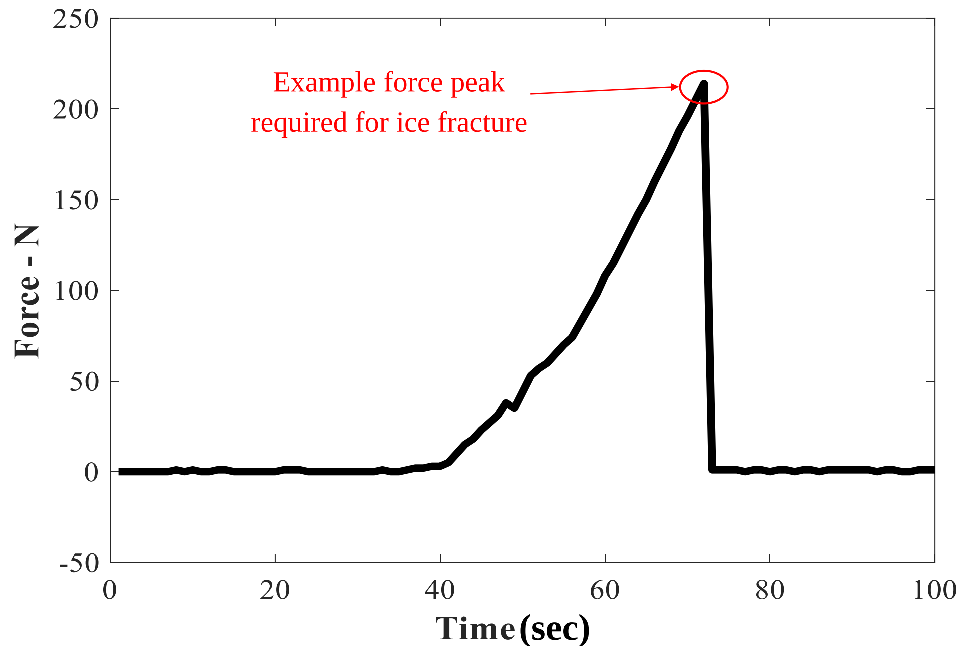

Fig. 5-5 Sample applied force graph over time during ice shear adhesion test.

5.3 Results & Discussion

Using the above method, the remaining ice accreted on the substrate disc surfaces after fracture was also measured. Depending on the amount of ice remaining, the ice failure can be categorized as:

1) adhesive fracture (ice-substrate facture) with no remaining ice on the substrate,
2) cohesive fracture (ice-ice fracture) for which the substrate still covered in ice, or
3) mixed-mode fracture with some ice remaining on the substrate (a combination of adhesive and cohesive fracture)

All the shear tests conducted on the metals (Al. & Ti.) resulted in a mixed-mode fracture. An example of impact ice residue left after fracture on each metal substrate disc is shown in Fig. 5-6. On the other hand, a clean adhesive fracture was observed for all shear icing tests on the SLIC surface (as shown in Fig. 5-7). This outcome was expected, since SLIC has previously demonstrated reduced ice adhesion in tensile mode and other conditions [91,110].

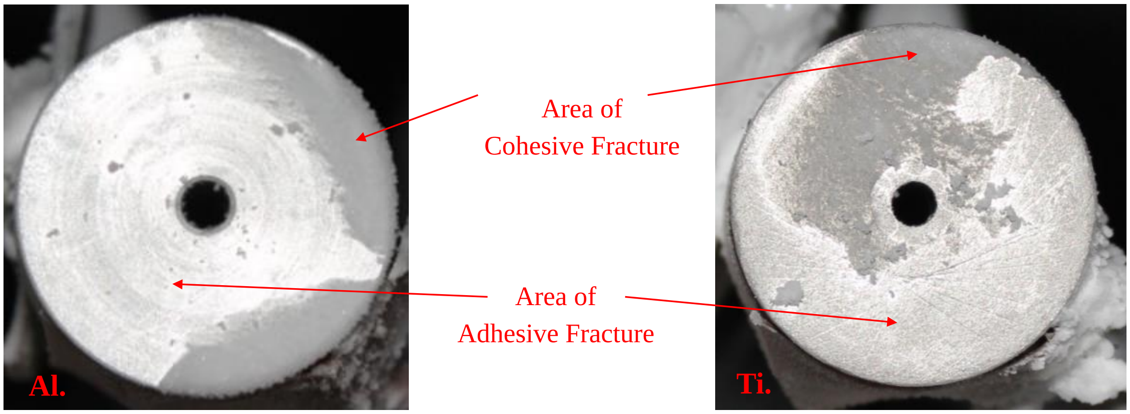

(a) (b)

Fig. 5-6 Residue left after impact ice shear adhesion test shown by area of adhesive & cohesive fracture on: (a) the aluminum surface, and (b) the titanium surface.

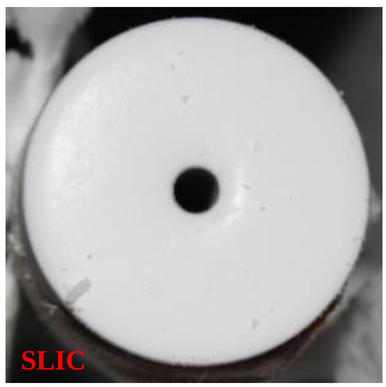

Fig. 5-7 Full ice removal (100% adhesive failure) from SLIC surface after impact ice shear adhesion test.

Table 5-5 below summarizes the average residual ice area for the tested surfaces, showing the difference between adhesive and mixed-mode fractures. The residual ice surface area on the metals were determined using “ImageJ”, which is an image processing software. SLIC’s ability to enable total removal of all the ice accreted on its surface in shear mode (for the tested conditions) confirms it as an icephobic coating. It should be noted that use of a consistent surface preparation and cleaning was important to reduce the variability of these and other measurements. Therefore, this practice is highly recommended.

Table 5-5 Average percentage of the ice residue area after ice fracture

	Avg. % Residue Area Fraction	
	Impact	Static
Al. Surface	38	16
Ti. Surface	26	11
SLIC Surface	0	0

As mentioned in the methods' section, the critical force, F_c, occurs at ice fracture. For the metals, this force was higher for static ice conditions (up to 45% more) than for impact ice conditions. For SLIC, this force peak was consistently much less than that for metals (up to 90% lower) for both impact and static ice conditions. This force reduction confirms the favorable icephobic attributes of this coating. Using Eq. 1, the average ice shear adhesion stress for each surface and condition are shown in Fig. 5-8a in terms of residual ice fraction. It can be seen that SLIC yields both a very low cohesive area (little to no residual ice) along with low adhesion strength. Comparing the two metals surfaces against each other, the adhesion strength on the titanium surface was found to be lower than that for the aluminum surface by 29% for impact ice and by 12% for static ice. This is consistent with findings of experiments in a tensile mode [119].

Comparing impact ice vs static ice, it can also be seen that impact ice (filled symbols) demonstrated a shear adhesion stress lower than static ice (hollow symbols) for the metal surfaces. This finding is opposite of that of Ronneberg *et al.* [205], which conducted their experiments at -10°C using a centrifuge adhesion test. Interestingly, Fig. 5-8a also shows that the lower shear stress for impact ice was accompanied by a higher amount of residual ice. As such, the impact ice may have weaker cohesive strength than static ice due to the differences in the microstructure (where impact ice is an amalgamation of many small freezing events whereas static ice is akin to single crystal growth). This may indicate that the substrate-ice bond is more consistently formed with static ice and that tests results in static ice may not be easily extendable to those for impact ice. Such differences in ice strength may be related to the differences in ambient temperature, in temperature transients, in other aspects of the freezing process, and/or perhaps even in the shear measurement technique itself. Further research is recommended to better understand the many parameters that can influence ice adhesive strength and residual ice fraction on metal surfaces. In addition, it should be noted that measured shear adhesion strength for both conditions on metals demonstrated statistical scatter due to the inherently stochastic nature of ice fracture, and the relative scatter about the mean (typically ±30%) is consistent with the amount of relative scatter seen by other studies [118,171,182–190].

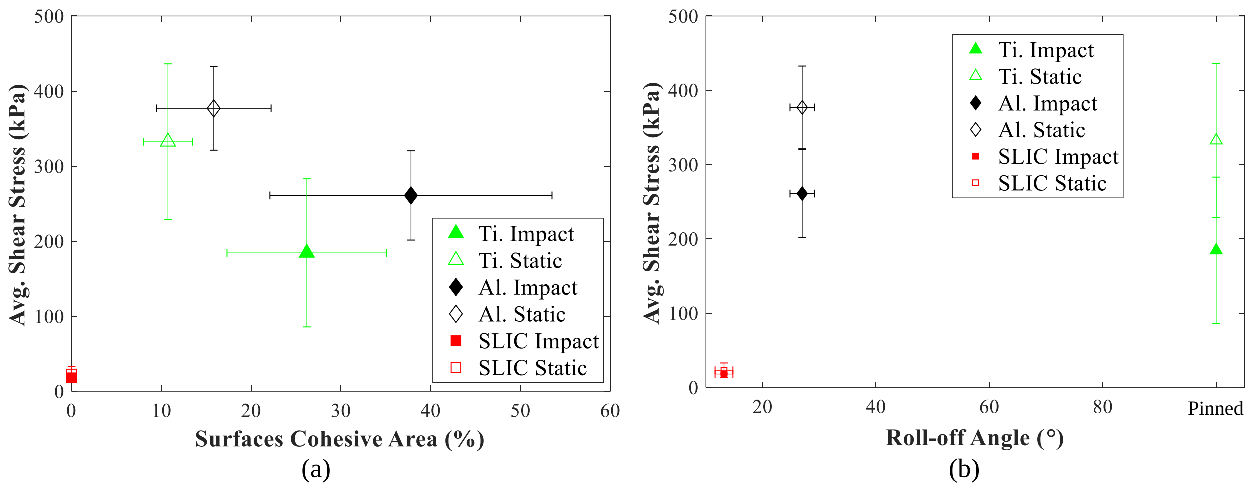

Fig. 5-8 Average ice adhesion shear stress for impact and static ice compared to (a) surfaces cohesive area (residue ice area fraction) and (b) surfaces roll-off angles. Bars indicate one standard deviation.

For SLIC surface, the average shear adhesion stresses for both impact and static ice were similar. Additionally, there was a reduction of about 90% for the SLIC compared to the metals (aluminum and titanium) for both impact tests and static tests. The low adhesion value of about 20 kPa on the SLIC is much lower than that seen for the metals, but low enough for ice to be removed by centripetal acceleration [91]. As such, SLIC could be used as an excellent de-icing tool for rotating components in applications operating at extremely cold temperatures (e.g., gas turbine fan blades).

This consistent low shear adhesion strength on SLIC is attributed to four primary factors: wetting contact angle, wetting roll-off angle, coating elasticity and coating self-lubrication. First, SLIC has a low surface energy relative to water creating a high contact angle, a feature found to be important for many icephobic coatings [91,132,133,183,193–195,206]. However, several studies found that hydrophobicity and icephobicity are not always correlated, i.e. a surface with a high contact angle for water is not enough to ensure low ice shear stress [5,33,120,139,146–148,183]. Perhaps a more important wetting factor is a low contact angle hysteresis or low roll-off angles. In fact, several studies reported that a low roll-off angle has a stronger correlation for reduced ice adhesion [162,165,166,168,171,196,197]. While SLIC does demonstrate a lower roll-off angle, as shown in Fig. 5-8b, it can also be seen that the present results indicate that titanium has a lower adhesion stress despite having a higher roll-off angle.

The third factor that provides an icephobic advantage for SLIC is its elastomeric property, since SLIC is predominantly made of silicone that can deform much more readily than ice. As noted by [168,207,208], this allows the surface to locally deform under shear stress to facilitate fracture between the ice and substrate bond. The fourth factor for SLIC is its self-lubrication whereby the infused oil can create a lubricant layer at the surface (partially responsible for the low roll-off angle) that enables interfacial slippage, which enhances ice release. This interfacial slippage has been noted as an important attribute for several icephobic oil-infused coatings [33,91,168,208]. Furthermore, the SLIC surface icephobicity did not degrade during and after the three icing tests on the same surface, indicating its resilience to icing conditions stemming from self-replenishment of the lubrication layer after an icing event.

As noted in the introduction, ice formation can be associated with a significant temperature rise in the substrate. For impact ice, this temperature increases particularly occurred during the first 35 seconds of the spray impact. Since the droplets were supercooled at the air temperature, the temperature increase is attributed to the substrate's absorption of latent heat in the water during the ice freezing process. For static ice, room temperature water (~22°C) was poured in the container above each substrate disc. The disc at that time was typically at a temperature of -7°C during the cooling process, and was recorded via the thermocouple inserted in the substrate disc. Before freezing, the temperature rise of the substrate can be related to the cooling of the water. During freezing (which took about 85 seconds), the temperature rise can be related to the substrate's absorption of latent heat. To consider these temperature transients, the average temperature rise experienced by each substrate disc respectively was obtained and compared to the cohesive residual ice area fractions as shown in Fig. 5-9. In general, the temperature rises were larger for impact ice (typically +6° C) as compared to static ice. This is consistent with less time for heat to be rejected to the surrounding air (instead of being absorbed by the ice) for the impact ice case. The results for static ice showed that residual ice fractions increased with the substrate temperature rise. This suggests that a closer bond between the substrate and the ice may increase heat transfer between these two surfaces. Regardless, thermal transients in icing can be significant for both metal and icephobic surfaces for impact conditions, and therefore warrant recording to fully characterize the process.

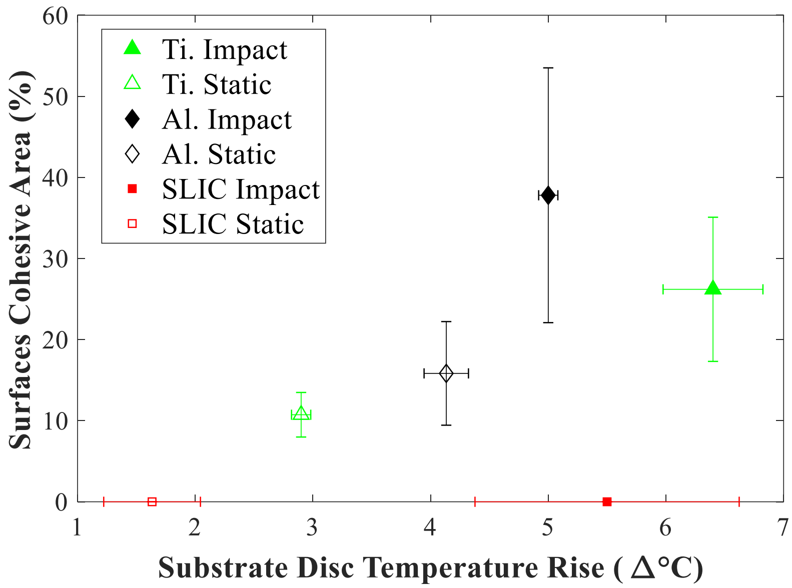

Fig. 5-9 Relationship between substrate disc temperature rise and average surfaces cohesive area (residue ice area fraction). Bars indicate one standard deviation.

In addition to the above comparisons within the present measurement set, the results were compared to those previously reported in the literature (Table 5-1, Table 5-2 & Table 5-3). For metals, Fig. 5-10a shows the comparison of available shear adhesion by ice types and ice adhesion shear measurements used (as grouped in Table 5-1, Table 5-2 & Table 5-3). The ice shear adhesion strength on metals varied from approximately 150 kPa and 1,900 kPa for both static and impact ice, with the exception the data of Pervier *et al.* [118,209] which reported values in excess of 12,000 kPa. This may be attributed to the fact that Pervier used a shear adhesion stress computational equation that emphasized the stress intensity factor along the ice/substrate interface and was different from the commonly used shear stress computation (Eq. 1). Additionally, differences in the shear adhesion data presented in Fig. 5-10a can be attributed to many factors listed as follows (in expected order of importance):

- apparatuses for shear measurement (and computation of stress if different from Eq. 1)
- protocols/procedures used (including surface preparation and cleaning, ice strain rate, etc.)
- surface chemistry (contact and roll-off angles)
- surface topography (roughness height and lateral wavelength)
- thermal conditions (air temperature, substrate temperature, freezing rate, heat transfer avenues)
- droplet conditions for impact ice (temperature, velocity, size and concentration)

Unfortunately, none of the previous studies provided all of these parameters, as was done for the current study. The authors, therefore, recommends future studies provide such details to allow for better quantitative correlation. Despite these differences, one qualitative trend may be identified. Generally, static ice has a higher shear stress adhesion than impact ice for metals.

Measurements of the present SLIC coating and other non-metal surfaces previously reported in the literature (Table 5-1, Table 5-2 & Table 5-3) are shown in Fig. 5-10b. Though the majority of these coatings were successful at reducing ice shear adhesion strength, a few of them demonstrated adhesion values similar to or higher than that of metals (as shown in Fig. 5-10a). One example is the superhydrophobic silicone of Chen *et al.* [183], which has a shear adhesion stress of about 850 kPa, thus demonstrating that superhydrophobicity does not necessarily equate to icephobicity. Other factors (e.g. coating elasticity and self- lubrication, which can allow for surface interfacial slippage) are also important. Notably, SLIC was found to be the best-performing surface (for both impact and static ice conditions) among these coatings.

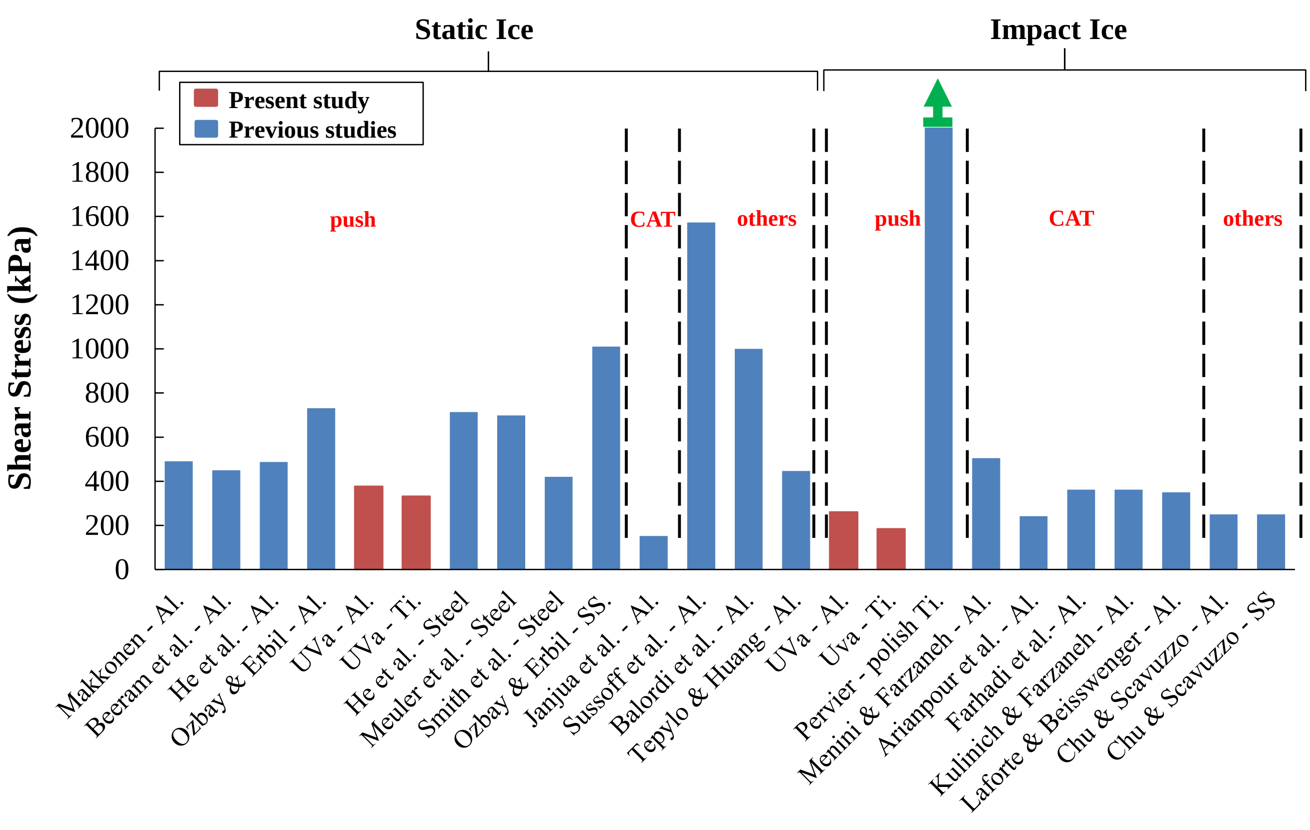

(a)

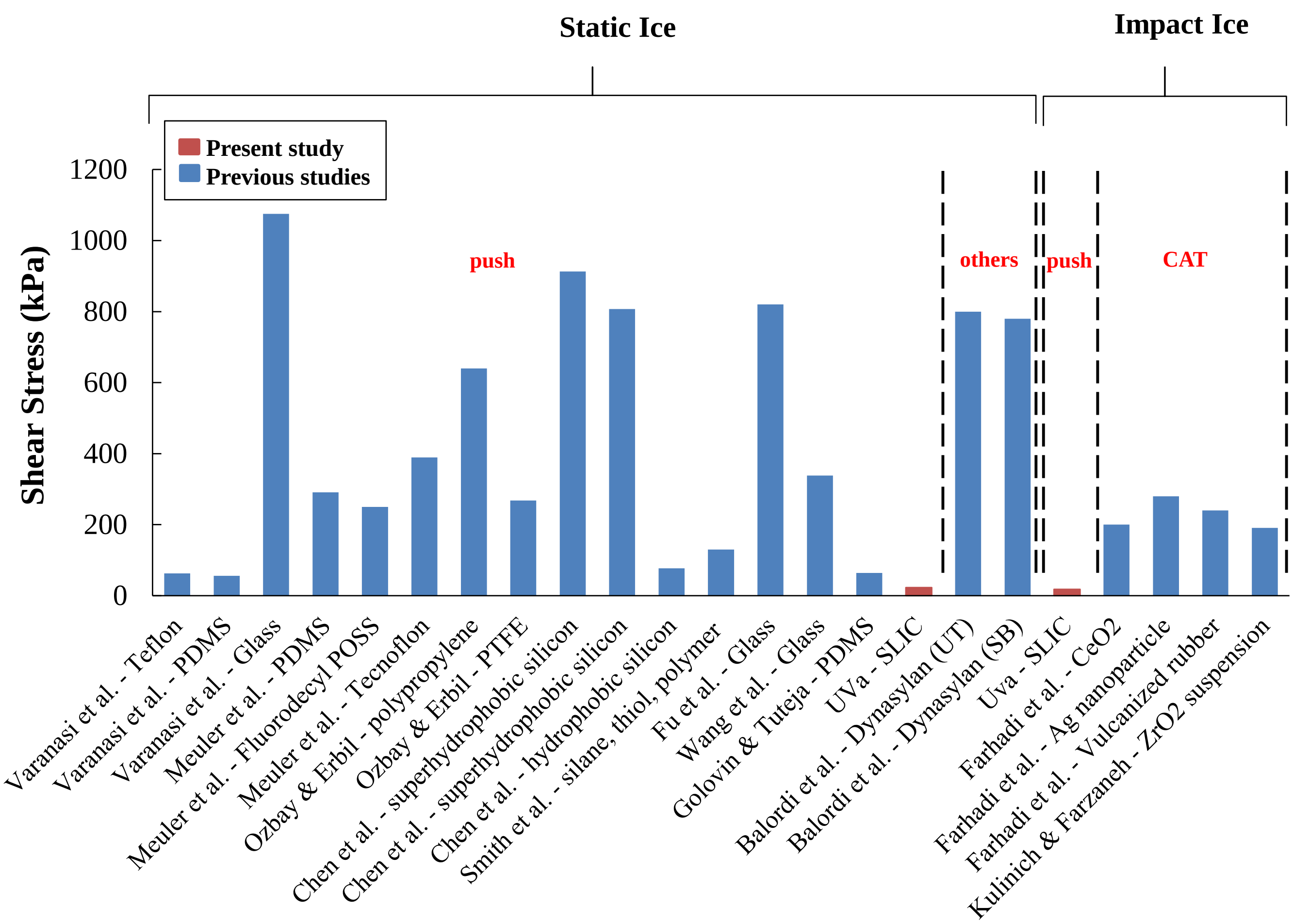

(b)

Fig. 5-10 Shear adhesion stress values comparison of this study (red bars) with previous data (blue bars) reported in the literature for: (a) metals, and (b) icephobic coatings.

5.4 Conclusions

This study presents ice shear adhesion stress data measured on a self-lubricating icephobic coating surface and on aluminum and titanium surfaces for both impact and ice conditions. These measurements were conducted in an icing wind tunnel, which was equipped with measurement capabilities to characterize the test conditions and obtain ice shear adhesion strength. For static ice, deionized water contained in a cylindrical mold was left to freeze gradually on the test surfaces at a temperature of -20°C. For impact ice, super-cooled 13 μm droplets impacted the test surfaces at a velocity of 35 m/s and at a temperature of -20°C. The results revealed that static ice has a shear adhesion strength higher than that of impact ice for the metals. Additionally, a reduction of more than half in shear adhesion strength was observed for the SLIC surface compared to the metals. Temperature rise was found to be significant for both metals and icephobic coatings during ice accretion with impact testing. This rise was not correlated with residual ice fraction for impact ice, but was found to be correlated for static ice, indicating significant differences between these two conditions. Lastly, a comparison of the present study's data with that reported in the literature for ice shear adhesion strength revealed that SLIC outperformed other surfaces for both the impact and static ice conditions. Additionally, SLIC did not lose its icephobicity throughout all the tests performed.

Moreover, this study recommends for future ice shear testing that testing include thermal measurements for the substrate temperature and specify/characterize all of the following:

- apparatuses for shear measurement (and computation of stress if different from Eq. 1)
- protocols/procedures used (including substrate samples' preparation and cleaning)
- surface chemistry (contact and roll-off angles) and roughness (magnitude and wavelength)
- thermal conditions (air temperature, substrate temperature, freezing rate, heat transfer avenues)
- droplets' conditions for impact ice (temperature, velocity, size and concentration).

Chapter:

6 Trends of Impact Ice Adhesion on Various Surfaces

6.1 Introduction

Icephobic surfaces have been extensively investigated within the last decade as an optional solution to the icing threats to various applications (e.g., power lines, wind turbines, aircraft). The key feature of these surfaces is that they exhibit reduced adhesion, thus can facilitate ice removal or retard its formation [89,91,110,162]. In some cases, this ice adhesion reduction factor was found to be linearly related to the reduction of ice accumulation [89]. However, usage of such surface is hindered by robustness issues for icephobic surfaces, including resistance to mechanical abrasion, to long-term weather exposure, and to various chemicals [89,139,141–143,173]. Another issue hindering their usage is that reported ice adhesion measurement on these and other surfaces (metallic and non-metallic) can vary by more than two orders of magnitude between studies [176]. These wide ranges of values may be attributed to differences in test conditions as indicated by Fig. 6-1, which shows a schematic of a push test, a widely used technique to measure surface ice shear adhesion strength. As shown in this figure, there are many factors (marked in red) that may affect the ice adhesion and typically vary across studies. These features become especially complicated for impact ice, which is ice accretion for aerodynamic flow past a surface with supercooled droplet deposition [91,119]. Impact ice is the ice of most concern for wind turbines and aircraft. In contrast, static ice occurs when a pool of water is stationary over a surface as the surface and/or water are chilled. Notably, most reported values of ice strength adhesion are based on static ice as it is simpler to test.

For impact ice, there are standards specifying the air temperature and Liquid Water Content (LWC) for aerospace icing conditions such as FAA Guidelines Parts 25 and 33 [12–14]. Particularly, in terms of ice accretion in a wind tunnel, there exist the SAE ARP 5905 [114] that is a set of aerospace recommended practice governing calibration and acceptance of icing wind tunnels. Other examples include SAE AIR5320 [210] for summary of icing simulation test facilities and SAE AIR6189 [211] for design, calibration and test methods for turbine engine icing test facilities. However, there are not accepted standards for wind-tunnel testing of ice adhesion that specify all the factors listed in Fig. 6-1. In fact, there are even no standards for static ice adhesion measurements. As a result, it is difficult to make a qualitative comparison of reported ice adhesion strength across multiple studies in order to obtain trends validated by multiple sources. To help address this complex issue, Laforte proposed that ice adhesion studies report Adhesion Reduction Factor (ARF), which is the normalization of the ice adhesion strength of tested surfaces including icephobic by that on a smooth aluminum surface or a similar metal [89]. This practice has been adopted by some new studies [143,154,194] but no investigations have yet demonstrated whether ARF improves cross-study comparisons.

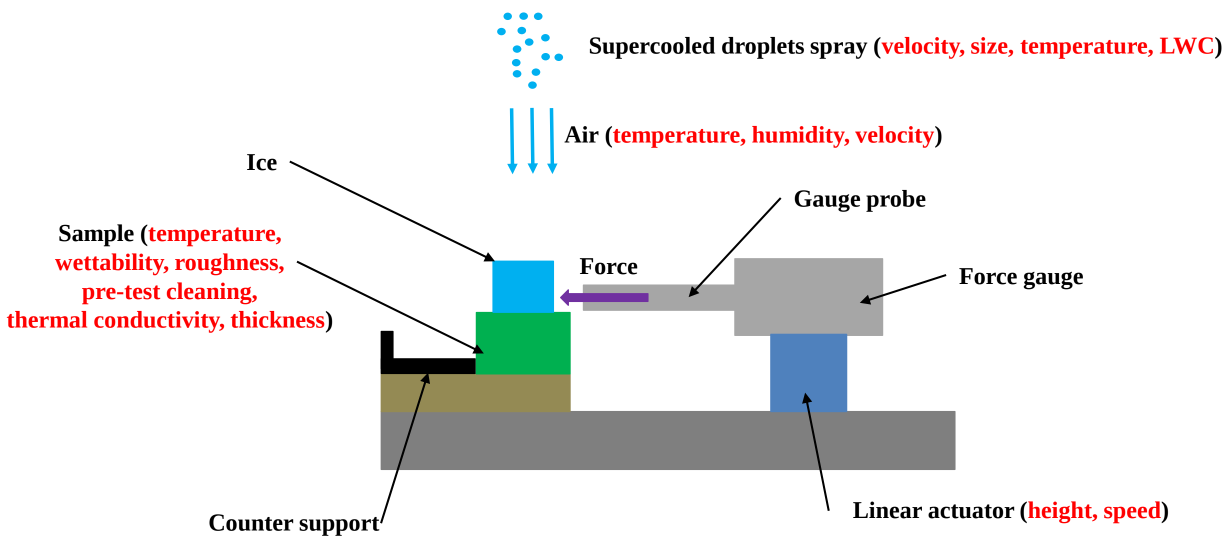

Fig. 6-1 Schematic of an ice push shear measurement technique showing key elements of the accretion and test technique and some of the associated factors (in red) that may affect ice adhesion.

To help predict potential icephobicity of surfaces, Meuler *et al.* [171] suggested a relationship between ice shear adhesion strength (τ) and surface wettability. In particular, they employed the work of adhesion on the basis of Young-Dupre equation along with capillary force balance arguments to show that the receding angle of a surface, θ_{rec}, can theoretically influence ice adhesion shear strength with the following proportionality

$$\tau \propto (1+\cos\theta_{rec}) \tag{1}$$

Subsequent static ice studies confirmed this relationship, where icephobic surfaces generally possessed a high receding angle [131,197,212]. However, most of these studies were conducted using static ice (inert water frozen atop a surface) and not cross-compared for impact ice. Another set of studies proposed a relationship between ice shear adhesion strength and roughness, and subsequently sparked the creation of geometrically-textured surfaces (geometric surfaces with pillars and pores) to reduce ice adhesion [154,213]. However, these surfaces are fragile and not suitable for aerospace. Therefore, they would not be discussed in this manuscript. Other researches established relationship between ice shear adhesion strength and many other factors (such as air temperature, surface contact angle, elastic modulus, and roughness, etc.) [103,208,214,215]. But again, no study has yet cross-compared against data sets for impact ice. As such, this manuscript aims to review existing models of ice shear adhesion strength models (for both icephobic and non-icephobic surface) with impact ice data from several studies in terms of the receding contact angle, elastic modulus, roughness, temperature, etc.. To the authors' knowledge, this is the first of such study to consider all these aspects among several studies, and especially the first to investigate them in the context of impact ice.

6.2 Adhesion Influencing Parameters

6.2.1 Influence of Wettability and Material Elasticity

To determine whether the correlation of receding angle proposed by Meuler *et al.* [171] for static ice shear adhesion strength would apply for impact ice, data from a variety of static and impact ice studies that characterized this wettability were considered as shown in Fig. 6-2a [131,171,182,194,197,203,208,212,215]. The impact ice data are shown with the filled symbols, while that of static ice are shown with hollow symbols. This plot also took into consideration the shear measurement technique used. The blue symbols were obtained using the push ice shear adhesion measurement technique (Fig. 6-1), while the green symbols indicates data taken using a centrifuge adhesion test as described in references [191,196,216]. The symbols in magenta are data collected using any other technique (e.g., zero-degree cone test, lap shear, etc.). The results indicate that a reduction of ice shear adhesion strength is observable for very high receding angles (data in the left corner of the plot marked by Region A) for both static and impact ice. This is consistent with the correlation proposed by Meuler *et al.*, and Region A corresponds to superhydrophobic surfaces with a contact angle greater than 155°. High receding angles for a surface are typically obtained through superhydrophobic surfaces with micro or nano-texture design to preserve a Cassie low-wetting state. These surfaces often suffer from a lack of mechanical robustness and the wetting state can be lost under high impact velocities [89,91,110,162].

Interestingly, a second region of low ice adhesion strength on the tested icephobic surfaces was observed as denoted by Region B in Fig. 6-2a and these represented coatings with soft surfaces. If one excludes Region B and focuses on Region A, one may estimate the relationship between shear adhesion strength of ice and surface wettability for hard surfaces as

$$\tau \sim 350\ \text{kPa}\left(1+\cos\theta_{rec}\right) \tag{2}$$

This relationship is given by the line in black in the plot on Fig. 6-2a and roughly corresponds to the static and impact data (excluding that in Region B). Similar plots were also investigated for shear strengths for static and impact as a function of static and advancing wetting angles, but neither of these provided as good of a correlation as that for receding angle. In addition, while the receding angle provided the best correlation, there is still significant variation of the data about this line, and much of this can be attributed to difference in other factors listed in Fig. 6-1, as well as the stochastic nature of ice strength that is related to the randomness of defect formation during ice accretion or freezing. However, there does not appear to be a consistent trend with respect to the test technique (indicated the color of the data symbols).

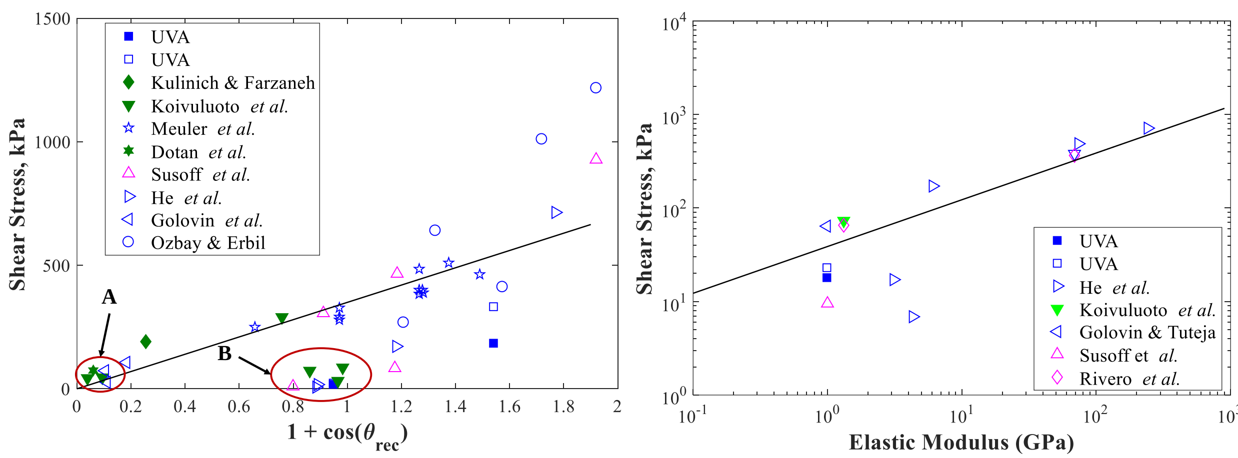

(a) (b)

Fig. 6-2 Ice shear adhesion strength (where filled symbols indicate impact ice and hollow symbols indicate static ice) as a function of (a) surface receding angle (all surfaces) and (b) surface elastic modulus (for hydrophobic and hydrophilic surfaces only). In addition, blue symbols indicate data for a push test, green symbols indicate data from a centrifuge adhesion test, and magenta corresponds to all other test techniques.

As noted above, a second region of low ice adhesion strength on the tested icephobic surfaces was observed as denoted by Region B in Fig. 6-2a. These were soft hydrophobic surfaces with receding contact angles in between

95º and 135º. This high level of performance (low ice adhesion) for soft materials (low modulus of elasticity) is consistent with a recent proposed relationship for static ice [167,217] given as

$$\tau \propto \sqrt{\frac{E\ G}{\Lambda}} \tag{3}$$

Where E is the elastic modulus, G is the surface energy, and Λ is the material thickness. This relationship was derived based on general observation in adhesion pull-off tests and on the property mismatch and deformation incompatibility between ice and substrate [218,219].

To further investigate the potential relationship between elastic modulus and ice shear adhesion strength, the data for nearly hydrophobic surfaces (receding contact angles in between 65º and 105º), in addition to a few metallic surfaces, were considered as a function of modulus. Most of the soft surfaces with low ice adhesion employed polydimethylsiloxane (PDMS). If one only considers the data for hydrophobic and hydrophilic surfaces (receding contact angles less than 105º) as shown in Fig. 6-2b, there is a qualitative trend between elastic modulus and ice shear adhesion strength. On this log-log plot, the data tend to follow a line with the slope of 1/2 (the constant of proportionality from Eq. 3) indicating that the influence of surface softness is significant to shear ice adhesion strength. However, there is still quite a bit of variation about this trendline (which can be related to other factors listed in Fig. 6-1) and there does not appear to be a consistent trend with respect to the test technique (indicated the color of the data symbols). It should be noted that the trends of wettability and modulus of Fig. 6-2 were also considered in terms of the dimensionless Adhesion Reduction Factor [89], but this did not improve the correlation for either Fig. 6-2a nor Fig. 6-2b. This indicates that Eqs. 2 and 3 are best considered in terms of absolute stress values (whereas taking the ratio of two values which both have uncertainty appears to introduce even more uncertainty in these relationships). As such, only absolute (dimensional) values of stress are considered in the remaining plots. Additionally, it should be noted that receding angles are typically based on drops that are a few millimeters in diameter and therefore do not necessarily reflect surface wetting aspects for drops that are tens of microns in diameter (as is typically observed for aerospace icing).

6.2.2 Influence of Roughness and Temperature

Some studies have also proposed ice adhesion models based upon surface roughness and air temperature based on their own data set [131,187,200,214,216]. Such studies often note that ice adhesion increases with increasing roughness or with decreasing air temperature. To determine whether such trends are consistent across data sets, especially for impact ice, these two parameters are plotted against ice shear adhesion strength in Fig. 6-3 for the studies in which roughness and/or temperature were reported [103,139,143,171,182,212,214,215,220]. Regarding surface roughness, the qualitative trend of increasing adhesion strength with roughness height is observable for both static and impact ice data as shown in Fig. 6-3a. However, there is wide variation in the adhesion data, especially for surfaces with roughness amplitudes greater than 1μm. This could be related to the influence of surface features on surface wettability for droplets that are on the order of tens of microns. Therefore, it is difficult to establish a quantitative trend solely based on roughness. This data includes roughness levels that are typical of the initial surface finish of aerospace components (about 0.1-1 μm) and that typical of such components after environmental or mechanical degradation takes place (greater than 1 μm).

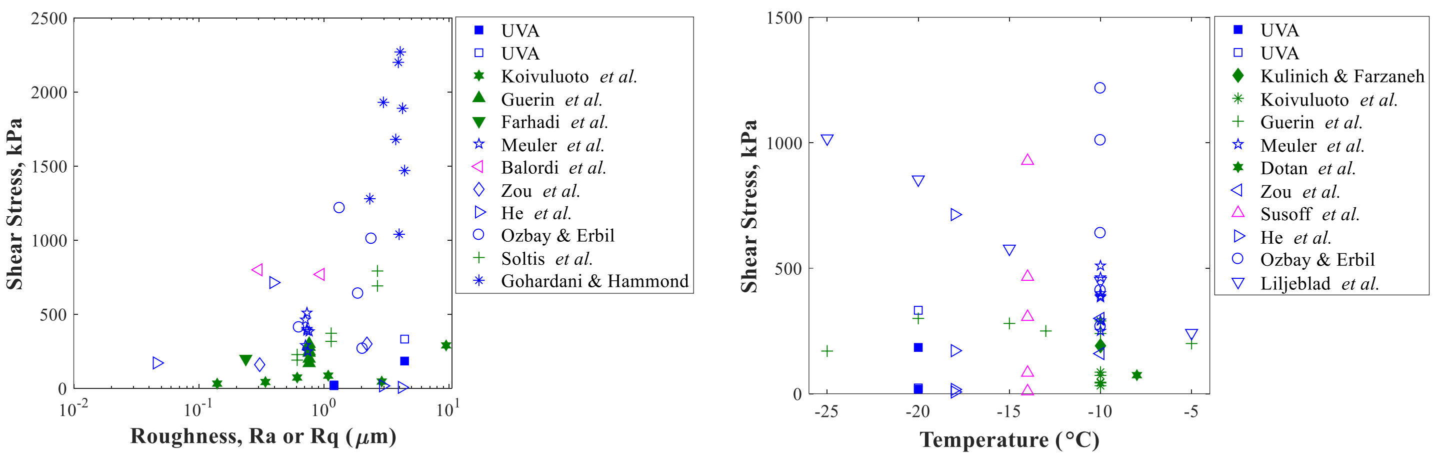

(a) (b)

Fig. 6-3 Ice shear adhesion strength (where filled symbols and + and * symbols indicate impact ice while hollow symbols indicate static ice) as a function of (a) surface roughness (for a variety of temperatures), and (b) air temperature (for a variety surface roughness), where the symbol color is the same as used for Fig. 6-2.

The trends with respect to temperature are shown in Fig. 6-3b and are not as clear. This may be related to the fact that most of the studies used a single temperature for testing, so variations in temperature for Fig. 6-3b are generally between different studies. One of the few studies that varied temperature was the impact ice data of Guerin *et al.*'s [green + symbols in Fig. 6-3b] for which the average ice shear adhesion was found to increase as the temperature dropped from freezing and peaked at -20°C. Even colder temperatures resulted in decreasing shear strength measured due to mostly cohesive failure (ice-ice fracture) rather than adhesive failure (ice-substrate interface fracture). This suggests that the adhesion strength is not actually decreasing, since characterizing the latter in term of cohesive failure is not appropriate. This trend is consistent with qualitative observations of several studies for shear adhesion (pulling the ice along the surface) for static ice [103,216,221–223]. For tensile adhesion (pulling the ice up and away from the surface), a similar trend was noted whereby ice adhesion strength increased as the temperature dropped from freezing and was found to be greatest at -15°C beyond which colder temperatures resulted in predominantly cohesive failure [118]. However, when comparing all the data in Fig. 6-3b, there is surprising little evidence of a strong trend with respect to air temperature, except that the adhesion is generally smaller at -5 ºC (typical conditions for glaze ice) as compared to that for -20 ºC to -10ºC (typical conditions for rime ice). This is true for both static ice and impact ice, indicating more studies on the effect of temperature are needed.

It should be noted that there are many other factors beyond surface wettability, modulus, roughness, and air temperature that are expected to influence ice adhesion strength as listed in red in Fig. 6-1. These factors include other coating characteristics (thickness, temperature, thermal conductivity and surface preparation), droplet characteristics (velocity, temperature, size, and LWC), air characteristics (velocity and humidity) and the testing technique (the rate and height of load application). Accordingly, there is not enough data between studies (or insufficient reporting of the variables) or among the surveyed sources to establish trends for all these factors that can be validated with consistency. As an expected consequence, the surveyed results indicate a dramatic variability of ice adhesion strength between studies as shown in Fig. 6-2 and Fig. 6-3. As such, it is recommended that standard impact ice guidelines be developed to govern ground-level test conditions and testing for both impact ice and static ice. In addition, investigations should seek to vary one factor at a time and include a focus on the individual effects of receding angle, modulus, roughness and temperature. Furthermore, all such factors listed in red in Fig. 6-1 should be characterized and reported for test results. For example, many studies fail to report surface preparation, strain rate, or ratio of force height to ice width for the push test and similarly the differences between air/sample/drop temperatures and between air speed and drop velocity are often unknown.

6.3 Conclusions

The surveyed results indicate that ice adhesion strength on surfaces measured by ground-testing can be influenced by many factors, especially for impact ice. In general, such factors vary widely between studies and some of them are not reported (as there is no widely accepted and employed standardized test procedure for evaluating icephobic surfaces). Nevertheless, several studies have tried to establish a relationship between ice adhesion strength with a few of these factors, focusing mainly on static ice. Of all the factors considered herein (e.g. Fig. 6-1), only the influence of receding angle and elastic modulus provided clear trends, that could be modeled to some degree. In particular, ice adhesion strength decreased (consistent with enhanced icephobic performance) for superhydrophobic surfaces with a high receding angle. Similarly, reduced ice adhesion strength was also observed for hydrophobic surfaces (receding contact angles between $95^{o}<\theta_{rec}<135^{o}$) which were soft (E< 6 GPa). These results were found to be true for both static and impact ice. However, dramatic variability was generally observed in the reported shear stress values. A qualitative trend of increasing adhesion strength with roughness height was found but the data was too scattered for any modeling. The effect of temperature was even less clear. This overall variability may be attributed to the fact that other parameters should be taken into account while trying to establish a robust ice adhesion strength models, and include but are not limited to the surface characteristics (thickness, temperature, thermal conductivity and surface preparation), the water characteristics (velocity, temperature, size, LWC), the air characteristics (velocity, humidity) and the testing technique (the rate and height of load application). As such, perhaps sorting the collected data, by an additional factor in cases where no trends were identified may suggest otherwise. To develop a stronger understanding of the influence of these parameters and to compare icephobic performance between studies, it is strongly recommended that guidelines or standards be developed for ground testing for both impact and static ice. Notably, beginning to follow guidelines of existing standards such as SAE ARP5905, may be an important step in moving toward repeatability in impact ice accretion and adhesion tests.

Chapter:

7 Conclusions

7.1 Atmospheric Icing Importance

The primary research goal of this project was to investigate ice adhesion strength (tensile and shear) on various surfaces for different flow conditions consistent with engine icing, representing unique work that has not been done before. Prior to the present experimental investigations, a survey was herein conducted to describe the key features of atmospheric icing pertinent to aircraft engines. This comprehensive survey was motivated by the icing of aircraft engines due to operation at low temperatures in the presence of atmospheric water. Engine ice adhesion and shedding are important since the ingestion of the shed ice can lead to detrimental effects on the engine. A few icing engine problems include engine rollback and flameout. The review first broadly discussed the environmental conditions that cause engine icing, including the atmospheric water phase (supercooled droplet vs. ice crystal icing) and the aero-thermal-fluid physics related to specific types of ice accretion (rime, glaze, etc.). Next, the engine components that are most susceptible to each type of icing and the associated engine problems (mechanical, operational, etc.) were identified.

7.2 Ice Adhesion Testing Facility

In order to accomplish the project's research goal, a novel Compact Icing Research Tunnel (CIRT) was designed and built to allow low-cost, quick turn-around, high-quality icing tests in modest volume. The CIRT was 3D printed, assembled and installed in a 1.5 m wide, 1.5 m long and 2.1 m tall walk-in cold chamber. It was also equipped with measurement capabilities to enable a thermally well-controlled environment, characterize icing test conditions, and allow ice adhesion measurements. Furthermore, this Compact Icing Research Tunnel (CIRT) was equipped with a single nozzle water spray system. The spraying system consists of a single MOD-1 nozzle calibrated to produce a droplets' cloud that has MVD range between 10 to 40 microns. The LWC with the single spray (MOD-1) in the CIRT ranges from 2 to 4 g/m^3, though all the tests conducted in this dissertation were with LWC of 2.8 g/m^3 and a droplets' cloud of 13 microns MVD, consistent with a strong icing event with supercooled liquid droplets.

7.3 Ice Tensile and Shear Adhesion Strength

The above Compact Icing Research Tunnel (CIRT) was employed to measure ice tensile and shear adhesion strength for both impact and static ice on conventional metals surfaces (aluminum & titanium) and on a Self-Lubricating Icephobic Coating (SLIC) surface. The static ice consisted of deionized water slowly poured over the surface and left to be frozen on the test specimen surface at stationary conditions. The impact ice consisted of droplets of mean volumetric diameter (MVD) of 13 μm impacting the test specimen surface respectively at velocity of 40 m/s and 35 m/s for tensile and shear tests, freezing and accreting dynamically. Both (tensile and shear) icing tests were conducted at a temperature of -20°C. The obtained results revealed that static ice has an ice tensile and shear adhesion stress higher than that of impact ice for the conditions used, consistent with previous studies. Additionally, a reduction of more than half was observed in ice tensile and shear adhesion stress for SLIC compared to aluminum and titanium for both impact and static ice. This performance of the SLIC stayed consistent even after multiple icing tests on the same sample.

7.4 Ice Adhesion Strength Trends

The ice shear adhesion data obtained in this dissertation for both impact and static ice were considered along with already published ice shear adhesion data in order to identify parametric influences and possible trends, as well as to consider existing adhesion strength models. The influence of wettability and surface modulus were the most profound. For roughness and temperature, the results indicated that parametric trends may be clear within a specific study; but, the trends are often not extendable to broad data sets of multiple investigations of static and impact ice. The dramatic variability of adhesion strength between the studies suggests that ice adhesion can depends on several parameters, which should be taken into consideration. As such, it is recommended to develop standards that govern ice adhesion tests in the future.

7.5 Contributions of Dissertation and Recommendations

This dissertation made a number of key scientific contributions. As mentioned above, this is the first study to measure both impact and static ice adhesion strength in the same facility using the same adhesion strength technique. As such, this research is unique in the sense that it provided a much better comparison of these two types of ice for a number of surfaces. Additionally, this study was the first to develop a high-fidelity compact icing tunnel. This is important, since conventional icing tunnel tests for impact ice with well-controlled conditions are typically difficult and expensive to conduct (which is a reason that there is much less data for impact ice than for static ice). Furthermore, this research was the first to characterize a robust icephobic coating (SLIC) in terms of both tensile and shear modes for the ice adhesion strength. It was also the first to examine the combined parametric influence of static and impact ice in terms of wetting, modulus of elasticity, roughness and temperatures. New recommendations are also made for future ice adhesion tests, with the goal of enabling the development of robust modeling capability for ice adhesion.

Bibliography

[1] Parent, O., and Ilinca, A. "Anti-Icing and de-Icing Techniques for Wind Turbines: Critical Review." *Cold Regions Science and Technology*, Vol. 65, No. 1, 2011, pp. 88–96. doi:10.1016/j.coldregions.2010.01.005.

[2] Yanxia, D., Yewei, G., Chunhua, X., and Xian, Y. "Investigation on Heat Transfer Characteristics of Aircraft Icing Including Runback Water." *International Journal of Heat and Mass Transfer*, Vol. 53, No. 19–20, 2010, pp. 3702–3707. doi:10.1016/j.ijheatmasstransfer.2010.04.021.

[3] Hansman, R. J., and Turnock, S. R. "Investigation of Surface Water Behavior during Glaze Ice Accretion." *Journal of Aircraft*, Vol. 26, No. 2, 1989, pp. 140–147. doi:10.2514/3.45735.

[4] Render, P. M., and Jenkinson, L. R. "Investigation into Ice Detection Parameters for Turboprop Aircraft." *Journal of Aircraft*, Vol. 33, No. 1, 1996, pp. 125–130. doi:10.2514/3.46912.

[5] Kreder, M. J., Alvarenga, J., Kim, P., and Aizenberg, J. "Design of Anti-Icing Surfaces: Smooth, Textured or Slippery?" *Nature Reviews Materials*, Vol. 1, No. 1, 2016. doi:10.1038/natrevmats.2015.3.

[6] Schutzius, T. M., Jung, S., Maitra, T., Eberle, P., Antonini, C., Stamatopoulos, C., and Poulikakos, D. "Physics of Icing and Rational Design of Surfaces with Extraordinary Icephobicity." *Langmuir*, Vol. 31, No. 17, 2015, pp. 4807–4821. doi:10.1021/la502586a.

[7] Bartlett, C. "Icing Scaling Considerations for Aircraft Engine Testing." *26th Aerospace Sciences Meeting*, AIAA Paper 88-0202, 1988. doi:10.2514/6.1988-202.

[8] Al-Khalil, K. M., Keith, T. G., Dewitt, K. J., Nathman, J. K., and Dietrich, D. A. "Thermal Analysis of Engine Inlet Anti-Icing Systems." *Journal of Propulsion and Power*, Vol. 6, No. 5, 1990, pp. 628–634. doi:10.2514/3.23264.

[9] Brown, J. M., Raghunathan, S., Watterson, J. K., Linton, A. J., and Riordon, D. "Heat Transfer Correlation for Anti-Icing Systems." *Journal of Aircraft*, Vol. 39, No. 1, 2002, pp. 65–70. doi:10.2514/2.2896.

[10] Pellissier, M. P. C., Habashi, W. G., and Pueyo, A. "Optimization via FENSAP-ICE of Aircraft Hot-Air Anti-Icing Systems." *Journal of Aircraft*, Vol. 48, No. 1, 2011, pp. 265–276. doi:10.2514/1.C031095.

[11] Potapczuk, M. G. "Aircraft Icing Research at NASA Glenn Research Center." *Journal of Aerospace Engineering*, Vol. 26, No. 2, 2013, pp. 260–276. doi:10.1061/(ASCE)AS.1943-5525.0000322.

[12] U.S. Department of Transportation, Federal Aviation Administration, "Icing Design Envelopes", *14 CFR*

parts 25 and 29, Appendix C, 2002, pp 2-4.

[13] U.S. Department of Transportation, Federal Aviation Administration, *14 CFR part 25, Appendix O*, 2004, pp 632-635.

[14] U.S. Department of Transportation, Federal Aviation Administration, *14 CFR part 33, Appendix D*, 2004, pp 909.

[15] Mason, J., Strapp, W., and Chow, P. “The Ice Particle Threat to Engines in Flight.” *44th AIAA Aerospace Sciences Meeting and Exhibit*, AIAA Paper 2006-206, 2006. doi:10.2514/6.2006-206.

[16] Mason, J. G., Chow, P., and Fuleki, D. M. “Understanding Ice Crystal Accretion and Shedding Phenomenon in Jet Engines Using a Rig Test.” *Journal of Engineering for Gas Turbines and Power*, Vol. 133, No. 4, 2011. doi:10.1115/1.4002020.

[17] Struk, P. M., Ratvasky, T. P., Bencic, T., Van Zante, J. F., King, M. C., Tsao, J.-C., and Bartkus, T. P. “An Initial Study of the Fundamentals of Ice Crystal Icing Physics in the NASA Propulsion Systems Laboratory.” *9th AIAA Atmospheric and Space Environments Conference*, AIAA Paper 2017-4242, 2017. doi:10.2514/6.2017-4242.

[18] Addy, H. E., and Veres, J. P. “An Overview of NASA Engine Ice-Crystal Icing Research.” *SAE Technical Papers*, NASA/TM-2011-217254, 2011. doi:10.4271/2011-38-0017.

[19] Haggerty, J., Defer, E., De Laat, A., Bedka, K., Moisselin, J. M., Potts, R., Delanoë, J., Parol, F., Grandin, A., and Divito, S. “Detecting Clouds Associated with Jet Engine Ice Crystal Icing.” *Bulletin of the American Meteorological Society*, Vol. 100, No. 1, 2019, pp. 29–40. doi:10.1175/BAMS-D-17-0252.1.

[20] Bravin, M., Strapp, J. W., and Mason, J. “An Investigation into Location and Convective Lifecycle Trends in an Ice Crystal Icing Engine Event Database.” *SAE Technical Papers*, 2015-01-2130, June 2015. doi:10.4271/2015-01-2130.

[21] Mason, J. G., and Grzych, M. “The Challenges Identifying Weather Associated with Jet Engine Ice Crystal Icing.” *SAE Technical Papers*, 2011-38-0094, June 2011. doi:10.4271/2011-38-0094.

[22] Nilamdeen, S., and Habashi, W. G. “Multiphase Approach toward Simulating Ice Crystal Ingestion in Jet Engines.” *Journal of Propulsion and Power*, Vol. 27, No. 5, 2011, pp. 959–969. doi:10.2514/1.B34059.

[23] Grzych, M., Tritz, T., Mason, J., Bravin, M., and Sharpsten, A. “Studies of Cloud Characteristics Related to Jet Engine Ice Crystal Icing Utilizing Infrared Satellite Imagery.” *SAE Technical Papers*, 2015-01-2086, June

2015. doi:10.4271/2015-01-2086.

[24] Hauk, T., Roisman, I. V., and Tropea, C. D. “Investigation of the Impact Behaviour of Ice Particles.” *6th AIAA Atmospheric and Space Environments Conference,* AIAA Paper 2014-3046, 2014. doi:10.2514/6.2014-3046.

[25] Pan, H., and Render, P. “Experimental Studies into the Hail Ingestion Characteristics of Turbofan Engines.” 30*th AIAA/ASME/SAE/ASEE Joint Propulsion Conference*, AIAA Paper 94-2956, 1994. doi:10.2514/6.1994-2956.

[26] Render, P. M., and Pan, H. “Experimental Studies into Hail Impact Characteristics.” *Journal of Propulsion and Power*, Vol. 11, No. 6, 1995, pp. 1224–1230. doi:10.2514/3.23961.

[27] Tsao, J. C. “Preliminary Evaluation of Altitude Scaling for Turbofan Engine Ice Crystal Icing.” *9th AIAA Atmospheric and Space Environments Conference,* AIAA Paper 2017-4086, June 2017. doi:10.2514/6.2017-4086.

[28] Currie, T. C., Struk, P. M., Tsao, J. C., Fuleki, D., and Knezevici, D. C. “Fundamental Study of Mixed-Phase Icing with Application to Ice Crystal Accretion in Aircraft Jet Engines.” *4th AIAA Atmospheric and Space Environments Conference*, AIAA Paper 2012-3035, June 2012. doi:10.2514/6.2012-3035.

[29] Sammak, M. “Anti-Icing in Gas Turbines Anti-Icing in Gas Turbines.” Master Thesis, Department of Energy Sciences, Lund University, Lund, Sweden, 2006, ISSN 0282-1990.

[30] Venkataramani, K. S., Mallina, R. V., Shamara, P. A., and Oliver, M. J. “Dynamics of Icing in Aircraft Engines.” *Collection of Technical Papers - 45th AIAA Aerospace Sciences Meeting*, AIAA Paper 2007-905, January 2007. doi:10.2514/6.2007-905.

[31] Chen, Y., Fu, L., and Dong, W. “Novel Cohesive/Adhesive Ice Shedding Model for Spinner Cone.” *Journal of Propulsion and Power*, Vol. 34, No. 3, 2018, pp. 647–659. doi:10.2514/1.B36289.

[32] Jorgenson, P. C. E., Veres, J. P., Wright, W. B., and May, R. D. “Engine Icing Modeling and Simulation (Part I): Ice Crystal Accretion on Compression System Components and Modeling Its Effects on Engine Performance.” *SAE Technical Papers*, 2011-38-0025, June 2011. doi:10.4271/2011-38-0025.

[33] Huang, X., Tepylo, N., Pommier-Budinger, V., Budinger, M., Bonaccurso, E., Villedieu, P., and Bennani, L. “A Survey of Icephobic Coatings and Their Potential Use in a Hybrid Coating/Active Ice Protection System for Aerospace Applications.” *Progress in Aerospace Sciences*, Vol. 105, No. January, 2019, pp. 74–97. doi:10.1016/j.paerosci.2019.01.002.

[34] Cao, Y., Wu, Z., Su, Y., and Xu, Z. "Aircraft Flight Characteristics in Icing Conditions." *Progress in Aerospace Sciences*, Vol. 74, 2015, pp. 62–80. doi:10.1016/j.paerosci.2014.12.001.

[35] Caliskan, F., and Hajiyev, C. "A Review of In-Flight Detection and Identification of Aircraft Icing and Reconfigurable Control." *Progress in Aerospace Sciences*, Vol. 60, 2013, pp. 12–34. doi:10.1016/j.paerosci.2012.11.001.

[36] Bragg, M. B., Broeren, A. P., and Blumenthal, L. A. "Iced-Airfoil Aerodynamics." *Progress in Aerospace Sciences*, Vol. 41, No. 5, 2005, pp. 323–362. doi:10.1016/j.paerosci.2005.07.001.

[37] Cebeci, T., and Kafyeke, F. " A Ircraft I Cing ." *Annual Review of Fluid Mechanics*, Vol. 35, No. 1, 2003, pp. 11–21. doi:10.1146/annurev.fluid.35.101101.161217.

[38] Lynch, F. T., and Khodadoust, A. "Effects of Ice Accretions on Aircraft Aerodynamics." *Progress in Aerospace Sciences*, Vol. 37, No. 8, 2001, pp. 669–767. doi:10.1016/S0376-0421(01)00018-5.

[39] Kind, R. J., Potapczuk, M. G., Feo, A., Golia, C., and Shah, A. D. "Experimental and Computational Simulation of In-Flight Icing Phenomena." *Progress in Aerospace Sciences*, Vol. 34, No. 5–6, 1998, pp. 257–345. doi:10.1016/S0376-0421(98)80001-8.

[40] Rashid, T., Khawaja, H. A., and Edvardsen, K. "Review of Marine Icing and Anti-/de-Icing Systems." *Journal of Marine Engineering and Technology*, Vol. 15, No. 2, 2016, pp. 79–87. doi:10.1080/20464177.2016.1216734.

[41] Work, A., and Lian, Y. "A Critical Review of the Measurement of Ice Adhesion to Solid Substrates." *Progress in Aerospace Sciences*, Vol. 98, No. March, 2018, pp. 1–26. doi:10.1016/j.paerosci.2018.03.001.

[42] National Transportation and Safety Board. "Aircraft Accident Report: In-Flight Icing Encounter and Loss of Control- Simmons Airlines, d.b.a. AMERICAN EAGLE FLIGHT 4184." NTSB/AAR-96/01, Washington, D.C., October 1994.

[43] Smith, K., "Turbojet, Turboprop, Turboshaft, and Turbofan Engine Induction System Icing and Ice Ingestion." *U.S. Department of Transportation - Federal Aviation Administration - Advisory Circular*, AC No. 20-147A, October 1994, retrieved September 2019. https://www.faa.gov/documentLibrary/media/Advisory_Circular/AC_20-147A.pdf.

[44] Mazzawy, R. S., and Strapp, J. W. "Appendix D - An Interim Icing Envelope." *SAE Technical Papers*, 2007-01-3311, Seville, Spain, September 2007. doi:10.4271/2007-01-3311.

[45] Van Diedenhoven, B., “Remote Sensing of Crystal Shapes in Ice Clouds.”, *Springer Series in Light Scattering*, edited A. Kokhanovsky, Chap. 5, Springer International Publishing AG 2018, pp 197-250. doi:10.1007/978-3-319-70808-9_5.

[46] Hauk, T., Bonaccurso, E., Villedieu, P., and Trontin, P. “Theoretical and Experimental Investigation of the Melting Process of Ice Particles.” *Journal of Thermophysics and Heat Transfer*, Vol. 30, No. 4, 2016, pp. 946–954. doi:10.2514/1.T4886.

[47] Leroy, D., Fontaine, E., Schwarzenboeck, A., Strapp, J. W., Korolev, A., McFarquhar, G., Dupuy, R., Gourbeyre, C., Lilie, L., Protat, A., Delanoe, J., Dezitter, F., and Grandin, A. “Ice Crystal Sizes in High Ice Water Content Clouds. Part II: Statistics of Mass Diameter Percentiles in Tropical Convection Observed during the HAIC/HIWC Project.” *Journal of Atmospheric and Oceanic Technology*, Vol. 34, No. 1, 2017, pp. 117–136. doi:10.1175/JTECH-D-15-0246.1.

[48] Lawson, R. P., Angus, L. J., and Heymsfield, A. J. “Cloud Particle Measurements in Thunderstorm Anvils and Possible Weather Threat to Aviation.” *Journal of Aircraft*, Vol. 35, No. 1, 1998, pp. 113–121. doi:10.2514/2.2268.

[49] Leroy, D., Fontaine, E., Schwarzenboeck, A., Strapp, J. W., Lilie, L., Delanoe, J., Protat, A., Dezitter, F., and Grandin, A. “HAIC/HIWC Field Campaign - Specific Findings on PSD Microphysics in High IWC Regions from in Situ Measurements: Median Mass Diameters, Particle Size Distribution Characteristics and Ice Crystal Shapes.” *SAE Technical Papers*, 2015-01-2087, June 2015. doi:10.4271/2015-01-2087.

[50] Leroy, D., Coutris, P., Fontaine, E., Schwarzenboeck, A., Walter Strapp, J., Lilie, L., Korolev, A., McFarqhuar, G., Dezitter, F., and Calmels, A. “HAIC/HIWC Field Campaigns - Specific Findings on Ice Crystals Characteristics in High Ice Water Content Cloud Regions.” *8th AIAA Atmospheric and Space Environments Conference*, AIAA Paper 2016-4056, Washington, D.C, June 2016. doi:10.2514/6.2016-4056.

[51] Bucknell, A., McGilvray, M., Gillespie, D. R. H., Jones, G., Reed, A., and Buttsworth, D. R. “Heat Transfer in the Core Compressor under Ice Crystal Icing Conditions.” *Journal of Engineering for Gas Turbines and Power*, Vol. 140, No. 7, 2018, pp. 1–13. doi:10.1115/1.4038460.

[52] Goold, I. “Rolls-Royce Advances Toward UltraFan.” *AINonline*, 2014, retrieved March 2018. https://www.ainonline.com/aviation-news/air-transport/2014-07-14/rolls-royce-advances-toward-ultrafan.

[53] Veillard, X., Habashi, W. G., and Baruzzi, G. S. “Icing Simulation in Multistage Jet Engines.” *Journal of*

Propulsion and Power, Vol. 27, No. 6, 2011, pp. 1231–1237. doi:10.2514/1.B34060.

[54] Goodwin, R. V., and Dischinger, D. G. "Turbofan Ice Crystal Rollback Investigation and Preparations Leading to Inaugural Ice Crystal Engine Test at NASA PSL-3 Test Facility. " *6th AIAA Atmospheric and Space Environments Conference*, AIAA Paper 2014-2895, June 2014. doi:10.2514/6.2014-2895.

[55] Goodwin, R. V. "Turbofan Ice Crystal Rollback Investigation and Preparations Leading to the Second, Heavily Instrumented, Ice Crystal Engine Test at NASA PSL-3 Test Facility." *8th AIAA Atmospheric and Space Environments Conference*, AIAA Paper 2016-3892, June 2016. doi:10.2514/6.2016-3892.

[56] Thomas, S. K., Cassoni, R. P., and MacArthur, C. D. "Aircraft Anti-Icing and de-Icing Techniques and Modeling." *Journal of Aircraft*, Vol. 33, No. 5, 1996, pp. 841–854. doi:10.2514/3.47027.

[57] Federal Aviation Administration Activities, Courses, Seminars & Webinars., "Structural Icing Type", ALC_Content, ALC-33: Inflight Icing, retrieved on August 2019. https://www.faasafety.gov/gslac/ALC/course_content.aspx?cID=33&sID=152&preview=true.

[58] Messinger, B. L. "Equilibrium Temperature of an Unheated Icing Surface as a Function of Air Speed." *Journal of the Aeronautical Sciences*, Vol. 20, No. 1, 1953, pp. 29–42. doi:10.2514/8.2520.

[59] Broeren, A. P., Diebold, J. M., and Bragg, M. B. "Aerodynamic Classification of Swept-Wing Ice Accretion." NASA/TM-2013-216381, DOT/FAA/TC-13/21, May 2013, 2019. doi:10.2514/6.2013-2825.

[60] Rosenfrans, W., "From Bad to Worse", Flight Safety Foundation, AeroSafety world, September 2012. https://flightsafety.org/asw-article/from-bad-to-worse/.

[61] Dong, W., Zheng, M., Zhu, J., Lei, G., and Zhao, Q. "Experimental Investigation on Anti-Icing Performance of an Engine Inlet Strut." *Journal of Propulsion and Power*, Vol. 33, No. 2, 2017, pp. 379–386. doi:10.2514/1.B36067.

[62] Lee, S., and Loth, E. "Simulation of Icing on a Cascade of Stator Blades." *Journal of Propulsion and Power*, Vol. 24, No. 6, 2008, pp. 1309–1316. doi:10.2514/1.37810.

[63] Dong, W., Zhu, J., Zheng, M., Lei, G. L., and Zhou, Z. X. "Experimental Study on Icing and Anti-Icing Characteristics of Engine Inlet Guide Vanes." *Journal of Guidance, Control, and Dynamics*, Vol. 38, No. 6, 2015, pp. 1330–1337. doi:10.2514/1.B35679.

[64] Morency, F., Brahimi, M. T., Tezok, F., and Paraschivoiu, I. "Hot Air Anti-Icing System Modelization in the ICE Prediction Code Canice." *36th AIAA Aerospace Sciences Meeting and Exhibit*, AIAA Paper 98-0192,

1998. doi:10.2514/6.1998-192.

[65] Al-Khalil, K. M., Keith, T. G., and De Witt, K. J. “New Concept in Runback Water Modeling for Anti-Iced Aircraft Surfaces.” *Journal of Aircraft*, Vol. 30, No. 1, 1993, pp. 41–49. doi:10.2514/3.56878.

[66] Al-Khalil, K. M., Keith, T. G., and De Witt, K. J. “Development of an Improved Model for Runback Water on Aircraft Surfaces.” *Journal of Aircraft*, Vol. 31, No. 2, 1994, pp. 271–278. doi:10.2514/3.46484.

[67] Calay, R. K., Holdø, A. E., Mayman, P., and Lun, I. “Experimental Simulation of Runback Ice.” *Journal of Aircraft*, Vol. 34, No. 2, 1997, pp. 206–212. doi:10.2514/2.2173.

[68] Lee, S., and Bragg, M. B. “Experimental Investigation of Simulated Large-Droplet Ice Shapes on Airfoil Aerodynamics.” *Journal of Aircraft*, Vol. 36, No. 5, 1999, pp. 844–850. doi:10.2514/2.2518.

[69] Aircraft Design for Icing - Anti-Icing Systems., “Module I - Before You Fly,” In-Flight Icing Database, retrieved August 2019. https://aircrafticing.grc.nasa.gov/1_1_3_6.html.

[70] Zhu, J., Dong, W., Zheng, M., Lei, A. G., and Zhao, Q. “Numerical Investigation of Heat and Mass Transfer on an Anti-Icing Inlet Cone.” *Journal of Propulsion and Power*, Vol. 32, No. 3, 2016, pp. 788–796. doi:10.2514/1.B35875.

[71] Dong, W., Zhu, J., Zheng, M., and Chen, Y. “Thermal Analysis and Testing of Nonrotating Cone with Hot-Air Anti-Icing System.” *Journal of Propulsion and Power*, Vol. 31, No. 3, 2015, pp. 896–903. doi:10.2514/1.B35378.

[72] Honsek, R., Habashi, W. G., and Aubé, M. S. “Eulerian Modeling of In-Flight Icing Due to Supercooled Large Droplets.” *Journal of Aircraft*, Vol. 45, No. 4, 2008, pp. 1290–1296. doi:10.2514/1.34541.

[73] Tetteh, E., Stebbins, S. J., Spivey, W., Loth, E., and Jacobs, J. “Heat Pad Effects on Inlet Guide Vane Ice Accretion.” *15th International Energy Conversion Engineering Conference*, AIAA Paper 2017-4783, Atlanta, 2017. doi:10.2514/6.2017-4783.

[74] Al-Khalil, K., Irani, E., and Miller, D. “Mixed Phase Icing Simulation and Testing at the Cox Icing Wind Tunnel.” *41st Aerospace Sciences Meeting and Exhibit*, AIAA Paper 2003-903, January 2003. doi:10.2514/6.2003-903.

[75] Kintea, D. M., Schremb, M., Roisman, I. V., and Tropea, C. “Numerical Investigation of Ice Particle Accretion on Heated Surfaces with Application to Aircraft Engines.” *AIAA AVIATION 2014 -11th AIAA/ASME Joint Thermophysics and Heat Transfer Conference*, AIAA Paper 2014-2820, June 2014. doi:10.2514/6.2014-2820.

[76] Norde, E., Van Der Weide, E. T. A., and Hoeijmakers, H. W. M. “Eulerian Method for Ice Crystal Icing.” *AIAA Journal*, Vol. 56, No. 1, 2018, pp. 222–234. doi:10.2514/1.J056184.

[77] Pan, H., and Render, P. M. “Impact Characteristics of Hailstones Simulating Ingestion by Turbofan Aeroengines.” *Journal of Propulsion and Power*, Vol. 12, No. 3, 1996, pp. 457–462. doi:10.2514/3.24057.

[78] Bartkus, T. P., Struk, P., and Tsao, J.-C. “Development of a Coupled Air and Particle Thermal Model for Engine Icing Test Facilities.” *SAE International Journal of Aerospace*, Vol. 8, No. 1, 2015, pp. 15–32. doi:10.4271/2015-01-2155.

[79] Struk, P., Currie, T., Wright, W. B., Knezevici, D. C., Fuleki, D., Broeren, A., Vargas, M., and Tsao, J. C. “Fundamental Ice Crystal Accretion Physics Studies.” *SAE Technical Papers*, NASA/TM-2012-217429, May 2012. doi:10.4271/2011-38-0018.

[80] Struk, P., Bartkus, T., Tsao, J. C., Currie, T., and Fuleki, D. “Ice Accretion Measurements on an Airfoil and Wedge in Mixed-Phase Conditions.” *SAE Technical Papers*, SAE-2015-01-2116, June 2015. doi:10.4271/2015-01-2116.

[81] Currie, T. C., Fuleki, D., and Mahallati, A. “Experimental Studies of Mixed-Phase Sticking Efficiency for Ice Crystal Accretion in Jet Engines.” *6th AIAA Atmospheric and Space Environments Conference*, AIAA Paper 2014-3049, June 2014. doi: 10.2514/6.2014-3049.

[82] Knezevici, D. C., Fuleki, D., Currie, T. C., and MacLeod, J. D. “Particle Size Effects on Ice Crystal Accretion.” *4th AIAA Atmospheric and Space Environments Conference 2012*, AIAA Paper 2012-3039, June 2012. doi:10.2514/6.2012-3039.

[83] Venkataramani, K. S., Plybon, R. C., Holm, R. G., and Krupp, B. R. “Aircraft Engine Icing Model.” *46th AIAA Aerospace Sciences Meeting and Exhibit*, AIAA Paper 2008-440, January 2008. doi:10.2514/6.2008-440.

[84] Ryosuke Hayashi, and Makoto Yamamoto. “Numerical Simulation on Ice Shedding Phenomena in Turbomachinery.” *Journal of Energy and Power Engineering*, Vol. 9, No. 1, 2015, pp. 45–53. doi:10.17265/1934-8975/2015.01.005.

[85] Labeas, G. N., Diamantakos, I. D., and Sunaric, M. M. “Simulation of the Electroimpulse De-Icing Process of Aircraft Wings.” *Journal of Aircraft*, Vol. 43, No. 6, 2006, pp. 1876–1885. doi:10.2514/1.21321.

[86] Maas, D. M., and McCown, N. M. “Turbine Inlet Ice Related Failures and Predicting Inlet Ice Formation.”

Proceedings of the ASME Turbo Expo, Vol. 4 PARTS A and B, 2007, pp. 1531–1543. doi:10.1115/GT2007-28351.

[87] May, R. D., Simon, D. L., and Guo, T. H. "Detection of the Impact of Ice Crystal Accretion in an Aircraft Engine Compression System during Dynamic Operation." *AIAA Guidance, Navigation, and Control Conference*, AIAA Paper 2014-0270, January 2014. doi:10.2514/6.2014-0270.

[88] Kundu, R., Prasad, J. V. R., Saxena, S., Singh, R., Breeze-Stringfellow, A., and Nakano, T. "Analysis of Stall Onset in a Multistage Axial Flow Compressor in Response to Engine Icing." *50th AIAA/ASME/SAE/ASEE Joint Propulsion Conference 2014*, AIAA Paper 2014-3841, July 2014. doi:10.2514/6.2014-3841.

[89] Laforte, C., Blackburn, C., and Perron, J. "A Review of Icephobic Coating Performances over the Last Decade." *SAE Technical Papers*, 2015-01-2149, June 2015. doi:10.4271/2015-01-2149.

[90] Farzaneh, M. "Ice Accretions on High-Voltage Conductors and Insulators and Related Phenomena." *Philosophical Transactions of the Royal Society of London, Series A: Mathematical, Physical and Engineering Sciences*, Vol. 358, No. 1776, 2000, pp. 2971–3005. doi:10.1098/rsta.2000.0692.

[91] Yeong, Y. H., Milionis, A., Loth, E., and Sokhey, J. "Self-Lubricating Icephobic Elastomer Coating (SLIC) for Ultralow Ice Adhesion with Enhanced Durability." *Cold Regions Science and Technology*, Vol. 148, No. June 2017, 2018, pp. 29–37. doi:10.1016/j.coldregions.2018.01.005.

[92] Jasinski, W. J., Noe, S. C., Selig, M. S., and Bragg, M. B. "Wind Turbine Performance under Icing Conditions." *Journal of Solar Energy Engineering*, Vol. 120, No. 1, 1998, pp. 60–65. doi:10.1115/1.2888048.

[93] Dalili, N., Edrisy, A., and Carriveau, R. "A Review of Surface Engineering Issues Critical to Wind Turbine Performance." *Renewable and Sustainable Energy Reviews*, Vol. 13, No. 2, 2009, pp. 428–438. doi:10.1016/j.rser.2007.11.009.

[94] Homola, M. C., Nicklasson, P. J., and Sundsbø, P. A. "Ice Sensors for Wind Turbines." *Cold Regions Science and Technology*, Vol. 46, No. 2, 2006, pp. 125–131. doi:10.1016/j.coldregions.2006.06.005.

[95] Bansmer, S. E., Baumert, A., Sattler, S., Knop, I., Leroy, D., Schwarzenboeck, A., Jurkat-Witschas, T., Voigt, C., Pervier, H., and Esposito, B. "Design, Construction and Commissioning of the Braunschweig Icing Wind Tunnel." *Atmospheric Measurement Techniques*, Vol. 11, No. 6, 2018, pp. 3221–3249. doi:10.5194/amt-11-3221-2018.

[96] Gent, R. W., Dart, N. P., and Cansdale, J. T. "Aircraft Icing." *Philosophical Transactions of the Royal Society*

of London, Series A: Mathematical, Physical and Engineering Sciences, Vol. 358, No. 1776, 2000, pp. 2873–2911. doi:10.1098/rsta.2000.0689.

[97] Janjua, Z. A. “The Influence of Freezing and Ambient Temperature on the Adhesion Strength of Ice.” *Cold Regions Science and Technology*, Vol. 140, No. May, 2017, pp. 14–19. doi:10.1016/j.coldregions.2017.05.001.

[98] Wang, X., Naterer, G. F., and Bibeau, E. “Convective Droplet Impact and Heat Transfer from a NACA Airfoil.” *Journal of Thermophysics and Heat Transfer*, Vol. 21, No. 3, 2007, pp. 536–542. doi:10.2514/1.27850.

[99] Wang, X., Naterete, G. F., and Bibeau, E. “Convective Heat Transfer from a NACA Airfoil at Varying Angles of Attack.” *Journal of Thermophysics and Heat Transfer*, Vol. 22, No. 3, 2008, pp. 457–463. doi:10.2514/1.34405.

[100] Jin, Z., and Hu, H. “Icing Process of Small Water Droplets Impinging onto a Frozen Cold Plate.” *Journal of Thermophysics and Heat Transfer*, Vol. 24, No. 4, 2010, pp. 841–844. doi:10.2514/1.49606.

[101] Henry, R. C., Guffond, D., Garnier, F., and Bouveret, A. “Heat Transfer Coefficient Measurement on Iced Airfoil in a Small Icing Wind Tunnel.” *Journal of Thermophysics and Heat Transfer*, Vol. 14, No. 3, 2000, pp. 348–354. doi:10.2514/6.1999-372.

[102] Lou, D., Hammond, D., and Pervier, M. L. “Investigation of the Adhesive Properties of the Ice-Aluminum Interface.” *Journal of Aircraft*, Vol. 51, No. 3, 2014, pp. 1051–1055. doi:10.2514/1.C032509.

[103] Guerin, F., Laforte, C., Farinas, M. I., and Perron, J. “Analytical Model Based on Experimental Data of Centrifuge Ice Adhesion Tests with Different Substrates.” *Cold Regions Science and Technology*, Vol. 121, 2016, pp. 93–99. doi:10.1016/j.coldregions.2015.10.011.

[104] Reinmann, J., Shaw, R. J., and Olsen, W. A. “NASA Lewis Research Center ’ s Program on Icing Research Cleveland”, *AIAA 21st Aerospace Sciences Meeting*, AIAA Paper 1983-0204, 1983. doi:10.2514/6.1983-204.

[105] John Hansman, R., Yamaguchi, K., Berkowitz, B., and Potapczuk, M. “Modeling of Surface Roughness Effects on Glaze Ice Accretion.” *Journal of Thermophysics and Heat Transfer*, Vol. 5, No. 1, 1991, pp. 54–60. doi:10.2514/3.226.

[106] Ide, R. F., and Oldenburg, J. R. “Icing Cloud Calibration of the NASA Glenn Icing Research Tunnel”, *39th Aerospace Sciences Meeting & Exhibit*, AIAA Paper 2001-0234, 2001. doi:10.2514/6.2001-234.

[107] Steen, L. E., Ide, R. F., and Van Zante, J. F. “An Assessment of the Icing Blade and the SEA Multi-Element Sensor for Liquid Water Content Calibration of the NASA GRC Icing Research Tunnel.” *8th AIAA Atmospheric and Space Environments Conference*, AIAA Paper 2016-4051, 2016. doi:10.2514/6.2016-4051.

[108] Hammond, D., and Luxford, G. “Cranfield University Icing Wind Tunnel.”, *41st Aerospace Sciences Meeting and Exhibit*, AIAA Paper 2003-901, 2003. doi:10.2514/6.2003-901.

[109] Lou, D. “The Development Production Demonstration and Analysis of the Ice Shear Rig for the Study of Engine Icing.” *MSc thesis*, School of Engineering, Cranfield University, U.K., 2010.

[110] Tetteh, E., and Loth, E. “Reducing Static and Impact Ice Adhesion with a Self-Lubricating Icephobic Coating (SLIC).” *Coatings*, Vol. 10, No. 3, 2020, p. 262. doi:10.3390/coatings10030262.

[111] Barlow, J. B., H. Rae, W., and Pope, A. *Low-Speed Wind Tunnel Testing, 3rd Edition* -. 1999.

[112] Davis, A. “Superhydrophobic Surfaces to Resist Droplet Sprays, Simulated Rain, Water Jets, and Aerodynamic Icing.” *MSc thesis*, Department of Mechanical and Aerospace Engineering, University of Virginia, U.S.A., 2013.

[113] Davis, A., Yeong, Y. H., Steele, A., Loth, E., and Bayer, I. S. “Spray Impact Resistance of a Superhydrophobic Nanocomposite Coating.” *AIChE Journal*, Vol. 60, No. 8, 2014, pp. 3025–3032. doi:10.1002/aic.

[114] SAE ARP5905 (TM). *Calibration and Acceptance of Icing Wind Tunnels*. 2015.

[115] Andrews, E. H., and Stevenson, A. “Fracture Energy of Epoxy Resin under Plane Strain Conditions.” *Journal of Materials Science*, Vol. 13, No. 8, 1978, pp. 1680–1688. doi:10.1007/BF00548731.

[116] Andrews, E. H., and Lockington, N. A. “The Cohesive and Adhesive Strength of Ice.” *Journal of Materials Science*, Vol. 18, No. 5, 1983, pp. 1455–1465. doi:10.1007/BF01111965.

[117] Andrews, E. H., Majid, H. A., and Lockington, N. A. “Adhesion of Ice to a Flexible Substrate.” *Journal of Materials Science*, Vol. 19, No. 1, 1984, pp. 73–81. doi:10.1007/BF02403112.

[118] Pervier, M.-L. “Mechanics of Ice Detachment Applied To Turbomachinery.” *PhD thesis*, Department of Power and Propulsion, Cranfield University, U.K., 2012.

[119] Yeong, Y. H. “Impinging Drops on Superhydrophobic Surfaces at Icing Conditions.” *PhD thesis*, Department of Mechanical and Aerospace Engineering, University of Virginia, U.S.A., 2014. doi:10.18130/V34V6F.

[120] Yeong, Y. H., Milionis, A., Loth, E., Sokhey, J., and Lambourne, A. “Atmospheric Ice Adhesion on Water-Repellent Coatings: Wetting and Surface Topology Effects.” *Langmuir*, Vol. 31, No. 48, 2015, pp. 13107–

13116. doi:10.1021/acs.langmuir.5b02725.

[121] Yeong, Y. H., Loth, E., and Sokhey, J. Ice Adhesion on Superhydrophobic Coatings in a Icing Wind Tunnel. In *Adv. Polym. Sci*, Springer, Berlin, Heidelberg, Berlin.

[122] Tetteh, E. Y., Loth, E., Loebig, J., Cummings, J., and Lilly, N. "The Compact Icing Research Tunnel (CIRT)." *AIAA Propulsion & Energy Forum,* AIAA paper 2019-4002, August 2019. doi:10.2514/6.2019-4002.

[123] Tremblay, C. "Determination de la Resistance a la Traction de la Glace Atmospherique. " *MSc thesis*, Resources and Systems Department, Université du Québec à Chicoutimi, Canada, 1991.

[124] Druez, J., Cloutier, J., and Claveau, L. "Etude Comparative de la Resistance a la Traction et a la Compression de la Glace Atmospherique." *Le Journal de Physique Colloques*, Vol. 48, No. C1, 1987, pp. C1-337-C1-343. doi:10.1051/jphyscol:1987147.

[125] Druez, J., McComber, P., and Tremblay, C. "Experimental Results on the Tensile Strength of Atmospheric Ice." *Transactions of the Canadian Society for Mechanical Engineering*, Vol. 13, No. 3, 1989, pp. 59–64. doi:10.1139/tcsme-1989-0010.

[126] Chu, M., Scavuzzo, R., and Kellackey, C. "Tensile Properties of Impact Ices." *30th Aerospace Sciences Meeting and Exhibit*, AIAA Paper 1992-0883, 1992. doi:10.2514/6.1992-883.

[127] Yirtici, O., Tuncer, I. H., and Ozgen, S. "Ice Accretion Prediction on Wind Turbines and Consequent Power Losses." *Journal of Physics: Conference Series*, Vol. 753, No. 2, 2016. doi:10.1088/1742-6596/753/2/022022.

[128] Antonini, C., Innocenti, M., Horn, T., Marengo, M., and Amirfazli, A. "Understanding the Effect of Superhydrophobic Coatings on Energy Reduction in Anti-Icing Systems." *Cold Regions Science and Technology*, Vol. 67, No. 1–2, 2011, pp. 58–67. doi:10.1016/j.coldregions.2011.02.006.

[129] Liu, Y., Li, L., Li, H., and Hu, H. "An Experimental Study of Surface Wettability Effects on Dynamic Ice Accretion Process over an UAS Propeller Model." *Aerospace Science and Technology*, Vol. 73, 2018, pp. 164–172. doi:10.1016/j.ast.2017.12.003.

[130] Zheng, S., Li, C., Fu, Q., Hu, W., Xiang, T., Wang, Q., Du, M., Liu, X., and Chen, Z. "Development of Stable Superhydrophobic Coatings on Aluminum Surface for Corrosion-Resistant, Self-Cleaning, and Anti-Icing Applications." *Materials and Design*, Vol. 93, 2016, pp. 261–270. doi:10.1016/j.matdes.2015.12.155.

[131] Susoff, M., Siegmann, K., Pfaffenroth, C., and Hirayama, M. "Evaluation of Icephobic Coatings - Screening of Different Coatings and Influence of Roughness." *Applied Surface Science*, Vol. 282, 2013, pp. 870–879.

doi:10.1016/j.apsusc.2013.06.073.

[132] Boinovich, L. B., and Emelyanenko, A. M. "Anti-Icing Potential of Superhydrophobic Coatings." *Mendeleev Commun*, Vol. 23, 2013, pp. 3–10. doi:10.1016/j.mencom.2013.

[133] Cao, L., Jones, A. K., Sikka, V. K., Wu, J., and Gao, D. "Anti-Icing Superhydrophobic Coatings." *Langmuir*, Vol. 25, No. 21, 2009, pp. 12444–12448. doi:10.1021/la902882b.

[134] Chavan, S., Carpenter, J., Nallapaneni, M., Chen, J. Y., and Miljkovic, N. "Bulk Water Freezing Dynamics on Superhydrophobic Surfaces." *Applied Physics Letters*, Vol. 110, No. 4, 2017. doi:10.1063/1.4974296.

[135] Chavan, S., Park, D., Singla, N., Sokalski, P., Boyina, K., and Miljkovic, N. "Effect of Latent Heat Released by Freezing Droplets during Frost Wave Propagation." *Langmuir*, Vol. 34, No. 22, 2018, pp. 6636–6644. doi:10.1021/acs.langmuir.8b00916.

[136] De Koninck, L. H., Ahmadi, S. F., and Boreyko, J. B. "Passive Anti-Frosting Cables." *International Journal of Heat and Mass Transfer*, Vol. 146, 2020, p. 118808. doi:10.1016/j.ijheatmasstransfer.2019.118808.

[137] Esmeryan, K. D., Bressler, A. H., Castano, C. E., Fergusson, C. P., and Mohammadi, R. "Rational Strategy for the Atmospheric Icing Prevention Based on Chemically Functionalized Carbon Soot Coatings." *Applied Surface Science*, Vol. 390, 2016, pp. 452–460. doi:10.1016/j.apsusc.2016.08.101.

[138] Esmeryan, K. D., Castano, C. E., Mohammadi, R., Lazarov, Y., and Radeva, E. I. "Delayed Condensation and Frost Formation on Superhydrophobic Carbon Soot Coatings by Controlling the Presence of Hydrophilic Active Sites." *Journal of Physics D: Applied Physics*, Vol. 51, No. 5, 2018. doi:10.1088/1361-6463/aaa188.

[139] Farhadi, S., Farzaneh, M., and Kulinich, S. A. "Anti-Icing Performance of Superhydrophobic Surfaces." *Applied Surface Science*, Vol. 257, No. 14, 2011, pp. 6264–6269. doi:10.1016/j.apsusc.2011.02.057.

[140] Wang, N., Xiong, D., Deng, Y., Shi, Y., and Wang, K. "Mechanically Robust Superhydrophobic Steel Surface with Anti-Icing, UV-Durability, and Corrosion Resistance Properties." *ACS Applied Materials and Interfaces*, Vol. 7, No. 11, 2015, pp. 6260–6272. doi:10.1021/acsami.5b00558.

[141] Verho, T., Bower, C., Andrew, P., Franssila, S., Ikkala, O., and Ras, R. H. A. "Mechanically Durable Superhydrophobic Surfaces." *Advanced Materials*, Vol. 23, No. 5, 2011, pp. 673–678. doi:10.1002/adma.201003129.

[142] Ellinas, K., Tserepi, A., and Gogolides, E. "Durable Superhydrophobic and Superamphiphobic Polymeric Surfaces and Their Applications: A Review." *Advances in Colloid and Interface Science*, Vol. 250, 2017, pp.

132–157. doi:10.1016/j.cis.2017.09.003.

[143] Balordi, M., Cammi, A., Santucci de Magistris, G., and Chemelli, C. “Role of Micrometric Roughness on Anti-Ice Properties and Durability of Hierarchical Super-Hydrophobic Aluminum Surfaces.” *Surface and Coatings Technology*, Vol. 374, No. March, 2019, pp. 549–556. doi:10.1016/j.surfcoat.2019.06.001.

[144] Boinovich, L. B., Emelyanenko, A. M., Ivanov, V. K., and Pashinin, A. S. “Durable Icephobic Coating for Stainless Steel.” *ACS Applied Materials and Interfaces*, Vol. 5, No. 7, 2013, pp. 2549–2554. doi:10.1021/am3031272.

[145] Song, J., Zhao, D., Han, Z., Xu, W., Lu, Y., Liu, X., Liu, B., Carmalt, C. J., Deng, X., and Parkin, I. P. “Super-Robust Superhydrophobic Concrete.” *Journal of Materials Chemistry A*, Vol. 5, No. 28, 2017, pp. 14542–14550. doi:10.1039/c7ta03526h.

[146] Kulinich, S. A., Farhadi, S., Nose, K., and Du, X. W. “Superhydrophobic Surfaces: Are They Really Ice-Repellent?” *Langmuir*, Vol. 27, No. 1, 2011, pp. 25–29. doi:10.1021/la104277q.

[147] Kim, P., Wong, T. S., Alvarenga, J., Kreder, M. J., Adorno-Martinez, W. E., and Aizenberg, J. “Liquid-Infused Nanostructured Surfaces with Extreme Anti-Ice and Anti-Frost Performance.” *ACS Nano*, Vol. 6, No. 8, 2012, pp. 6569–6577. doi:10.1021/nn302310q.

[148] Esmeryan, K. D. “From Extremely Water-Repellent Coatings to Passive Icing Protection—Principles, Limitations and Innovative Application Aspects.” *Coatings*, Vol. 10, No. 1, 2020, p. 66. doi:10.3390/coatings10010066.

[149] Maitra, T., Jung, S., Giger, M. E., Kandrical, V., Ruesch, T., and Poulikakos, D. “Superhydrophobicity vs. Ice Adhesion: The Quandary of Robust Icephobic Surface Design.” *Advanced Materials Interfaces*, Vol. 2, No. 16, 2015. doi:10.1002/admi.201500330.

[150] Jung, S., Dorrestijn, M., Raps, D., Das, A., Megaridis, C. M., and Poulikakos, D. “Are Superhydrophobic Surfaces Best for Icephobicity?” *Langmuir*, Vol. 27, No. 6, 2011, pp. 3059–3066. doi:10.1021/la104762g.

[151] Wier, K. A., and McCarthy, T. J. “Condensation on Ultrahydrophobic Surfaces and Its Effect on Droplet Mobility: Ultrahydrophobic Surfaces Are Not Always Water Repellant.” *Langmuir*, Vol. 22, No. 6, 2006, pp. 2433–2436. doi:10.1021/la0525877.

[152] Wilson, P. W., Lu, W., Xu, H., Kim, P., Kreder, M. J., Alvarenga, J., and Aizenberg, J. “Inhibition of Ice Nucleation by Slippery Liquid-Infused Porous Surfaces (SLIPS).” *Physical Chemistry Chemical Physics*, Vol.

15, No. 2, 2013, pp. 581–585. doi:10.1039/c2cp43586a.

[153] Smith, J. D., Dhiman, R., Anand, S., Reza-Garduno, E., Cohen, R. E., McKinley, G. H., and Varanasi, K. K. "Droplet Mobility on Lubricant-Impregnated Surfaces." *Soft Matter*, Vol. 9, No. 6, 2013, pp. 1772–1780. doi:10.1039/c2sm27032c.

[154] Subramanyam, S. B., Rykaczewski, K., and Varanasi, K. K. "Ice Adhesion on Lubricant-Impregnated Textured Surfaces." *Langmuir*, Vol. 29, No. 44, 2013, pp. 13414–13418. doi:10.1021/la402456c.

[155] Ozbay, S., Yuceel, C., and Erbil, H. Y. "Improved Icephobic Properties on Surfaces with a Hydrophilic Lubricating Liquid." *ACS Applied Materials and Interfaces*, Vol. 7, No. 39, 2015, pp. 22067–22077. doi:10.1021/acsami.5b07265.

[156] Rykaczewski, K., Anand, S., Subramanyam, S. B., and Varanasi, K. K. "Mechanism of Frost Formation on Lubricant-Impregnated Surfaces." *Langmuir*, Vol. 29, No. 17, 2013, pp. 5230–5238. doi:10.1021/la400801s.

[157] Wong, T. S., Kang, S. H., Tang, S. K. Y., Smythe, E. J., Hatton, B. D., Grinthal, A., and Aizenberg, J. "Bioinspired Self-Repairing Slippery Surfaces with Pressure-Stable Omniphobicity." *Nature*, Vol. 477, No. 7365, 2011, pp. 443–447. doi:10.1038/nature10447.

[158] Wang, G., and Guo, Z. "Liquid Infused Surfaces with Anti-Icing Properties." *Nanoscale*, Vol. 11, No. 47, 2019, pp. 22615–22635. doi:10.1039/c9nr06934h.

[159] Erbil, H. Y. "Improvement of Lubricant-Infused Surfaces for Anti-Icing Applications." *Surface Innovations*, Vol. 4, No. 4, 2016, pp. 214–217. doi:10.1680/jsuin.16.00026.

[160] Zhang, M., Yu, J., Chen, R., Liu, Q., Liu, J., Song, D., Liu, P., Gao, L., and Wang, J. "Highly Transparent and Robust Slippery Lubricant-Infused Porous Surfaces with Anti-Icing and Anti-Fouling Performances." *Journal of Alloys and Compounds*, Vol. 803, 2019, pp. 51–60. doi:10.1016/j.jallcom.2019.06.241.

[161] Zhu, L., Xue, J., Wang, Y., Chen, Q., Ding, J., and Wang, Q. "Ice-Phobic Coatings Based on Silicon-Oil-Infused Polydimethylsiloxane." *ACS Applied Materials and Interfaces*, Vol. 5, No. 10, 2013, pp. 4053–4062. doi:10.1021/am400704z.

[162] Wang, Y., Yao, X., Chen, J., He, Z., Liu, J., Li, Q., Wang, J., and Jiang, L. "Organogel as Durable Anti-Icing Coatings." *Science China Materials*, Vol. 58, No. 7, 2015, pp. 559–565. doi:10.1007/s40843-015-0069-7.

[163] Urata, C., Dunderdale, G. J., England, M. W., and Hozumi, A. "Self-Lubricating Organogels (SLUGs) with Exceptional Syneresis-Induced Anti-Sticking Properties against Viscous Emulsions and Ices." *Journal of*

Materials Chemistry A, Vol. 3, No. 24, 2015, pp. 12626–12630. doi:10.1039/c5ta02690c.

[164] Liu, H., Zhang, P., Liu, M., Wang, S., and Jiang, L. “Organogel-Based Thin Films for Self-Cleaning on Various Surfaces.” *Advanced Materials*, Vol. 25, No. 32, 2013, pp. 4477–4481. doi:10.1002/adma.201301289.

[165] Eifert, A., Paulssen, D., Varanakkottu, S. N., Baier, T., and Hardt, S. “Simple Fabrication of Robust Water-Repellent Surfaces with Low Contact-Angle Hysteresis Based on Impregnation.” *Advanced Materials Interfaces*, Vol. 1, No. 3, 2014, pp. 1–5. doi:10.1002/admi.201300138.

[166] Damle, V. G., Uppal, A., Sun, X., Burgin, T. P., and Rykaczewski, K. “Rapid and Scalable Lubrication and Replenishment of Liquidinfused Materials.” *Surface Innovations*, Vol. 4, No. 2, 2015, pp. 102–108. doi:10.1680/jsuin.16.00002.

[167] Zhuo, Y., Håkonsen, V., He, Z., Xiao, S., He, J., and Zhang, Z. “Enhancing the Mechanical Durability of Icephobic Surfaces by Introducing Autonomous Self-Healing Function.” *ACS Applied Materials and Interfaces*, Vol. 10, No. 14, 2018, pp. 11972–11978. doi:10.1021/acsami.8b01866.

[168] Golovin, K., Kobaku, S. P. R., Lee, D. H., DiLoreto, E. T., Mabry, J. M., and Tuteja, A. “Designing Durable Icephobic Surfaces.” *Science Advances*, Vol. 2, No. 3, 2016. doi:10.1126/sciadv.1501496.

[169] Acker, L. W. *Preliminary Results of Natural Icing of an Axial-Flow Turbojet Engine*. Washington, 1948.

[170] Tetteh, E. Y., Loth, E., Loebig, J., Cummings, J., and Lilly, N. “The Compact Icing Research Tunnel (CIRT).” *AIAA Propulsion & Energy Forum,* AIAA paper 2019-4002, August 2019. doi:10.2514/6.2019-4002.

[171] Meuler, A. J., Smith, J. D., Varanasi, K. K., Mabry, J. M., McKinley, G. H., and Cohen, R. E. “Relationships between Water Wettability and Ice Adhesion.” *ACS Applied Materials and Interfaces*, Vol. 2, No. 11, 2010, pp. 3100–3110. doi:10.1021/am1006035.

[172] Rothrock, A. M., and Selden, R. F. *Adhesion of Ice in Its Relation to the De-Icing of Airplanes*; NACA Technical Notes, Washington, DC, USA, August 1939.

[173] Milionis, A., Loth, E., and Bayer, I. S. “Recent Advances in the Mechanical Durability of Superhydrophobic Materials.” *Advances in Colloid and Interface Science*, Vol. 229, 2016, pp. 57–79. doi:10.1016/j.cis.2015.12.007.

[174] Cho, S. H., White, S. R., and Braun, P. V. “Self-Healing Polymer Coatings.” *Advanced Materials*, Vol. 21, No. 6, 2009, pp. 645–649. doi:10.1002/adma.200802008.

[175] Zhuo, Y., Xiao, S., Håkonsen, V., Li, T., Wang, F., He, J., and Zhang, Z. "Ultrafast Self-Healing and Highly Transparent Coating with Mechanically Durable Icephobicity." *Applied Materials Today*, Vol. 19, 2020, p. 100542. doi:10.1016/j.apmt.2019.100542.

[176] Rønneberg, S., Zhuo, Y., Laforte, C., He, J., and Zhang, Z. "Interlaboratory Study of Ice Adhesion Using Different Techniques." *Coatings*, Vol. 9, No. 10, 2019, p. 678. doi:10.3390/coatings9100678.

[177] Vasileiou, T., Schutzius, T. M., and Poulikakos, D. "Imparting Icephobicity with Substrate Flexibility." *Langmuir*, Vol. 33, No. 27, 2017, pp. 6708–6718. doi:10.1021/acs.langmuir.7b01412.

[178] Irajizad, P., Al-Bayati, A., Eslami, B., Shafquat, T., Nazari, M., Jafari, P., Kashyap, V., Masoudi, A., Araya, D., and Ghasemi, H. "Stress-Localized Durable Icephobic Surfaces." *Materials Horizons*, Vol. 6, No. 4, 2019, pp. 758–766. doi:10.1039/c8mh01291a.

[179] Irajizad, P., Hasnain, M., Farokhnia, N., Sajadi, S. M., and Ghasemi, H. "Magnetic Slippery Extreme Icephobic Surfaces." *Nature Communications*, Vol. 7, No. December, 2016, pp. 1–7. doi:10.1038/ncomms13395.

[180] Oleskiw, M. M. "A Review of 65 Years of Aircraft In-Flight Icing Research at NRC." *Canadian Aeronautics and Space Journal*, Vol. 47, No. 3, 2001, pp. 259–268.

[181] Lian, W., and Xuan, Y. "Experimental Investigation on a Novel Aero-Engine Nose Cone Anti-Icing System." *Applied Thermal Engineering*, Vol. 121, 2017, pp. 1011–1021. doi:10.1016/j.applthermaleng.2017.04.160.

[182] Ozbay, S., and Erbil, H. Y. "Ice Accretion by Spraying Supercooled Droplets Is Not Dependent on Wettability and Surface Free Energy of Substrates." *Colloids and Surfaces A: Physicochemical and Engineering Aspects*, Vol. 504, 2016, pp. 210–218. doi:10.1016/j.colsurfa.2016.05.065.

[183] Chen, J., Liu, J., He, M., Li, K., Cui, D., Zhang, Q., Zeng, X., Zhang, Y., Wang, J., and Song, Y. "Superhydrophobic Surfaces Cannot Reduce Ice Adhesion." *Applied Physics Letters*, Vol. 101, No. 11, 2012, pp. 2012–2015. doi:10.1063/1.4752436.

[184] Smith, J. D., Meuler, A. J., Bralower, H. L., Venkatesan, R., Subramanian, S., Cohen, R. E., McKinley, G. H., and Varanasi, K. K. "Hydrate-Phobic Surfaces: Fundamental Studies in Clathrate Hydrate Adhesion Reduction." *Physical Chemistry Chemical Physics*, Vol. 14, No. 17, 2012, pp. 6013–6020. doi:10.1039/c2cp40581d.

[185] He, Z., Vågenes, E. T., Delabahan, C., He, J., and Zhang, Z. "Room Temperature Characteristics of Polymer-

Based Low Ice Adhesion Surfaces.” *Scientific Reports*, Vol. 7, 2017, pp. 1–10. doi:10.1038/srep42181.

[186] Beeram, P., Waldman, R., and Hu, H. “Ice Adhesion Measurements of Ice Mitigation Coatings Pertinent to Aircraft Icing.” *9th AIAA Atmospheric and Space Environments Conference, 2017*, No. June, 2017, pp. 1–15. doi:10.2514/6.2017-3928.

[187] Wang, C., Zhang, W., Siva, A., Tiea, D., and Wynne, K. J. “Laboratory Test for Ice Adhesion Strength Using Commercial Instrumentation.” *Langmuir*, Vol. 30, No. 2, 2014, pp. 540–547. doi:10.1021/la4044254.

[188] Makkonen, L. “Ice Adhesion - Theory, Measurements and Countermeasures.” *Journal of Adhesion Science and Technology*, Vol. 26, No. 4–5, 2012, pp. 413–445. doi:10.1163/016942411X574583.

[189] Varanasi, K. K., Deng, T., Smith, J. D., Hsu, M., and Bhate, N. “Frost Formation and Ice Adhesion on Superhydrophobic Surfaces.” *Applied Physics Letters*, Vol. 97, No. 23, 2010, pp. 95–98. doi:10.1063/1.3524513.

[190] Fu, Q., Wu, X., Kumar, D., Ho, J. W. C., Kanhere, P. D., Srikanth, N., Liu, E., Wilson, P., and Chen, Z. “Development of Sol-Gel Icephobic Coatings: Effect of Surface Roughness and Surface Energy.” *ACS Applied Materials and Interfaces*, Vol. 6, No. 23, 2014, pp. 20685–20692. doi:10.1021/am504348x.

[191] Laforte, C., and Beisswenger, A. “Icephobic Material Centrifuge Adhesion Test.” *Proceedings of the International Workshop on Atmospheric Icing of Structures (IWAIS XI)*, No. June, 2005, pp. 1–5.

[192] Menini, R., and Farzaneh, M. “Elaboration of Al2O3/PTFE Icephobic Coatings for Protecting Aluminum Surfaces.” *Surface and Coatings Technology*, Vol. 203, No. 14, 2009, pp. 1941–1946. doi:10.1016/j.surfcoat.2009.01.030.

[193] Menini, R., Ghalmi, Z., and Farzaneh, M. “Highly Resistant Icephobic Coatings on Aluminum Alloys.” *Cold Regions Science and Technology*, Vol. 65, No. 1, 2011, pp. 65–69. doi:10.1016/j.coldregions.2010.03.004.

[194] Dotan, A., Dodiuk, H., Laforte, C., and Kenig, S. “The Relationship between Water Wetting and Ice Adhesion.” *Journal of Adhesion Science and Technology*, Vol. 23, No. 15, 2009, pp. 1907–1915. doi:10.1163/016942409X12510925843078.

[195] Kulinich, S. A., and Farzaneh, M. “On Ice-Releasing Properties of Rough Hydrophobic Coatings.” *Cold Regions Science and Technology*, Vol. 65, No. 1, 2011, pp. 60–64. doi:10.1016/j.coldregions.2010.01.001.

[196] Kulinich, S. A., and Farzaneh, M. “Ice Adhesion on Super-Hydrophobic Surfaces.” *Applied Surface Science*, Vol. 255, No. 18, 2009, pp. 8153–8157. doi:10.1016/j.apsusc.2009.05.033.

[197] Kulinich, S. A., and Farzaneh, M. “How Wetting Hysteresis Influences Ice Adhesion Strength on Superhydrophobic Surfaces.” *Langmuir*, Vol. 25, No. 16, 2009, pp. 8854–8856. doi:10.1021/la901439c.

[198] Janjua, Z. A., Turnbull, B., Choy, K. L., Pandis, C., Liu, J., Hou, X., and Choi, K. S. “Performance and Durability Tests of Smart Icephobic Coatings to Reduce Ice Adhesion.” *Applied Surface Science*, Vol. 407, 2017, pp. 555–564. doi:10.1016/j.apsusc.2017.02.206.

[199] Arianpour, F., Farzaneh, M., and Jafari, R. “Hydrophobic and Ice-Phobic Properties of Self-Assembled Monolayers (SAMs) Coatings on AA6061.” *Progress in Organic Coatings*, Vol. 93, 2016, pp. 41–45. doi:10.1016/j.porgcoat.2015.12.008.

[200] Chu, M. C., and Scavuzzo, R. J. “Adhesive Shear Strength of Impact Ice.” *AIAA Journal*, Vol. 29, No. 11, 1991, pp. 1921–1926. doi:10.2514/3.10819.

[201] Mulherin, N. D., and Haehnel, R. B. “Ice Engineering: Progress in Evaluating Surface Coatings for Icing Control at Corps Hydraulic Structures.” *Cold Regions Research and Engineering Laboratory Technical Note*, Vol. 03, No. 4, 2003, pp. 1–8.

[202] Tepylo, N., Huang, X., Budinger, M., Pommier-Budinger, V., and Rouset, P. “Evaluation Of Anti-Icing Polymer Coatings.” *Proceedings of the Canadian Society for Mechanical Engineering International Congress 2018 (CSME Internation Congress 2018)*, May, 2018, pp. 1–5. doi:10.25071/10315/35417.

[203] Rivero, P. J., Rodriguez, R. J., Larumbe, S., Monteserín, M., Martín, F., García, A., Acosta, C., Clemente, M. J., García, P., Mora, J., and Agüero, A. “Evaluation of Functionalized Coatings for the Prevention of Ice Accretion by Using Icing Wind Tunnel Tests.” *Coatings*, Vol. 10, No. 7, 2020, p. 636. doi:10.3390/coatings10070636.

[204] Fortin, G., and Perron, J. “Ice Adhesion Models to Predict Shear Stress at Shedding.” *Journal of Adhesion Science and Technology*, Vol. 26, No. 4–5, 2012, pp. 523–553. doi:10.1163/016942411X574835.

[205] Rønneberg, S., Laforte, C., Volat, C., He, J., and Zhang, Z. “The Effect of Ice Type on Ice Adhesion.” *AIP Advances*, Vol. 9, No. 5, 2019. doi:10.1063/1.5086242.

[206] Menini, R., and Farzaneh, M. “Advanced Icephobic Coatings.” *Journal of Adhesion Science and Technology*, Vol. 25, No. 9, 2011, pp. 971–992. doi:10.1163/016942410X533372.

[207] Zhuo, Y., Håkonsen, V., He, Z., Xiao, S., He, J., and Zhang, Z. “Enhancing the Mechanical Durability of Icephobic Surfaces by Introducing Autonomous Self-Healing Function.” *ACS Applied Materials & Interfaces*,

Vol. 10, No. 14, 2018, pp. 11972–11978. doi:10.1021/acsami.8b01866.

[208] Golovin, K., and Tuteja, A. “A Predictive Framework for the Design and Fabrication of Icephobic Polymers.” *Science Advances*, Vol. 3, No. 9, 2017, pp. 1–10. doi:10.1126/sciadv.1701617.

[209] Pervier, M. L. A., Gurrutxaga Lerma, B., Piles Moncholi, E., and Hammond, D. W. “A New Test Apparatus to Measure the Adhesive Shear Strength of Impact Ice on Titanium 6Al-4V Alloy.” *Engineering Fracture Mechanics*, Vol. 214, No. February, 2019, pp. 212–222. doi:10.1016/j.engfracmech.2019.01.039.

[210] SAE AIR5320 (TM). *Summary of Icing Simulation Test Facilities*. 1999.

[211] SAE AIR6189 (TM). *Design, Calibration, and Test Methods for Turbine Engine Icing Test Facilities*. 2017.

[212] Koivuluoto, H., Stenroos, C., Ruohomaa, R., Bolelli, G., Lusvarghi, L., and Vuoristo, P. “Research on Icing Behavior and Ice Adhesion Testing of Icephobic Surfaces.” *Proceedings of 16th International Workshop on Atmospheric Icing of Structures- IWAIS XVI, Jun 28–Jul 3*, 2015, pp. 1–14.

[213] Chen, J., Liu, J., He, M., Li, K., Cui, D., Zhang, Q., Zeng, X., Zhang, Y., Wang, J., and Song, Y. “Superhydrophobic Surfaces Cannot Reduce Ice Adhesion.” *Applied Physics Letters*, Vol. 101, No. 11, 2012, pp. 95–98. doi:10.1063/1.4752436.

[214] Zou, M., Beckford, S., Wei, R., Ellis, C., Hatton, G., and Miller, M. A. “Effects of Surface Roughness and Energy on Ice Adhesion Strength.” *Applied Surface Science*, Vol. 257, No. 8, 2011, pp. 3786–3792. doi:10.1016/j.apsusc.2010.11.149.

[215] He, Z., Vågenes, E. T., Delabahan, C., He, J., and Zhang, Z. “Room Temperature Characteristics of Polymer-Based Low Ice Adhesion Surfaces.” *Scientific Reports*, Vol. 7, No. August 2016, 2017, pp. 1–7. doi:10.1038/srep42181.

[216] Soltis, J., Palacios, J., Eden, T., and Wolfe, D. “Evaluation of Ice-Adhesion Strength on Erosion-Resistant Materials.” *AIAA Journal*, Vol. 53, No. 7, 2015, pp. 1825–1835. doi:10.2514/1.J053516.

[217] Xiao, S., Skallerud, B. H., Wang, F., Zhang, Z., and He, J. “Enabling Sequential Rupture for Lowering Atomistic Ice Adhesion.” *Nanoscale*, Vol. 11, No. 35, 2019, pp. 16262–16269. doi:10.1039/c9nr00104b.

[218] He, Z., Xiao, S., Gao, H., He, J., and Zhang, Z. “Multiscale Crack Initiator Promoted Super-Low Ice Adhesion Surfaces.” *Soft Matter*, Vol. 13, No. 37, 2017, pp. 6562–6568. doi:10.1039/c7sm01511a.

[219] Chaudhury, M. K., and Kim, K. H. “Shear-Induced Adhesive Failure of a Rigid Slab in Contact with a Thin Confined Film.” *European Physical Journal E*, Vol. 23, No. 2, 2007, pp. 175–183. doi:10.1140/epje/i2007-

10171-x.

[220] Liljeblad, J. F. D., Furó, I., and Tyrode, E. C. “The Premolten Layer of Ice next to a Hydrophilic Solid Surface: Correlating Adhesion with Molecular Properties.” *Physical Chemistry Chemical Physics*, Vol. 19, No. 1, 2017, pp. 305–317. doi:10.1039/C6CP05303C.

[221] Dong, W., Ding, J., and Zhou, Z. X. “Experimental Study on the Ice Freezing Adhesive Characteristics of Metal Surfaces.” *Journal of Aircraft*, Vol. 51, No. 3, 2014, pp. 719–726. doi:10.2514/1.C032393.

[222] Ozeki, T., Yamamoto, R., Izumiyama, K., and Sakamoto, T. “Ice Adhesion Tests on Pliable Polymer Sheets for Protection Against Sea-Water Spray Icing.” *Journal of Adhesion Science and Technology*, Vol. 26, No. 4–5, 2012, pp. 651–663. doi:10.1163/016942411X574817.

[223] Emelyanenko, K. A., Emelyanenko, A. M., and Boinovich, L. B. “Water and Ice Adhesion to Solid Surfaces: Common and Specific, the Impact of Temperature and Surface Wettability.” *Coatings*, Vol. 10, No. 7, 2020, p. 648. doi:10.3390/coatings10070648.

Appendix A

Aluminum Ice Accretion-Video 1.mp4

Video 1. GoPro recording (sped up to X8) of the impact ice accretion on the aluminum surface in the icing wind tunnel test section.

Aluminum Ice tensile Test-Video 2.mp4

Video 2. GoPro recording (sped up to X8) of the tensile test or pop-off test on the aluminum surface. It can be seen the violent release of the ice block from the aluminum surface.

SLIC Ice Accretion-Video 3.mp4

Video 3. GoPro recording (sped up to X4) of the impact ice accretion on the SLIC surface in the icing wind tunnel test section.

SLIC Ice Tensile Test-Video 4.mp4

Video 4. GoPro recording (sped up to X2) of the tensile test or pop-off test on the SLIC surface. Ice fracture occurs at 00.13 sec followed by the ice spinning and levitating above the SLIC surface for a duration of 5 sec. The ice block finally leaves the surface at 00.18 sec.

Linear Abrasion Test.MP4

Video 5. Video showing the linear abrasion test on the SLIC using the medium-coarse abradant.

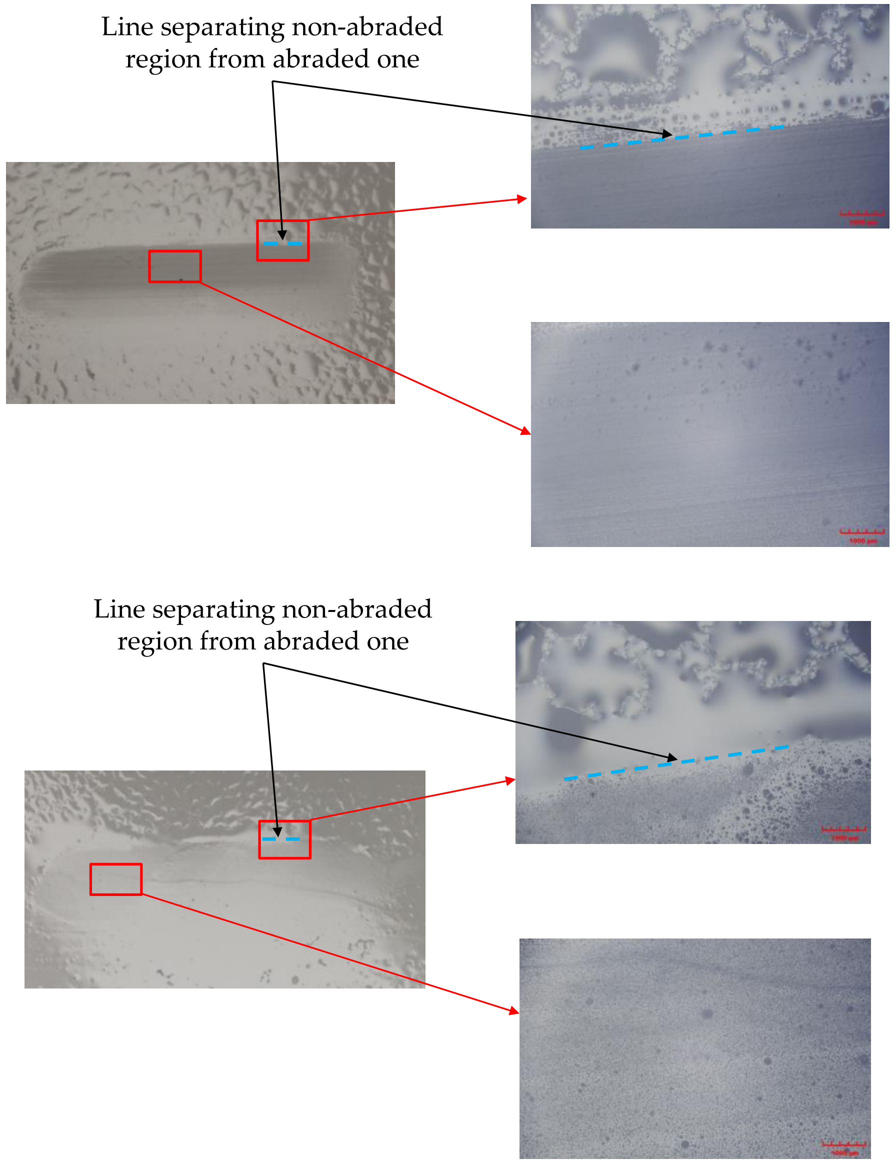

Figure 1. CANON photographic camera and HIROX microscope images of the SLIC coating post-abrasion. (a) & (b) are respectively photographs of the SLIC abraded by the medium-coarse abradant and the crocking cloth. (c) & (e) are respectively HIROX microscope images of SLIC showing both regions non-abraded and abraded by the medium-coarse abradant and the crocking cloth, while (d) & (f) are respectively HIROX microscope images of SLIC abraded region by the medium-coarse abradant and the crocking cloth.

Appendix B

Aluminum ice accretion.mp4

Video 1. Impact ice accretion on aluminum substrate disc (speed up X8).

Aluminum ice shear test.mp4

Video 2. Ice shear adhesion test on aluminum substrate disc (speed up X2) for impact ice condition. Ice fracture can be seen, followed by removal of the fractured ice residue.

Titanium ice shear test for static ice.mp4

Video 3. Ice shear adhesion test on titanium substrate disc (speed up X2) for static ice condition. Ice fracture can be seen, followed by removal of the fractured ice residue.

SLIC ice accretion.mp4

Video 4. Impact ice accretion on SLIC coated substrate disc (speed up X8).

SLIC Ice adhesion test.mp4

Video 5. Ice shear adhesion test on SLIC coated substrate disc (speed up X2) for impact ice condition. Ice fracture can be seen, followed by removal of the fractured ice residue.